Mondragon Unibertsitatea

DOCTORAL THESIS

IMPACT PERFORMANCE PREDICTION OF AS-MANUFACTURED RESIN TRANSFER MOULDING COMPOSITES USING MACHINE LEARNING BASED DIGITAL TWIN

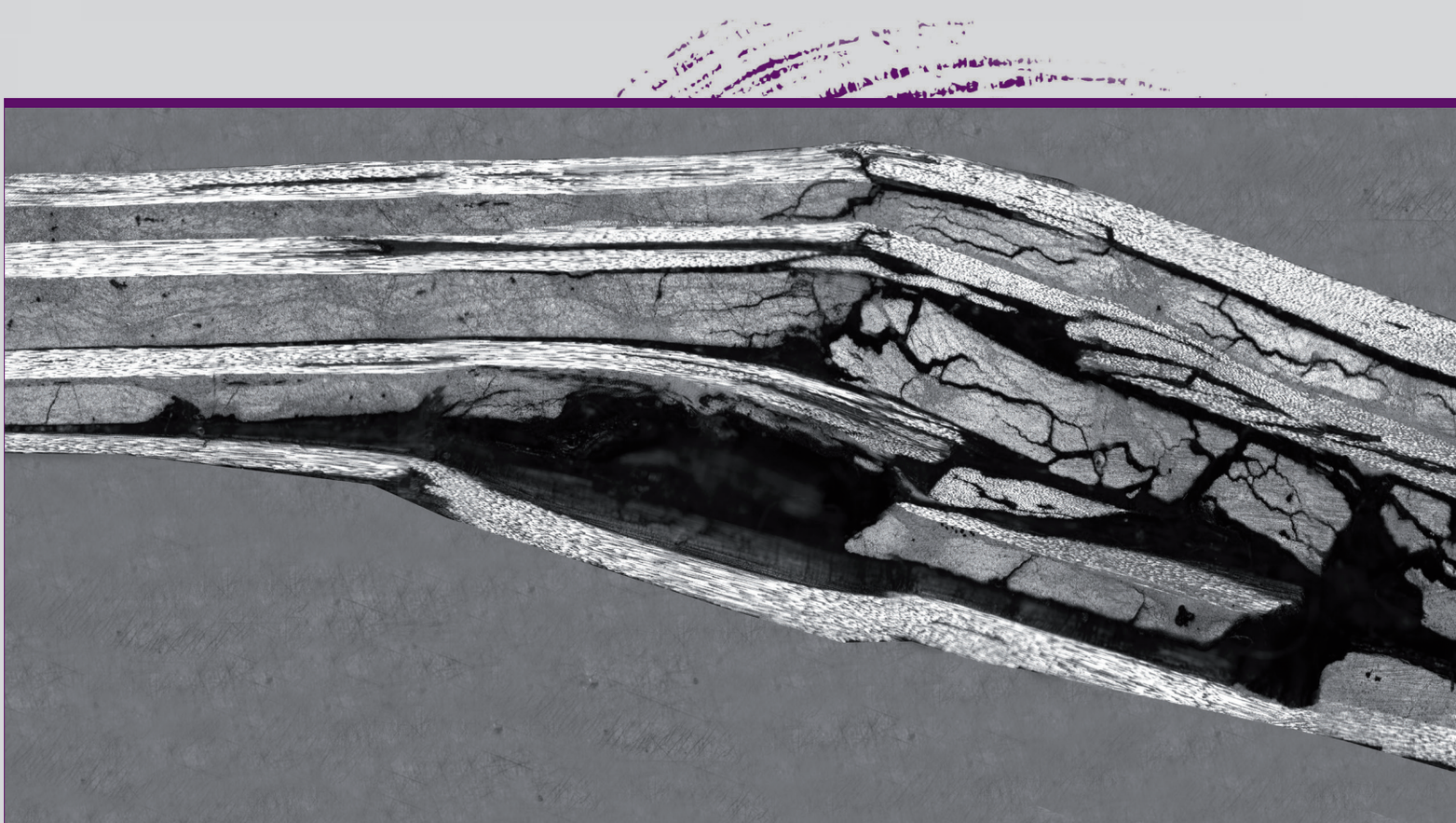

JULEN MENDIKUTE SAN MARTIN | Arrasate-Mondragón, 2022

JULEN MENDIKUTE SAN MARTIN | Impact performance prediction of as-manufactured Resin Transfer Moulding composites using Machine Learning based Digital Twin

Mondragon Unibertsitatea
Goi Eskola Politeknikoa
Faculty of Engineering

Impact performance prediction of as-manufactured Resin Transfer Moulding composites using Machine Learning based Digital Twin

Julen Mendikute San Martin
Department of Mechanics and Industrial Production
Mondragon Unibertsitatea

Supervisors:
Dr. Jon Aurrekoetxea Narvarte
Dra. Maider Baskaran Razkin

A thesis submitted for the degree of
Doctor by Mondragon Unibertsitatea

May 2022

Declaration of Originality

I hereby declare that the research recorded in this thesis and the thesis itself were developed entirely by myself, in the Polymer and Composites Technology research group, at Mondragon Unibertsitatea.

Julen Mendikute

Arrasate, May 2022

Acknowledgements

Tesiaren amaieran, nire esker ona adierazi nahi diet euren laguntzaren bitartez helburu hau betetzen lagundu didaten pertsona guztiei.
Lehenik eta behin, nire zuzendari izan diren Jon Aurrekoetxea eta Maider Baskarani eskerrak eman nahi nizkieke nigan jarritako konfiantza guztiagatik. Zuen laguntza eta dedikazioa ezinbestekoa izan da erronka hontan, eta gainera, beti izan duzue umorerako tartea.
Mondragon Unibertsitateko Konpositeen ikerketa lerroko lankide guztiei. Laborategiko momentu on eta txar guztietan bertan egon zaretelako, baita kongresuetan bizitako esperientzia politetan ere. Bestalde, Iñigo Llavoriri, Elementu finitutako modelizazioan eskeinitako laguntzagatik eta Ekhi Zugastiri, Adimen artifizialari buruz horrenbeste erakusteagatik.
Quisiera agradecer a Jaime Castro y a Carlos González por la oportunidad y el apoyo recibido durante mi estancia en IMDEA.
Era berean, lankide izan diren doktorando guztiei ere eskerrak ematea gustatuko litzaidake. Urte hauetan pasatako momentu guztiengatik, unibertsitatean eta unibertsitatetik kanpo. Nola ez, nire Debako lagunei, lanetik deskonektatzen laguntzeagatik eta urte guzti hauetan bertan egoteagatik.
Nire eskerrik berezienak eman nahiko nizkioke nire familiari; Aita, Ama eta Amaiari. Gaur naizena izateko ezinbestekoak izan zaretelako. Eta azkenik, eskerrik asko Gabi. Nire bizitzako bidelagun izateagatik eta egunerokotasunean nire alboan egoteagatik. Tesi hau zuena ere bada!

Abstract

The use of lightweight materials has demonstrated to be very energy efficient in the transport sector, reducing the consumption of fossil fuels and increasing the range of electric cars. Carbon fibre reinforced polymers (CFRP) have proven to be effective for structural lightweighting as they combine low density with good mechanical properties, especially in terms of specific strength and stiffness. Resin Transfer Moulding (RTM) is an effective process in the manufacture of high performance, geometrically complex structural parts with low process costs. However, the robustness of the RTM process remains a challenge, as both material and process uncertainties negatively affect the impregnation quality, generating void defects and dry zones. To address these defects, a paradigm shift has to take place, as the production system itself has to become an "expert" in material science and process technology. The manufacturing system must consider the defects generated in impregnation stage to recognise the risks in the final structural performance. In other words, a Digital Twin (DT) of the physical process must be constructed and accurately recreate the RTM process. For this purpose, the continuous Process-Structure-Property-Performance (PSPP) modelling approach has proven to be the key to the generation of DTs. Therefore, the objective of this thesis is to generate the scientific-technological knowledge for Digital Twins of the RTM process following the PSPP approach.

Firstly, an experimental characterisation of the material based on the PSPP approach has been carried out to quantify the effect of process parameters on void generation (Process-Structure), and subsequently, void effect on impact properties (Structure-Property). For this purpose, NCF-Epoxy biaxial laminates (0/90) with different void contents (0.58%, 1.35%, 2.44% and 4.34%) have been tested by the drop-weight impact test method. Samples with high void content (4.34%) recorded a 25.9% reduction in peak force, and a 9.57% reduction in dissipated energy compared to samples with low void content (0.58%). In addition, the penetration and perforation limits were lower in the high void content specimens, 20% and 30% respectively.

Secondly, a Machine Learning (ML) based impregnation quality diagnosis model has been developed. This model has been fed with information from process, synthetic data generated by FEM simulations, and has been able to predict the generated impregnation structure (Process-Structure). The diagnosis has been performed by means of a Supervised Learning binary classification model trained with synthetic dataset. Among the different predictive models studied, Extreme Gradient Boosting and Light Gradient Boosting

Machine were the most accurate models for predicting RTM filling quality, with an accuracy of 84.9% and 83.4%, respectively. In addition, a scaling of the ML model has allowed not only to predict the part quality, but also to locate the zones where the defect was generated. Comparing the computational time of the ML model with the FEM model, a reduction in computational time from 360 s to 1 s was observed. Thus, supervised learning predictive models can be used to diagnose the quality of the manufactured part using RTM. They are fast enough to be integrated into the process and feed the digital twin of the process.

Finally, a surrogate model based on ML-FEM has been developed, which, knowing the location and position of the impregnation defect, is able to predict the reduction of mechanical properties (Structure-Properties), and then the impact performance of the parts (Properties-Performance). The surrogate model has allowed predictions for (i) quality classification based on the maximum displacement, (ii) numerical prediction (regression) of the maximum displacement, and (iii) multi-output regression to obtain the impact curves ($F(t)$, $\delta(t)$, and $E(t)$). The results obtained have shown an accuracy of 95.85% in the classification and a R^2 of 0.86 in the regression. Once the surrogated model is trained, it is able to make predictions in less than 5 seconds, unlike the FEM model that needs about 60 minutes. In addition, the multi-output regression has been shown to be able to replicate accurately force, displacement and energy curves.

Combining both the impregnation quality diagnostic model (Process-Structure) and the structural performance predictive model (Structure-Properties-Performance), it has been possible to generate a DT based on the PSPP approach. Both models are fast enough to be integrated into the RTM process and allow online structural validation considering the process defects.

Resumen

El uso de materiales ligeros ha resultado ser energéticamente muy eficiente en el sector del transporte, ya que permite reducir el consumo de combustibles fósiles e incrementar la autonomía de los coches eléctricos. Los polímeros reforzados con fibra de carbono (CFRP) han demostrado ser eficaces para el aligeramiento estructural, ya que combinan una baja densidad con buenas propiedades mecánicas, sobre todo en términos de resistencia y rigidez específica. Resin Transfer Moulding (RTM) es un proceso efectivo en la fabricación de piezas estructurales de altas prestaciones, geométricamente complejas y con costes de proceso bajos. No obstante, la robustez del proceso RTM sigue siendo un reto, ya que las incertidumbres tanto del material como del proceso afectan negativamente en la impregnación, generando defectos de porosidad y zonas secas. Para hacer frente a estos defectos se debe dar un cambio de paradigma, ya que el propio sistema de producción tiene que convertirse en "experto" en ciencia de los materiales y en tecnología de proceso. El sistema de fabricación debe considerar los defectos generados en la impregnación para reconocer los riesgos en el rendimiento mecánico final. En otras palabras, se debe de construir un Gemelo Digital (DT) del proceso físico para recrear con precisión el proceso de RTM. Para ello, el enfoque de modelización continua de Proceso-Estructura-Propiedades-Rendimiento (PSPP) resulta ser clave. El objetivo de esta tesis, es la generación de conocimiento para sentar las bases científico-tecnológicas de los gemelos digitales del proceso RTM siguiendo el enfoque PSPP.

En primer lugar, se ha realizado un estudio experimental basado en el enfoque PSPP donde se ha estudiado el efecto de los parámetros de proceso en la generación de porosidad (Proceso-Estructura), y posteriormente, su efecto en las propiedades a impacto (Estructura-Propiedades). Para ello, se han ensayado laminados biaxiales (0/90) de NCF-Epoxy con diferentes contenidos de porosidad (0,58%, 1,35%, 2,44% y 4,34%) por el método de impacto por caída de dardo. Las muestras de alto contenido en porosidad (4,34%) han registrado una reducción del 25,9% en la fuerza máxima, y del 9,57% en la energía disipada en comparación con las muestras de bajo contenido en porosidad (0.58%). Además, los límites de penetración y perforación han sido inferior en las piezas de alto contenido de porosidad, 20% y 30% respectivamente.

En segundo lugar, se ha desarrollado un modelo de diagnóstico de calidad de impregnación basado en Machine Learning (ML). Este modelo, se ha alimentado con la información del proceso, datos sinteticos generados mediante simulaciones FEM, y ha

sido capaz de predecir la estructura generada (Proceso-Estructura). El diagnóstico se ha realizado mediante un modelo de clasificación binaria de Aprendizaje Supervisado entrenado con un conjunto de datos sintéticos. Entre los diferentes modelos predictivos estudiados, Extreme Gradient Boosting y Light Gradient Boosting Machine han sido los modelos más precisos para predecir la calidad de llenado del RTM, con una precisión del 84,9% y 83,4%, respectivamente. Además, un escalado del modelo ML ha permitido no sólo predecir la calidad de la pieza, sino también localizar las zonas donde se generó el defecto. Comparando el tiempo de cálculo del modelo ML frente al modelo FEM y se ha observado una reducción de 360 s a 1 s en el tiempo computacional. Así pues, los modelos predictivos de aprendizaje supervisado pueden utilizarse para diagnosticar la calidad de la pieza fabricada mediante RTM. Son lo suficientemente rápidos como para integrarse en el proceso y alimentar el gemelo digital del proceso.

Por último, se ha desarrollado un modelo subrogado basado en ML-FEM, que conociendo la localización y la posición del defecto de impregnación es capaz de predecir la reducción de propiedades mecánicas (Estructura-Propiedades), y después el comportamiento a impacto de las piezas (Propiedades-Rendimiento). El modelo subrogado ha permitido realizar predicciones para (i) la clasificación de calidad basada en el desplazamiento máximo, (ii) la predicción numérica (regresión) del desplazamiento máximo, y (iii) la regresión multi-salida para obtener las curvas de impacto($F(t)$, $\delta(t)$, y $E(t)$). Los resultados obtenidos han mostrado una precisión del 95,85% en la clasificación y un R^2 de 0,86 en la regresión. Una vez entrenado el modelo subrogado, es capaz de realizar predicciones en menos de 5 segundos, a diferencia del modelo FEM que necesita unos 60 minutos. Además, la regresión multi-salida ha demostrado ser capaz de replicar las curvas completas de fuerza, desplazamiento y energía.

Combinando ambos, el modelo de diagnóstico de la calidad de la impregnación (Proceso-Estructura) y el modelo predictivo del comportamiento a impacto (Estructura-Propiedades-Rendimiento), es posible generar un DT. Ambos modelos son lo suficientemente rápidos como para integrarse en el proceso de RTM y permiten la validación mecánica en línea considerando los defectos del proceso.

Laburpena

Material arinen erabilera energetikoki oso eraginkorra dela frogatu da garraioaren sektorean, erregai fosilen kontsumoa murrizteko eta auto elektrikoen autonomia luzatzeko aukera ematen baitu. Karbono-zuntzez indartutako polimeroak (CFRP) eraginkorrak dira egitura arintzeko, dentsitate baxua eta propietate mekaniko onak konbinatzen baitituzte, batez ere erresistentzia eta zurruntasun espezifikoa. Resin Transfer Moulding (RTM) prozesua eraginkorra da prestazio handiko, geometrikoki konplexuak eta kostu baxuko piezak fabrikatzeko. Hala ere, RTM prozesuaren fidagarritasunak erronka bat izaten jarraitzen du, materialaren eta prozesuaren ziurgabetasunek negatiboki eragiten baitute inpregnazio kalitatean, batez ere porositate akatsak eta eremu lehorrak sortzen. Akats horiei aurre egiteko, paradigma aldaketa bat behar da, fabrikazio-sistema bera "aditu" bilakatu behar baita, materialen zientzian eta prozesu teknologian. Fabrikazio-sistemak kontuan hartu behar ditu inpregnazioan sortutako akatsak, azken egituraren errendimendu mekanikoa aurreikusteko. Hau da, prozesu fisikoaren Biki Digitala (DT) eraiki behar da, eta RTM prozesua zehaztasunez digitalki sortu. Horretarako, prozesuaren modelizazio jarraia, Prozesua-Egitura-Propietateak-Portaera (PSPP) metodologian oinarritua, funtsezkoa da. Tesi honen helburua, RTM prozesuaren biki digitalen inguruan ezagutza sortzen da, PSPP ikuspegian oinarrituz.

Lehenik eta behin, PSPP ikuspegian oinarritutako azterketa esperimental bat egin da. Azterketa horretan, prozesu parametroek porositatea sortzeko duten eragina kuantifikatu da (Prozesua-Egitura), eta, ondoren, porositateak talka-propietateetan duen eragina (Egitura-Propietateak). Horretarako, NCF-Epoxy biaxialen (0/90) saiakuntzak egin dira porositate-eduki desberdinekin (% 0,58; % 1,35; % 2,44 eta % 4,34), dardo bidezko talka metodoaren bidez. Porositate handiko laginek (% 4,34) % 25,9 murriztu dute indar maximoa, eta % 9,57, berriz, disipazio energia, porosidade baxuko laginen aldean (% 0,58). Gainera, penetrazio eta zulatze mugak txikiagoak izan dira porositate handiko laginetan, % 20 eta % 30, hurrenez hurren.

Bigarrenik, Machine Learning-en (ML) oinarritutako inpregnazio-kalitatearen diagnostiko modelo bat garatu da. Modelo hau prozesuko datuekin elikatu da, FEM simulazioen bidez sortutako datu sintetikoak, eta prozesu ostean sortutako egitura aurreikusten du (Prozesua-Egitura). Gainbegiratutako Ikaskuntza (Supervised Learning) modelo baten bidez egin da diagnostikoa, datu sintetiko multzo batekin entrenatuta. Aztertutako modelo prediktiboen artean, Extreme Gradient Boosting eta Light Gradient Boosting Machine

izan dira RTMaren betetze-kalitatea aurresateko modelorik zehatzenak, % 84,9 eta % 83,4 eko zehaztasunarekin. Gainera, ML modeloaren eskalatze bati esker, piezaren kalitatea aurreikusteaz gain, akatsa sortu den eremuak aurkitu ahal izan dira. ML modeloaren kalkulu-denbora FEM modeloarekin alderatuz gero, denbora konputazionalean 360 s-tik 1 s-ra murriztu dela ikusi da. Beraz, gainbegiratutako ikaskuntzaren modelo prediktiboak RTM bidez fabrikatutako piezaren kalitatea diagnostikatzeko erabil daitezke. Bestalde, prozesuan integratzeko eta prozesuaren biki digitala elikatzeko bezain azkarrak dira.

Azkenik, ML eta FEM-en oinarritutako modelu subrogatu bat garatu da. Modelo honek, inpregnazio defektuaren kokapena eta porosidade maila ezagututa, propietate mekanikoen murrizketa aurreikus dezake (Egitura-Propietateak), eta, ondoren, piezen talka portaera aurreikus dezake (Propietateak-Portaera). Modelo subrogatua hiru zatitan banatua izan da: (i) gehienezko desplazamenduan oinarritutako kalitate sailkapena, (ii) desplazamendu maximoaren balioaren aurreikuspena (erregresioa) eta (iii) talka-kurbak lortzeko multi-irteera erregresiboa ($F(t)$, $\delta(t)$, eta $E(t)$). Lortutako emaitzek erakutsi dutenez, % 95,85-eko zehaztasuna lortu da sailkapenean, eta % 0,86-koa erregresioko R^2 balioan. Bestalde, modelo subrogatua entrenatu ondoren, 5 segundo baino gutxiagoan egin ditzake iragarpenak; FEM modeloak, berriz, 60 minutu behar ditu. Gainera, multi-irteera erregresioak frogatu du gai dela indarraren, desplazamenduaren eta energiaren kurba osoak erreplikatzeko.

Biak konbinatuz, inpregnazioaren kalitatearen diagnostiko-modeloa (Prozesua-Egitura) eta egiturazko portaeraren modelo prediktiboa (Egitura-Propietateak-Portaera), PSPP ikuspegian oinarritutako DT bat sor daiteke. Bi modeloak RTM prozesuan integratzeko bezain azkarrak dira, eta prozesu-defektuak kontuan hartuta piezen portaera mekanikoa on-line balioztatzeko aukera ematen dute.

Contents

List of Figures

List of Abbreviations

AI . . . . . Artificial Intelligence

ANN . . . . . Artificial Neural Networks

AUC . . . . . Area Under the Curve

BIW . . . . . Body-In-White

CDM . . . . . Continuum Damage Mechanics

CFRP . . . . . Carbon Fibre Reinforced Polymers

CVFE . . . . . Control Volume/Finite Element

DT . . . . . Digital Twin

FEM . . . . . Finite Element Method

ILSS . . . . . Inter-Laminar Shear Strength

LCM . . . . . Liquid Composite Moulding

ML . . . . . Machine Learning

NCF . . . . . Non-Crimp Fabrics

NDI . . . . . Non-Destructive Inspection

PSPP . . . . . Process-Structure-Property-Performance

RF . . . . . Random Forest

RFE . . . . . Recursive Feature Elimination

ROC . . . . . Receiver Operating Characteristic

RTM . . . . . Resin Transfer Moulding

SEM . . . . . Scanning Electron Microscope

SL . . . . . Supervised Learning

UD . . . . . Uni-Directional

WCM . . . . . Wet Compression Moulding

XCT . . . . . X-ray micro-Computed Tomography

XGBoost . . . . . eXtreme Gradient Boosting

ZDM . . . . . Zero-Defect Manufacturing

List of variables

α . . . . . [-] Curing conversion

γ . . . . . [N/mm] Surface tension of the resin

$\delta^0_{I,\mathrm{eq}}$ . . . . . [m] Equivalent displacement of totally damaged

$\delta_{I,\mathrm{eq}}$ . . . . . [m] Equivalent displacement

$\delta^{\mathrm{f}}_{I,\mathrm{eq}}$ . . . . . [m] Equivalent displacement of the onset of damage

$\delta(t)$ . . . . . [m] Displacement on impact test

η . . . . . [-] B-K coefficient

θ . . . . . [°] Resin fibre contact angle

μ . . . . . [Pa s] Viscosity of the resin

ν_{12} . . . . . [-] Principal Poisson's ratio

ρ_{c}, ρ_{f}, ρ_{m} . . . . . [kg/m^3] Density of the composite sample, fibre and matrix

σ_{11}, σ_{22}, σ_{33} . . . . . [MPa] Tension in three dimensions

$\sigma_{I,\mathrm{eq}}$ . . . . . [MPa] Equivalent stress

ϕ . . . . . [-] Porosity of the textile

Ca^* . . . . . [-] Modified capillary number

Ca^*_{opt} . . . . . [-] Optimum modified capillary number

E_1, E_2, E_3, G_{12}, G_{23}, G_{13} . [GPa] Elastic constants of the unidirectional ply

E_0 . . . . . [J] Incident energy on impact test

E_{d} . . . . . [J] Delamination onset energy

E_{dis} . . . . . [J] Dissipated energy

E_{ff} . . . . . [J] Fibre failure onset energy

F_{d} . . . . . [N] Delamination force on impact test

F_{p} . . . . . [N] Peak force on impact test

$F^{\mathrm{t}}_{\mathrm{f}}$, $F^{\mathrm{c}}_{\mathrm{f}}$, $F^{\mathrm{t}}_{\mathrm{m}}$, $F^{\mathrm{c}}_{\mathrm{m}}$ . . . . . [-] fibre and matrix failure indices

$G^{\mathrm{C}}_{\mathrm{n}}$, $G^{\mathrm{C}}_{\mathrm{s}}$, $G^{\mathrm{C}}_{\mathrm{t}}$ . . . . . [J/m^2] Inter-laminar fracture toughness Mode I, II, III

$G^{\mathrm{ft}}_{\mathrm{f}}$, $G^{\mathrm{fc}}_{\mathrm{f}}$, $G^{\mathrm{mt}}_{\mathrm{f}}$, $G^{\mathrm{mc}}_{\mathrm{f}}$ . . . . . [kJ/m^2] Fracture energies per unit area

$\mathbf{K}$ . . . . . [m^2] Permeability tensor

k_{ref} . . . . . [m^2] Reference permeability without binder

k_{binder} . . . . . [m^2] Permeability without binder

k_{xx}, k_{yy} . . . . . [m^2] Permeability in x and y direction

K_{nn}, K_{ss}, K_{tt} . . . . . [N/m^3] Stiffness penalty in normal, 1st and 2nd shear

L_c . . . . . [m] Characteristic length for each failure mode

P . . . . . [Pa] Pressure

Q_{inj} . . . . . [m^3/s] Injection flow rate

T . . . . . [°C] Temperature

t_n, t_s, t_t . . . . . [MPa] Inter-laminar tension in normal, 1st and 2nd shear

t_n^0, t_s^0, t_t^0 . . . . . [MPa] Inter-laminar failure in normal, 1st and 2nd shear

v . . . . . [m/s] Impregnation velocity

v_{opt} . . . . . [m/s] Optimum impregnation velocity

v_f, v_r, v_v . . . . . [-] Fibre, resin and void volume fraction

w_c, w_f, w_m . . . . . [g] Weight of the composite, fibre and matrix

w_i . . . . . [g] Weight of the composite sample immersed in water

X^T, X^C, Y^T, Y^C, S^L, S^T . [MPa] Strength values of the unidirectional ply

1 Introduction

Contents

In this first chapter, the scientific-technological background of this doctoral thesis and the organization of the thesis report are presented. This thesis has been carried out within the Applied Engineering PhD program, in the "Plastics and Composites Technology" Research Group of the Department of "Mechanics and Industrial Production" of Mondragon Unibertsitatea. In addition, the work has been funded by a pre-doctoral grant from the Basque Government (PRE_2021_2_0272).

1.1 Scientific-technological background

The environment is always a matter of concern for Europe, specially, when dealing with the automotive industry. Proof of this is the resolution signed by the European Parliament in which a climate and environmental emergency was declared, and as a solution, the objective of reducing greenhouse gas emissions by 55% in 2030 was proposed[1].

Studies have shown that the transport sector accounts for a quarter of greenhouse gas emissions in Europe, with 72% of these emissions coming from road transport[2]. Weight reduction is the most cost-effective way to minimize transportation-related fuel consumption and greenhouse gas emissions, and it has become a major industrial problem. Studies showed that a 10% weight reduction can reduce the fuel consumption of internal combustion engine vehicles by 6-8% or increase the range of electric cars by 10% [Reiland

[1] European Parliament resolution of 28 November 2019 (2019/2930(RSP))
[2] Shares of European greenhouse gas emissions (Source: EEA)

2020]. Additionally, lightweighting increases safety, as a lighter vehicle takes less energy to brake, and reduces the amount of kinetic energy to be dissipated in a crash.

Carbon Fibre Reinforced Plastics (CFRP) have lightweighting potential as they combine low density with high mechanical properties in terms of specific strength, specific stiffness, toughness and good corrosion resistance [González 2017]. Automotive industry is looking for a higher use of CFRP, but the high operating costs associated with its manufacturing processes limit a wider application in the sector. Liquid Composite Moulding (LCM) processes, and specially Resin Transfer Moulding (RTM), are competitive for overcoming these challenges [Bel 2015]. RTM is a processing method with potential for producing low-cost and geometrically complex automotive composite parts [Sozer 2012].

Different main car manufacturers have introduced RTM parts for body-in-white (BIW) structural applications. BMW is one of the biggest drivers in this trend, and among its exponents are the i3 and i8 electric vehicles with their monocoque body called "life module" of NCF-CFRP made entirely by RTM. The BMW 7-series also includes critical BIW elements such as roof rail manufactured via High-Pressure Resin Transfer Molding and roof bows or tunnel manufactured with Wet Compression Moulding (WCM) [Mason 2022]. The recently launched BMW iX features a multi-material body with CFRP components manufactured using RTM. Particularly important are the A, B and C-pillars and the roof frame components (Figure 1.1). This made possible a reduction of 80 kg compared to the BMW X5, which is similar in size.

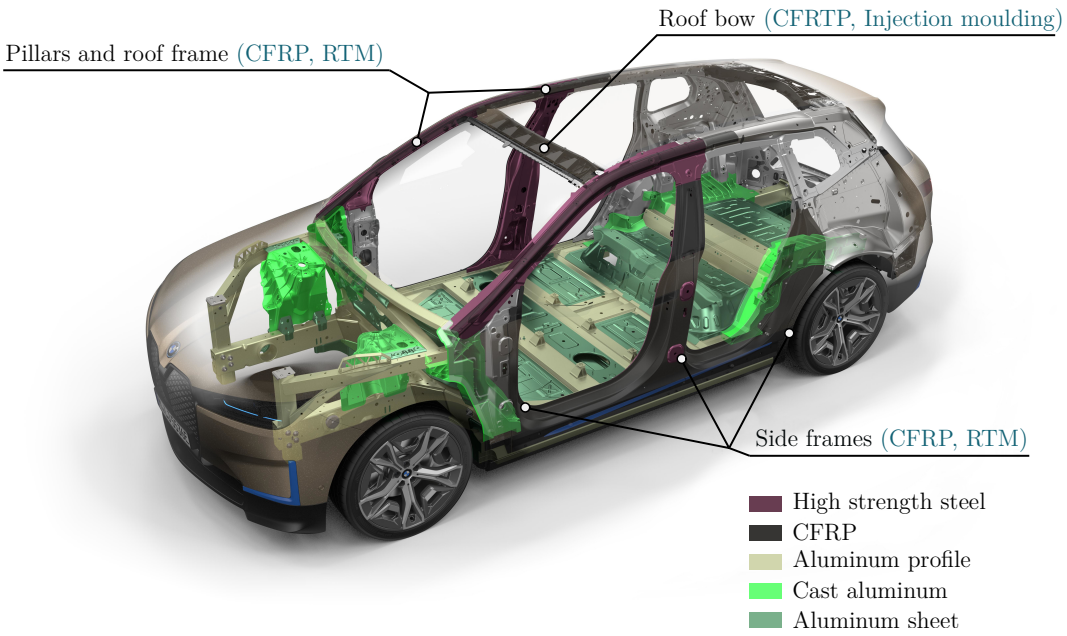

Figure 1.1: BMW iX chassis consists of CFRP parts (Adapted from [BMW group 2021]).

Nonetheless, RTM process robustness is still a challenge, as the part quality is affected by the intrinsic manufacturing uncertainties (fabric reinforcement, matrix material and process parameters variations) and it induces impregnation defects [Mesogitis 2014]. Consequently, to ensure the quality of the final part, complex and time-consuming Non-Destructive Inspection (NDI) operations are required. The cost of these NDI operations can reach 15% of the value of the final component [Crane 2018]. As impregnation related defects reduce the mechanical properties, severe acceptance criteria (less than a 1% of void content [Hamidi 2018]) are imposed, resulting in costly rework or scrappage. Additionally, more conservative part designs which do not enhance the lightweight potential of CFRP are applied [Zambal 2018].

In recent years, simulation models have made a qualitative leap forward, making it possible to simulate the different production phases of composites as well as the structural behaviour of the parts in a reliable manner. However, the digital revolution that is now taking over the industry aims to go one step further. Not only intends to be able to simulate everything in isolation, but to integrate all the phenomena in a digital model that replicates the physical part. This replication is known as the Digital Twin (DT) and is intended to be a cornerstone of the future of manufacturing, as it enables the active process control and the in-line quality assessment (Figure 1.2). The DT will be updated with material data, process parameters and physical sensors. It will be able to monitor the process for predictive maintenance of the machine, detection of defects and prediction of the performance of the as-manufactured part.

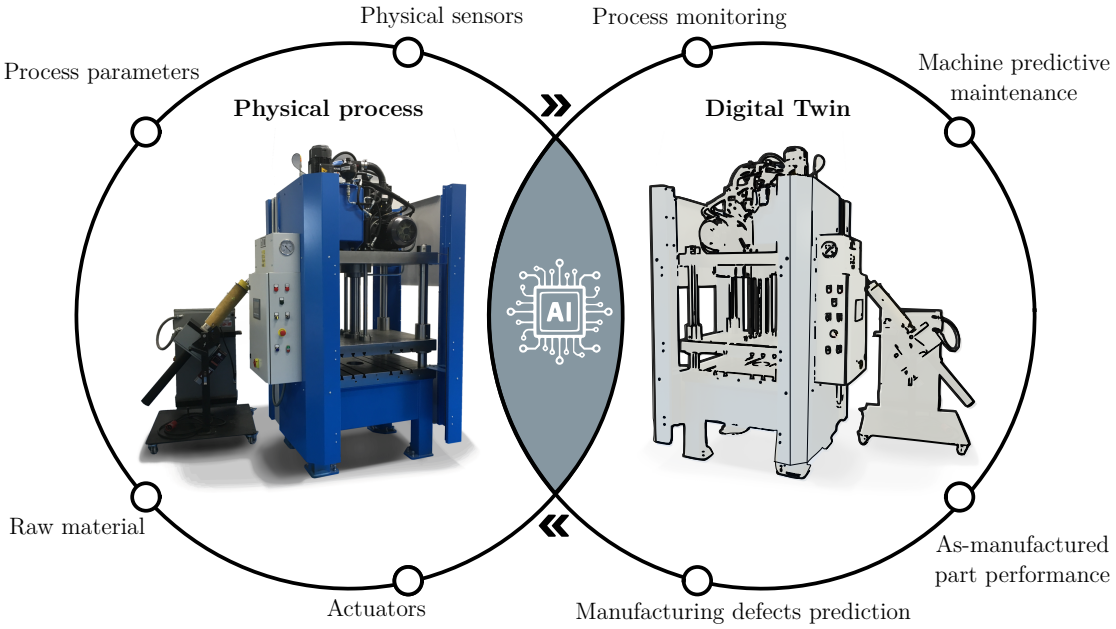

Figure 1.2: Interaction between the physical process and its Digital Twin.

In recent years, a considerable effort has been made towards Zero-Defect Manufacturing (ZDM), which is often too costly. The new DT-based approach, however, does not focus on manufacturing defect-free parts, but parts with a number of defects that do not compromise its structural integrity. For that, the manufacturing system must be enhanced with material science and process technology intelligence, and establish accurate Processing–Structure–Property–Performance (PSPP) relationships [Gomez 2021]. In this way, the digital twin will give a much more realistic view of the part and provide information on "as-manufactured" instead of "as-designed" [Heinecke 2018]. This paradigm shift replaces quality-based criteria with those based on product performance, leading to a reduction in part defectiveness and an improvement in the robustness of the composite processes. In the PSPP approach (Figure 1.3), the Processing-Structure link relates process parameters, such as internal pressure or temperature, directly to the structure of the material in terms of void content, fibre misalignment or degree of cure among others. The second link, the Structure-Property link, relates the structure of the material to each of its physical, chemical and mechanical properties (thermal conductivity, Young's modulus, impact properties...). Finally, the Property-Performance relationship determines the behaviour of a part, (either in terms of displacement, failure or energy absorption, for instance) under specific operating conditions and environmental effects [Agrawal 2016].

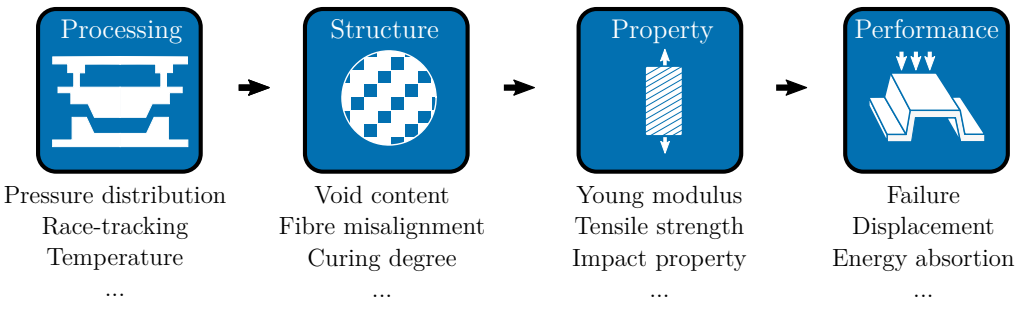

Figure 1.3: PSPP methodology.

Creating PSPP Digital Twins based on the Virtual Process Chain, which is a concatenation of FEM models, is computationally costly and is not suitable for integrating as an in-line quality assessment within the DT [Henning 2019]. Data-driven surrogate models, also called meta-model or emulator, can solve this challenge by replacing the expensive physics-based FEM simulations with reduced degrees-of-freedom models [Bárkányi 2021]. Among surrogate modelling techniques, successful Machine Learning (ML) based methods are gaining popularity in composite materials [C. T. Chen 2019].

Therefore, in this thesis, the RTM process will be integrated into a holistic DT powered by Artificial Intelligence (AI). In this way, it will be possible to model the process-to-performance chain in a fast and reliable way.

1.2 Organization of the thesis report

The thesis document consists of seven sections including the introduction section described in this **Chapter 1**.

In **Chapter 2** a review of the state of the art of composite manufacturing by RTM is presented. The aim is to understand in depth the generation of voids and their effect on the mechanical properties. In addition, different ways of generating DT based on AI are analysed, considering similar cases found in the industry. To conclude the chapter, a critical review of the state of the art is presented.

On **Chapter 3** the global objective of the thesis is presented, which is to generate scientific-technological knowledge for the generation of a digital twin of the RTM process based on the PSPP approach. In addition, for the fulfilment of this global objective, numerical-experimental operational objectives are defined.

In **Chapter 4** the first contribution of the thesis is described. It demonstrates how different RTM process parameters generate different levels of voids, and thus, the impact properties of the material are reduced. In other words, the experimental Processing-Structure-Property link is generated.

The development and validation of a predictive model based on supervised learning for the diagnosis of defective RTM is presented in **Chapter 5**. It is demonstrated that by monitoring the injection phase of RTM it is possible to detect the impregnation defects generated during the process which is key for future in-line quality assessment. In this way, the Processing-Structure link of the digital twin proposed in this thesis is created.

The third and last contribution of this thesis is described in **Chapter 6**, where a surrogate ML-based model for the prediction of the in-service performance of composite parts that consider void defects is developed and validated. In this way, the Structure-Property-Performance link necessary for the development of the Digital Twin is generated.

Finally, **Chapter 7** summarises the general conclusions and contributions of the present thesis. Furthermore, recommendations for future lines of research are described.

2
State of the art

Contents

The final quality of CFRP parts manufactured using RTM is highly dependent on manufacturing conditions. Therefore, in order to generate a Digital Twin of the process it is necessary to understand the process, detect implicit deviations from the process, quantify the origin and effect of defects, and finally, control the process. The review of the current state of the art was carried out following the Process-Structure-Property-Performance methodology and focusing on individual linkages.

2.1 Resin Transfer Moulding Process-Structure

This section focuses on the analysis of RTM technology for the manufacture of CFRP parts. Focusing on (i) the resin impregnation phase in the reinforcement fabrics, (ii) the

study of the uncertainties of the process affecting the variability of permeability and (iii) the defects generated in the impregnation phase due to the uncertainties. In other words, the **Process-Structure** link of the RTM process is analysed.

Resin Transfer Moulding (RTM) is part of a generic family known as Liquid Composite Moulding (LCM). In this process, the dry textile is placed in the cavity of the mould and liquid resin is injected under positive pressure, impregnating dry textiles. RTM is a well-established process for niche applications and has several advantages for the manufacture of high performance compounds [Advani 2010], such as low investment in equipment, excellent control of mechanical properties, closed mould processing, low injection pressures, integration of inserts and freedom of design. The main steps followed in RTM manufacturing are layup and draping, mould closure, resin injection, curing and demoulding [Sozer 2012]. Firstly, the lay-up preform is placed in the mould cavity automatically or manually and the textile is draped to the mould geometry (Figure 2.1-1). Once the preform is placed, the mould is closed. This step can be done manually with clamps or bolts or with the help of compression press (Figure 2.1-2). When the mould is closed and the preform is compacted to the desired thickness, the resin is injected (Figure 2.1-3). It is considered the most critical stage that can determine the final quality of the part. In this stage, the liquid resin is injected in the mould cavity at controlled flow-rate or controlled pressure. The injection strategy will be defined by; part size and geometry, cycle time and the resin gel time among other aspects. The resin injection will finish when resin reach the vents ports, understanding that the mould cavity has been filled. Then, vent and injection ports are closed and the resin is cured (Figure 2.1-4), and demoulded (Figure 2.1-5).

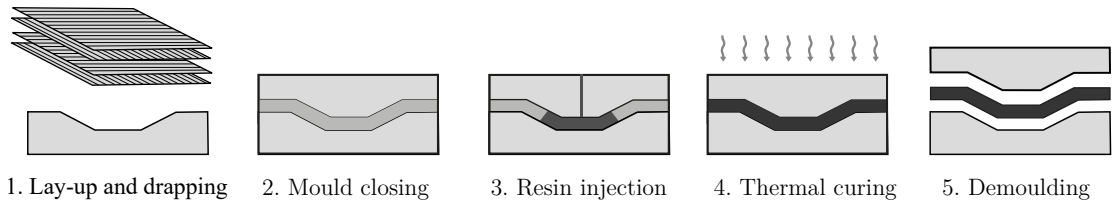

Figure 2.1: RTM prcess steps.

In CFRP composites, fibre makes up 40-60% of the total volume, and these fibres are responsible for supporting the structural loads as they provide stiffness and strength to the part. Among the different types of fibres, carbon fibre is the most widely used primary in structural applications, ahead of other synthetic fibres (glass, aramid, etc.) or natural fibres. The individual fibres are arranged in tows where each one can contain thousands of individual fibres. In turn, the rovings are arranged in different textile architectures. Among the most commonly used architectures, Non-Crimp Fabrics (NCF) have the largest

share of all structural lightweighting application in automotive industry [Lomov 2011]. NCF are an advanced textile fabrics that integrates more than one unidirectional fibres ply in order to avoid tow crimp in the fibre direction [Bel 2015]. This architecture improves the strength, stiffness and fatigue life of composite parts. The architecture of an NCF is described as a multi-scale geometry with three main levels (Figure 2.2): the preform scale (macro: $10^{-1} - 10^{0}$ m), yarn or bundles and stitches scale (meso: $10^{-2} - 10^{3}$ m) and fibre filaments scale (micro: 10^{-5} m) [Loendersloot 2011].

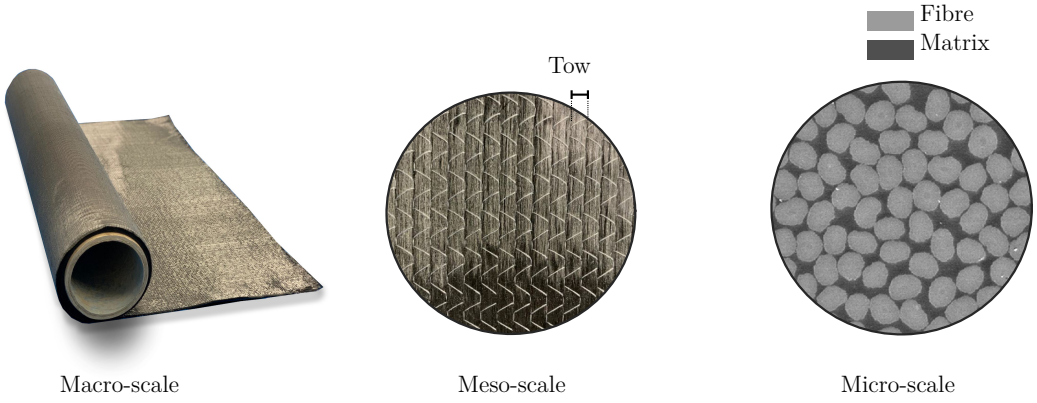

Figure 2.2: Textile scales: macro meso and micro.

The second main component of composites, the resin, is responsible for bonding all the fibres together and provide a permanent geometry. In this way, under mechanical stress, the composite is able to work in synergy. In a thermoset polymeric matrix, the resin system consists mainly of a thermoset resin and a hardener. Once the resin and hardener are mixed, the curing phase begins. The viscosity of the resin will increase exponentially as the degree of cure of the resin increases. A parameter to take into account in manufacturing is the gel time. This parameter determines the time in which the viscosity is too high for the impregnation of the textile, and thus, the processing time should be lower than the gel time. Among the resins on the market, the most suitable for automotive mass production are those with a very low viscosity. These resins allow to reduce the manufacturing cycle times as well as to reduce the equipment required.

2.1.1 Resin flow in textile reinforcements

The advancement of the flow through a one-scale porous medium is well described by Darcy's law, which indicates that the flow-rate is proportional to the pressure gradient inside the mould [Advani 2010]:

$$\vec{V} = -\frac{\mathbf{K}}{\mu}\nabla P \tag{2.1}$$

assuming that the mould is non-deformable and the resin is a Newtonian incompressible fluid, so the the continuity (mass conservation) equation, $\nabla \cdot \vec{V} = 0$, resulted in:

$$\nabla \cdot \left(\frac{\mathbf{K}}{\mu} \nabla P \right) = 0 \tag{2.2}$$

where, $\vec{V}$ [m/s] is the averaged Darcy's velocity, μ the fluid viscosity [Pa s], and P is the local fluid pressure [Pa]. $\mathbf{K}$ is the macroscopic permeability tensor of the preform [m^2] and is as follows:

$$\mathbf{K} = \begin{pmatrix} K_{xx} & K_{xy} & K_{xz} \\ K_{yx} & K_{yy} & K_{yz} \\ K_{zx} & K_{zy} & K_{zz} \end{pmatrix} \tag{2.3}$$

if the selected coordinate direction is along the main directions of the preform can be simplified to three variables; K_{xx}, K_{yy}, and K_{zz}. In literature, a distinction is often made between the in in-plane permeabilities, K_{xx} and K_{yy}, and out-of-plane permeability K_{zz}:

$$\mathbf{K} = \begin{pmatrix} K_{xx} & 0 & 0 \\ 0 & K_{yy} & 0 \\ 0 & 0 & K_{zz} \end{pmatrix} \tag{2.4}$$

the Darcy velocity is related to the surface velocity of the resin through the porosity (ϕ) of the textile, which is is related to the volume of fibre (V_f) in the cavity. The velocity is then calculated in the following way:

$$\vec{V} = \vec{V}_r \phi \tag{2.5}$$

the main injection strategies are at constant pressure or at constant flow-rate. At constant pressure injection, The inlet pressure is constant during the injection. Therefore, the inlet flow-rate is a consequence and it decreases with the flow-front advancement. At constant flow-rate, the inlet pressure increases as the flow-front advances. In most cases, the injectors have an upper pressure limits, so when the inlet pressure reaches this value automatically switches to constant pressure injection.

The flow pattern is affected by the mould and injection shape; rectilinear, radial or rectilinear-radial combination. In rectilinear flow (Figure 2.2a), the resin is injected from an inlet port located in a border of the mould, creating a one-dimensional flow. The advancement of the flow front is parallel to the mould wall, considering totally 1D flow. The vent port is usually located at the end of the mould. In the case of radial flow in radial mould, the resin inlet is located in the middle point of the mould and the created fluid flow is two-dimensional [Rudd 1997] (Figure 2.2b). In the rectilinear-radial combination, the flow is radial until the flow reaches the walls of the rectangular mould, and After this instant, it gradually becomes almost a rectilinear flow [Rudd 1997] (Figure 2.2c).

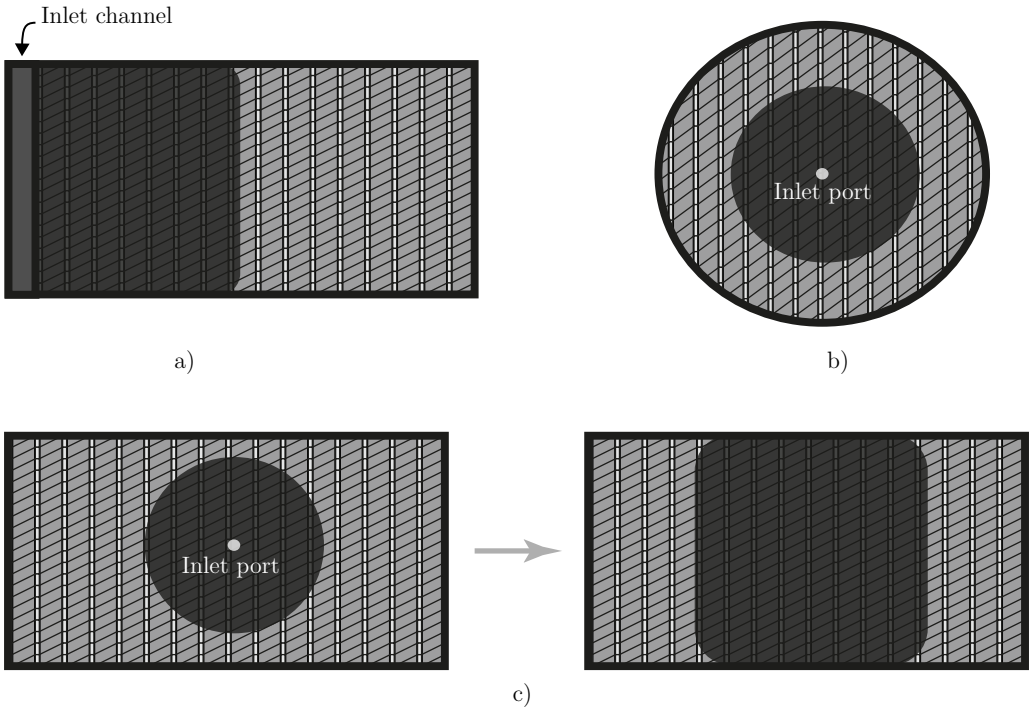

Figure 2.3: Type of impregnation: a) rectilinear, b) radial and c) rectilinear-radial.

Dual-scale flow

Analytically the reinforcement preform is considered a homogeneous single-scale porous medium and the Darcy's law is applied to describe the macroscopic flow evolution. Most textile reinforcements, however, are composed of tows that are woven in a specific pattern [Park 2011]. This architecture is described as dual-scale porosity, where the channels between the fibres in the tow are known as micro-porosity and the channels between the tows are known macro-porosity. Carbon fibre has a diameter of about 10 µm and the micro-porosity is of the same scale. The macro-porosity is of the order of the mm. Therefore, the macro-porosity is three orders of magnitude greater than micro-porosity [Sozer 2012] and the flow of resin through the textile fibre is described as a dual-scale flow [Gokce 2005].

The hypothesis of an accentuated flow front that divides the liquid and air phases is not valid. As the flow front advances, the tows keep saturating. The resin flow-rate entering in the tow is added as a sink (s) in the mass conservation equation [Bodaghi 2019b]:

$$\nabla \cdot \left(\frac{\mathbf{K}}{\mu} \nabla P \right) = s \tag{2.6}$$

In dual-scale fabrics, there is a partially saturated zone covering a significant distance behind the flow front, separating the fully saturated-zone and the unfilled zone (Figure 2.4a). The length of the partially saturated area remains constant in time. It has been seen that in the partially saturated zone, by reducing the flow passage the permeability

is decreased [Park 2011]. Therefore, unsaturated permeability is lower than saturated permeability [Bréard 2003; Kuentzer 2007]. This confirms the need to define permeability as a function of the degree of saturation (s): the ratio between the saturated volume and the total volume. The main phenomena due to saturation delay are pressure dropping and non-linear pressure profile [Park 2011] (Figure 2.4a). As seen at the beginning of this section, Darcy's law describes the inlet pressure increases linearly over time for single-scale fabrics. However, it has been seen that in dual-scale textiles it does not grow linearly but drops over time (pressure dropping phenomena) (Figure 2.4b). This is explained by the delay in saturation of the fabric, and as long as the pressure profile is non-linear. Analytical [Kuentzer 2007; Zhou 2006] and numerical [Parnas 1991] solution for pressure dropping phenomena are reported in literature.

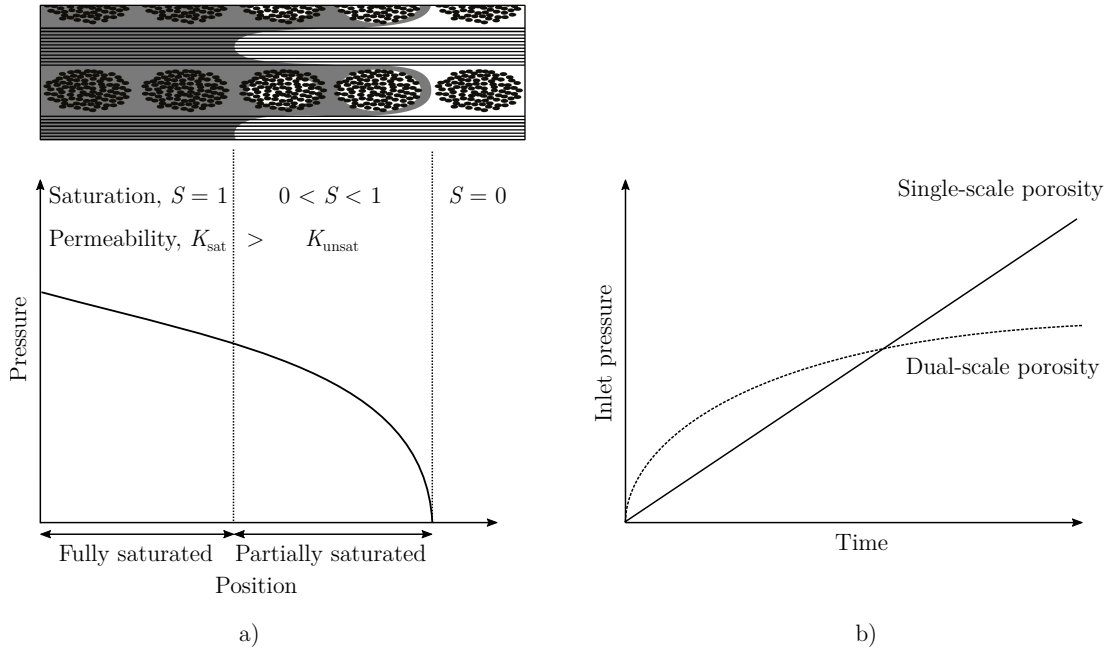

Figure 2.4: Dual-scale flow: a) pressure drop along position, and b) inlet pressure [Park 2011].

2.1.2 Uncertainties related to the process

The intrinsic uncertainty associated with the RTM process lead to the generation of scrap with consequences on the cost of manufacture and the environment. On the other hand, defects generated in the process directly compromise the mechanical behaviour of composite parts. The potential of the composites is not exploited, since designs that are more conservative are used. Moreover, this arises the rejection rate, which requires costly reworking and scrapping actions [Potter 2009]. The uncertainties of the process are classified in three groups [Konstantopoulos 2019; Mesogitis 2014]: (i) variations and defects in the textile architecture generated during the production, handling or storage of textiles,

(ii) variations in resin system during the storage conditions, in its composition or in its formulation, and (iii) Uncertainty in process conditions and environmental parameters.

Variations and defects in the textile architecture

Textile variability influences mainly the filling stage of the process, leading to unfilled and unsaturated regions. This is caused by stochastic distribution of the permeability along the preform that alter the filling pattern of the resin. The variation of the filling pattern can be associated with two types of uncertainties: textile imperfections and textile architecture variation.

The inherent textile imperfection may occur in production, handling or storage of textiles and pre-exist in the material provided by carbon fibre manufacturers. Eight different textile imperfection have been categorized [Schneider 2011] (Figure 2.5): wrinkle generation by sharp fold, Cut or tear in preform, yarn splice, fuzz ball or accumulation of frayed fibres on the surface, gap between fibre yarn, missing of stitching or knitting loop, deviation of fibre orientation, and Missing of reinforcement yarn.

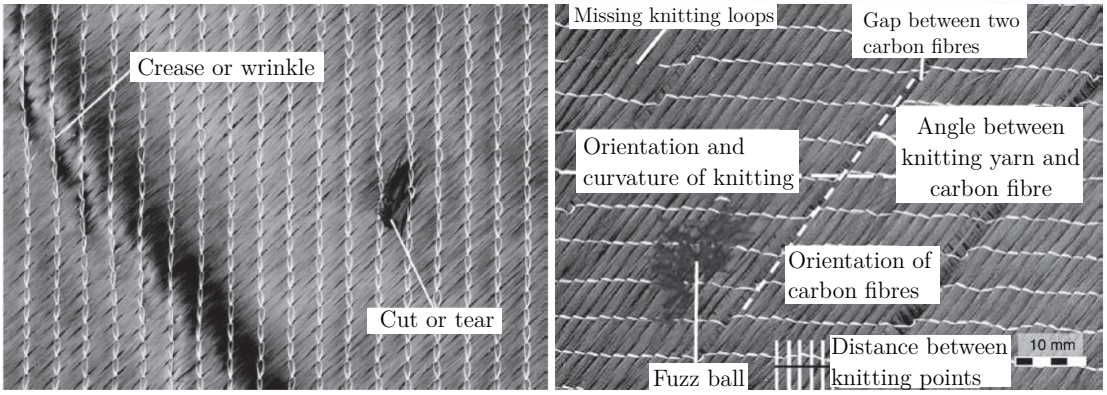

Figure 2.5: Defects in the textile architecture [Schneider 2011].

Besides, there is a variability in permeability due to the fabric inherent variations such as the stitching, shearing, nesting effect and binder application.

In NCF textiles, stitching is used to bind reinforcing layers together [Schnabel 2011]. This is not considered textile imperfection but it can affect the filling stage generating preferential flow channels. The permeability can be affected for two reasons, the stitching seams itself and the opening generated due to the stitching. In the case of radial injection, the ellipse orientation and the shape is influenced by stitching seams. Rieber *et al.* [Rieber 2009] conclude that for a seam distance of 7.5 mm the global permeability is reduced by 33%. This is explained by the understanding that the seams are obstacles to flow that makes it difficult for the flow to penetrate [Chiu 2002]. The results of the numerical simulations also suggest that the effect of the stitches is very different for a different type

of stitch size, off-centre position, slope, matrix, distribution density [hu 2003]. Similarly, the stitching opening can modify the permeability of the preform. Recent work [Lomov 2011] shows that 25% of the stitches creates a 0.6 mm wide opening between tows. By the same way, the transverse permeability is increased linearly witch the stitch density due to the generated openings [Drapier 2002].

When NCF is sheared during the preforming stage, the fibre orientation, areal density and fabric density and hence fibre volume fraction are modified [Lomov 2011]. The local geometry variation of biaxial NCF has been studied [Loendersloot 2011] and different mechanical properties models have been developed [Truong 2008]. Furthermore, shearing has been widely studied regarding to its influence on the local permeability. The influence was quantified by Demaria *et al.* [Demaría 2007] with the development of a predictive model that estimates the value of the permeability tensor and its directions as a function of the deformation angle. In the case of NCF it is shown that two relevant factors must be considered: the ratio of principal permeability components (K_{xx}/K_{yy}) and their direction of principal axes with respect to the shear deformation of the fibre.

In the preforming phase, the textile preform is compacted to the specified thickness and the architecture of the preform is modified. The phenomenon of how different layers of fabric interconnect with each other is called nesting, considering the perfect nesting when all peak and valleys fit exactly. Nesting reduces the thickness and thus the permeability is reduces as v_{f} is increased [Bodaghi 2019b]. The degree of nesting varies spatially, so it introduces a large scatter in permeability measurements [Hoes 2004], being the main contributor to permeability scatter [Konstantopoulos 2019]. The effect of nesting in permeability has been studied in several numerical and experimental studies [Belov 2004; Senoguz 2001] reaching the conclusion that the permeability values can differ by an order of magnitude. In addition, it has been demonstrated that the effect of nesting on out-of-plane permeability is up to two orders of magnitude greater with no-nesting than with maximum nesting [Fang 2015].

Permeability is also influenced by binder application; it is increased as binder application influences preform distribution and porosity [Dickert 2012]. One of the possible reasons is that the adhesion of the binder hinders the accommodation of the fibres, thus preventing nesting. Consequently, the channels of the original fabric are not reduced and the permeability higher [Baskaran 2017].

Variations in matrix system

The uncertainties regarding the matrix system affects not only to the filling stage but also to the curing stage. The filling is affected as the chemical composition of the matrix system affect to the viscosity of the fluid. Besides, the curing kinetic is also modified and hence the curing stage [Konstantopoulos 2019]. The batch-to-batch resin variation affect to the process. On the other hand, defects induced by mixing can alter the process.

For that, automatic mixing can be more accurate than manual mixing as human errors are reduced. It has been seen that a deviation of 1% in curing agent can reduce the enthalpy of the reaction by 23 J/g [Núñez 1995]. Finally, the aging effect affect the chemical properties of the resin, as there is a gradual deterioration of their properties [Konstantopoulos 2019]. The aging effect can occur on shelf life or storage life of the resin. A study about the aging effect on Epoxy resins shows that its properties are degraded below the unacceptable threshold in 6 month in optimum environment [Sands 2001].

Uncertainty in process conditions and environmental parameters

The quality of the final part can be directly affected by variations in process parameters. Among the process parameters, two main source of deviation can be identified. First, the deviation in the part-tool interface and second, the temperature variation in the process. A preferential flow channel can be generated between the preform and the tool. This effect known as race-tracking is arisen as an imperfections in preform placing. The resin flows faster for the preferential channel. Race-tracking strength [Devillard 2003] is defined as the ratio between permeability along the gap (free edge) and bulk permeability in race-tracking direction. This race-tracking strength has been quantified to range from 4-27 for warp direction and 2-34 for weft direction [Lawrence 2004]. This high variation in permeability causes unfilled region in the preform, known as dry zones, once the resin reach the vent port. The mould tooling withstand the injection pressure and the compaction pressure. This inner pressure deflect the mould making the cavity thickness non-uniform. This deflection has been quantified and it has been observed that a radial injection of 130 kPa in a 6 mm thick polycarbonate mould increases the nominal thickness from 4 mm to 5.03 mm [MacLaren 2009]. This thickness variation leads to filling time variation being necessary an extra post-filling time for the mould to recover the nominal thickness [Konstantopoulos 2019]. The process temperature is a key parameter in composite manufacturing as it affects not only the injection stage but also the curing stage. When the composite part is injected and cured at ambient temperature the temperature variable is not controlled being a clear source of uncertainties [Konstantopoulos 2019]. In the case of controlled temperature, the injection system and the mould are heated. The accuracy of the temperature control system is another source of uncertainty.

2.1.3 Manufacturing defects

The RTM process can induce defects in the composite material being an inconvenience to a wider use of technology [Carlone 2015; Park 2011]. For this reason, it is important to understand the formation mechanism, characterization techniques and the reduction/removal techniques of these defects [Hamidi 2018]. These knowledge allow to reduce the defects generated during the RTM process and to reach the quality standards of the autoclave processes [Chowdhury 2008]. The defects that arise in the manufacturing process

are classified in two main groups: design-induced defects and process-induced defects [Potter 2009]. The design-induced defects are in relation to material selection, tooling design, process parameters definition and they can be prevented. Process-induced defects are those that are inherent in the process itself and cannot be completely eradicated. This process-induced defects are generated during impregnation stage and there are classified in two types: dry zones and voids (micro-voids and macro-voids).

Dry zones formation

Once the mould has been filled there can appear areas that have not been impregnated. Dry zone is a non-impregnated area (Figure 2.6), also called an unsaturated area, where the flow of resin did not reach [Hamidi 2018]. Complete wetting of the preform is a problem of great concern in the industry and components containing dry zones are rejected [D. H. Lee 2006]. Therefore, it is essential to know how they are generated and how to prevent them from being generated. The dry zone can be caused by air entrapment due to the fusion of multiple flow fronts. This fusion of flow fronts occurs in both single-point and multi-point injections causing the formation of dry zones in components manufactured by RTM. Higher local permeability zones in the preform can enhance this phenomenon [D. H. Lee 2006; J. Yang 2010]. Besides, the high variation in permeability caused by race-tracking can be another cause of the generation of dry zones in the preform once the resin reaches the vent port [Bodaghi 2016; Lawrence 2004].

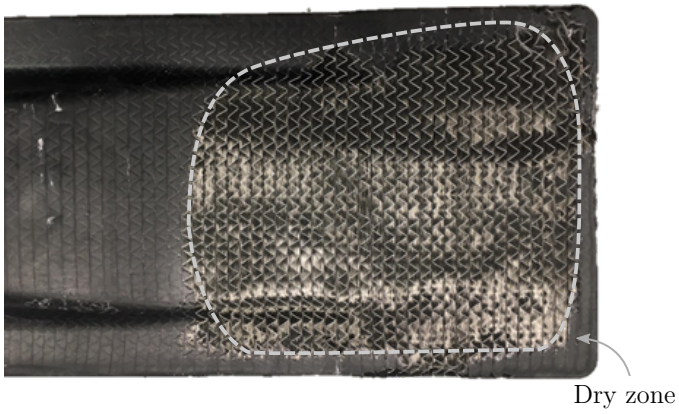

Figure 2.6: Generation of a dry zone in a part manufactured by RTM.

Voids formation mechanism and characterization methods

The voids are generated by different mechanism: mechanical air entrapment, nucleation, leakage, cavitation or uneven resin curing. However it has been found that the voids generated by air entrapment are the most common in the RTM manufacturing process [Leclerc 2008; Matsuzaki 2014; Park 2011]. The voids generated by air entrapment are

classified in two types based on their location: Micro-voids and macro-voids. In dual-scale architectures, the resin flows through the channels between the fibres in the tow and through the channels between the tows [Park 2011]. It is demonstrated that the velocity of the flow has a significant influence on the volume and type of void generated [Bréard 2003; Labat 2001; Patel 1995b; Patel 1995a; Patel 1996b], and it is justified by the balance between the two types of forces involved, the viscous force and the capillary. When the impregnation velocity is high, the flow follows the preferential path formed by the spaces between tows, and the interior of the tow is not totally impregnated, generating micro-voids (Figure 2.7a). On the contrary, when the velocity of the flow front is low, capillarity allows faster progress through the tow than between them, which generates a macro-void (Figure 2.7b).

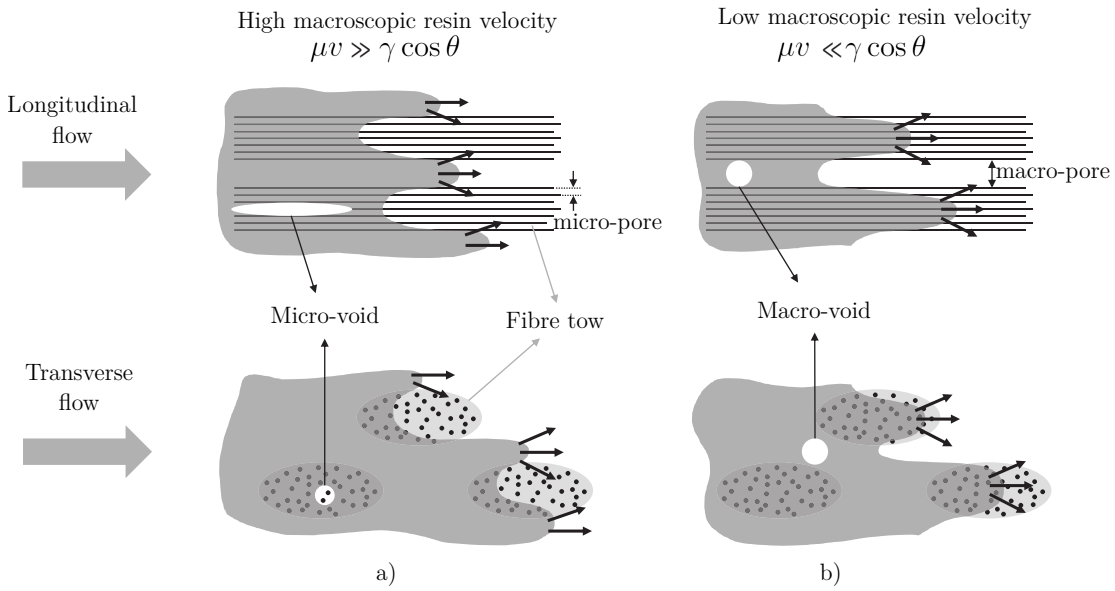

Figure 2.7: void generation mechanisms for a) macro-voids and b) micro-voids [Mehdikhani 2019].

The capillarity number Ca^* is a dimensionless constant representing the ratio between viscous and capillary forces [Patel 1995b; Patel 1995a; Patel 1996b; Rohatgi 1996]:

$$Ca^* = \frac{\mu v}{\gamma \cos\theta} \tag{2.7}$$

which depends on the resin/fibre contact angle (θ), the surface tension of the resin (γ), the viscosity of the resin (μ) and the velocity of the flow front (v).

Different experimental works have been carried out where the volume of voids of different liquid is correlated with the number of capillarity [Rohatgi 1996; Patel 1996a; Leclerc 2008]. Demonstrating that the relationship between the void content of both micro-void and macro-void, and Ca^* can be fitted into a master curve (Figure 2.8). When the capillary number is low, micro-voids tend to be created. On the contrary,

when it is higher, macro-voids are generated. This implies that there is an optimal range of capillary number that generates the lower void content, which is always greater than zero [Gourichon 2008; Leclerc 2008].

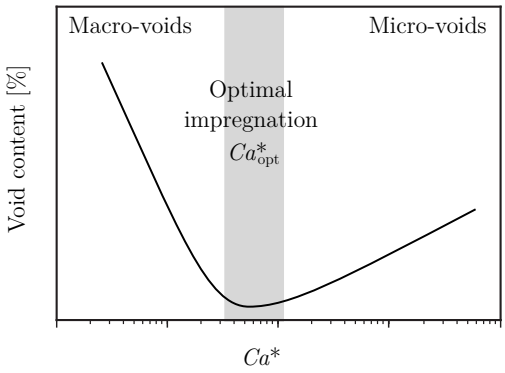

Figure 2.8: Characteristic void content as a function of Ca^* curve.

Several void characterization technique have been developed in order to quantify the void content in composites specimens. There are on-line characterization techniques that monitor the void generation during the filling. However, the post-cured characterization techniques are wider used in industry as their simplicity. The most used techniques for the post-curing characterization of CFRP parts are constituent content measurement by matrix removal, ultrasonic C-scan inspection, radiographic technique and microscopic image analysis [Hamidi 2018]. The density measurement, ASTM 792-08, is useful to characterize the fibre, resin and void volume fraction. ASTM D3171-15 technique describes the needed step to be followed for volume fraction measurement. This standard consists of physically eliminating the matrix by digestion or burn-off, leaving the reinforcement unaffected. In this way, it is possible to quantify the content (in volume or weight) of the fiber, the matrix and voids. However, the uncertainty in fibre density induces measurement error and it is possible to obtain results of negative voids content, which is physically impossible [Bowles 1992]. In terms of results, it allows just the overall void content and it does not give information about the shape, distribution and the size of the voids. The ultrasonic C-scan technique is a qualitative non-destructive technique for general defects detection in composite parts [Kuentzer 2007]. The mechanism is based on the transmission of shorts pulses of ultrasonic energy. The X-ray micro-computed tomography (XCT) technique is another non-destructive technique, which enables the detection of voids up to 1 µm in size [S. M. Sisodia 2016]. The microscopic image analysis is used for void quantification and analysis of shape, size and distribution. This method involves cutting and preparing a small sample for analysis under an optical microscope or Scanning Electron Microscope (SEM). For void content assessment, the image is post-processed using optical counting technique [Mehdikhani 2019]. It has been

demonstrated that the microscopic image analysis is one of the most accurate technique for void content measurement in CFRP parts [Santulli 2002].

Void reduction strategies

Based on the capillary analysis defined in the previous section [Patel 1995a], several research publications focus on the reduction of voids content by working on the optimal capillary number. Ruiz *et al.* [Ruiz 2006] propose a methodology based on the analysis of the capillary number for the reduction of micro-voids and macro-voids formed during the injection phase. In order to do this, the capillarity number at each point of the flow front was calculated and the injection flow was corrected in order to bring the capillarity number closer to its optimum value. As can be seen, when injected with constant pressure (Figure 2.9a) and constant flow-rate (Figure 2.9b), the void content was high. On the other hand, when variable flow injections were programmed to keep Ca^* constant at its optimum value (Ca^*_{opt}) (Figure 2.9c) the void content decreased.

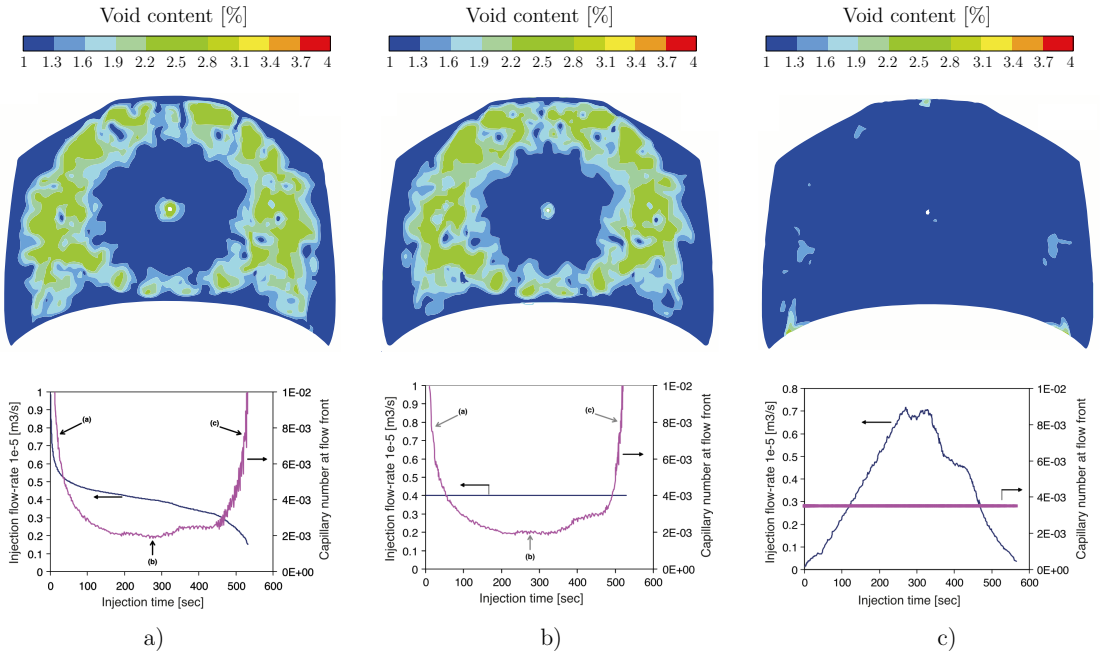

Figure 2.9: Injection flow rate and capillary number for a) constant inlet pressure b) constant flow-rate and c) optimized injection [Ruiz 2006].

2.1.4 Flow monitoring

Online process monitoring system are used for monitor the process data, compare with the ideal process data and if necessary take action on the process parameters. Although the process parameters (temperature, viscosity, permeability, injection strategy...) are optimized by numerical process simulations, does not always ensure an optimized manufacturing process. This deficiency is due to the sensitivity of the resin flow to

process disturbances (change in local permeability) and material variables (compressibility and local permeability), which can lead to defects and reduced properties in the final part. This high variability in the quality of the product can be reduced by online measurement of process and material properties and that is why monitoring techniques are key enabler for process optimisation [Griffin 2017].

Digital cameras are the simplest way to monitor the flow front advanced in RTM [Nielsen 2002]. Nevertheless, they are limited to transparent mould, which are not suitable for CFRP manufacturing.

Optical fibres are embedded in the RTM mould for mould filling and resin cure monitoring. The travelling light is influenced under strain or thermal change affecting to the reflective surface [S. Konstantopoulos 2014].

The sensors that detect electromagnetic properties include dielectric analysis sensors and direct current sensors. In the Dielectric sensors, the sample is located between parallel electrodes (dielectric sensors) which create an electrical field. Monitoring the dielectric permittivity the degree of conversion, viscosity and flow front position can be predicted [S. Konstantopoulos 2014]. Unique linear sensor [Skordos 2000], parallel large sensors [Hegg 2005] and a sensor grid [Yenilmez 2009] are used. In direct current sensors, the conductivity of a medium between two discrete point is measured. The sample act as an electrically conductivite medium [S. Konstantopoulos 2014]. This type of sensors are capable of predictiong the flow front position as flowing resin closes the circuit once it arrives to sensor location [Bickerton 2001; Lawrence 2004]. It is possible to monitor the curing of the resin as the resistance of the medium is changed during the curing of the resin [Garschke 2012].

The ultrasonic transducers are widely used in composite manufacturing, especially in curing stage [Aggelis 2012]. It is able to monitor the evolution of the mechanical properties during the curing of the part. For that, an ultrasonic wave is propagated trough the sample and longitudinal and shear velocities of waves propagation are measured [S. Konstantopoulos 2014].

The main thermal monitoring systems are thermocouples and infrared thermometers. Whereas thermocouples measures the voltage proportional to the contact temperature, the infrared thermometers uses a photo sensible cell that is able to detect the thermal radiation emitted by a sample [S. Konstantopoulos 2014]. The thermocouples are used in RTM processes since it enables the filling and curing monitoring [Tuncol 2007], however, the temperature at discrete point is only measured. On the other hand, the infrared thermography cameras allow the monitoring of thermal image of the superficial face [Cuevas 2013].

Pressure transducers work with piezo-resistive effect as they change the electrical resistance with pressure application and are particularly advantageous [Di Fratta 2013]. They are able to withstand the temperature and pressure conditions of the injection phase (Up to 200 ^{o}C and 20 bars). They may be incorporated in the mould and reuse

several times without compromising the part's quality [S. Konstantopoulos 2014]. Such sensors, moreover, often produce local pressure measurements, and covering a considerable area would be expensive. In literature a work associating pressure values measured at discrete sensor positions with flow front progression along defined flow paths is found [Di Fratta 2016]. In this way, they monitor the flow front by combining experimental data, acquired by a limited number of sensors, and pressure profile calculations. The pressure values detected by each sensor were associated with flow progression along predefined current lines. At each impregnation time step, an algorithm optimized the position of the flow front along such lines, minimizing the differences between calculated and measured pressures at the sensor locations. Additionally, the generated void content can be directly linked to the data acquired by pressure sensor [Gourichon 2008].

2.1.5 Impregnation phase modeling

Computational tools have been a very powerful ally of engineering, since they allow very accurate approximations of any type of problem described with partial differential equations. In particular, Finite Element Method (FEM) based models have been used to optimise numerous manufacturing processes by replacing trial-and-error approaches [W. K. Liu 2021].

A variety of FEM-based mathematical models have been developed for the optimisation of the draping, impregnation and curing stage of the RTM process [Sozer 2012]. This study is focused exclusively on the impregnation phase, as it is considered the most critical stage of the process. The impregnation phase is modelled according to Darcy's law and volume of fluid or Control Volume/Finite Element (CVFE) methods are used to solve it [Pierce 2017]. The CVFE method is the most frequently used method and is also the method employed by commercial softwares, either PAM-RTM®, LIMS® or MoldFlow®. The method consists of a 5-step iterative process (Figure 2.10). In the first step, the domain space is discretised into elements, nodes and volume controls. In the second step, it calculates the pressure gradient within the mould for the given boundary conditions. In the third step, the velocity field for each of the control volumes is calculated from the pressure gradient. In the fourth step, from the flow velocity, the minimum time required to fill a single control volume is determined and the adjacent volumes are considered to be partially filled. Finally, in the fifth step, the new flow front is determined and the new boundary conditions are established. From this new flow front, the process is repeated iteratively from step 2 until the mould is completely filled.

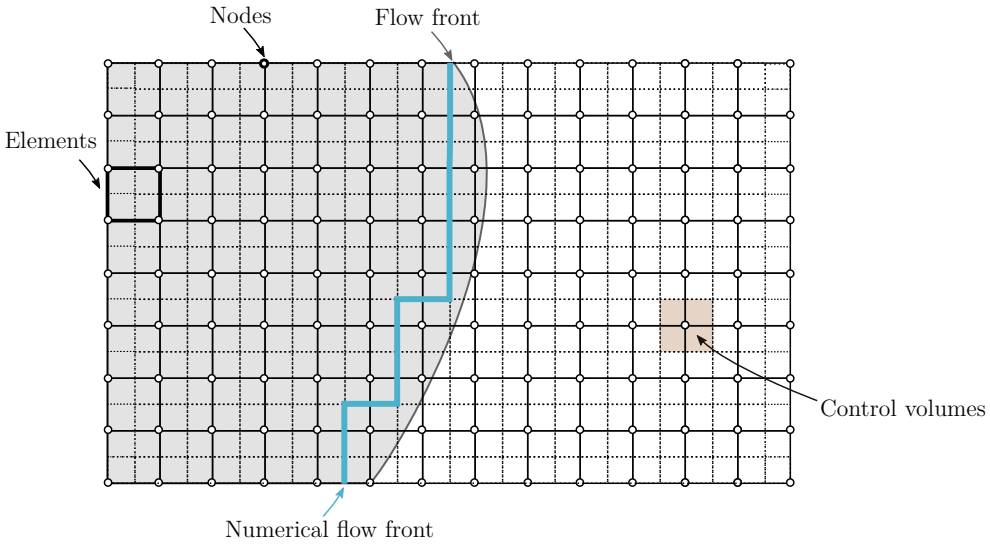

Figure 2.10: Control Volume/Finite Element (CVFE) method for flow simulation (based on [Pierce 2017]).

This method allows the calculation of filling times, internal pressures, filling patterns and thus reduces the probability of generating dry zones. Therefore, simulations are essential in process design, as they allow optimisation of injection point locations, vacuum points, and other process considerations [Pierce 2017]. The robustness of the impregnation is highly dependent on the accuracy of the permeability values of the textile reinforcement. However, the stochasticity and variability of reinforced textiles compromise the robustness of numerical models. Since the local variability of the textile geometry affects the local permeability of the reinforcement and hence the filling pattern [Bodaghi 2019b]. Despite the need to characterise permeability accurately, there is no standard method for this measurement and several characterisation methods exist [Loendersloot 2011]. Typically, the fluid used in measurements is a constant viscosity fluid, because it simplifies mould preparation and cleaning and reduces the cost of the experiment [Fauster 2019]. The methods used for permeability characterisation are classified according to: (i) the filling pattern whether it is rectilinear or radial, (ii) saturation level whether it is saturated or unsaturated and, (iii) the injection strategy whether is at constant pressure or constant flow rate. In the same way, determining the viscosity of the resin is crucial. For this purpose, there are different methods such as the Ford viscosity cup [McKelvie 1978], Falling ball Method [Stabik 2009], Capillary flow method [McKelvie 1978], and rotational viscosimeter. This last method, the rotational viscosimeter, is the most widely used in the literature to determine the viscosity of phenolic, polyester or epoxy resins [Stabik 2009; Kim 1993].

Different works have demonstrated the possibility of numerically predicting the level of voids by using the capillary number. By measuring the surface tension of the resin, the contact angle between the resin and the fibre, the viscosity of the resin and by calculating

the impregnation velocity, it is possible to determine the level of voids generated in each control volume. In this way, it has been shown that it is possible to reduce the level of voids in a part only by controlling the impregnation velocity [Trochu 2006; Ruiz 2006].

2.2 Structure-Property

The study about the effect of voids on different mechanical properties is shown in this section. Emphasis is placed on work where the reinforcement fabric architecture was RTM and the manufacturing process was one of the LCM variants. In this section the **Structure-Property** link, the second link in the PSPP chain, is studied.

Defects induced by the RTM process, and in particular voids, make it difficult to achieve the quality standards of the robust autoclave process [Mesogitis 2014]. Therefore, quantifying the effect of voids on mechanical performance is essential to achieve the robustness required by the industry [Hamidi 2018]. While analytical, statistical or numerical studies have been conducted, experimental work has made the major contribution to this study [Mehdikhani 2019].

For the quantification of the effect of voids on mechanical properties, it is essential to be able to introduce voids in a controlled manner. In the in the investigation carried out by Klosterman *et al.* [Klosterman 2021], they, compare different techniques for generating void content in a controlled way, such as water spray method, inappropriate pressure and inappropriate temperature application. For RTM processes, the purpose has been fulfilled by non-optimal impregnation velocities [Leclerc 2008].

Many articles can be found in the literature that analyse the effect of void content on different mechanical properties. The consensus in the literature is that matrix-dominated properties are clearly affected by the void content, whereas in the fibre-dominated properties the effect is not so evident. The majority of these studies are related to prepreg textiles, where voids are generated by modifying the consolidation pressure. There are few works available about the effect of voids on the reduction of mechanical properties of NCF manufactured with RTM.

2.2.1 Void effect in mechanical properties

On the basis of the different studies found in the literature, the negative effect of voids on the following mechanical properties are described: (i) Tensile modulus and tensile strength in longitudinal and transversal directions, (ii) Intra-laminar shear modulus, (iii) compression modulus and strength, (iv) flexural modulus and strength, (v) Inter-Laminar Shear Strength (ILSS), (vi) inter-laminar fracture toughness, and (vii) impact properties.

Tensile modulus and tensile strength

The void effect on tensile properties affect differently in fibre-dominated and matrix-dominated properties. Fibre dominated elastic properties such as longitudinal tensile modulus and poisson's ratio are less sensitive to void presence. Whereas matrix-dominated properties as transverse tensile modulus and out-of-plane tensile modulus are more sensitive to voids. Different work have analysed the voids effect on UD carbon-epoxy materials [Harper 1987; Stamopoulos 2016] manufactured by prepreg, showing no sensitivity in the longitudinal tensile modulus. The NCF carbon-epoxy material manufactured by RTM shows the same result [S. Sisodia 2015; Xu 2014]. However, the transverse tensile modulus for carbon-epoxy NCF is reduced 15% with 5% of void content [Varna 1995]. Experimental results about the reduction in out-of-plane tensile modulus shows a reduction of 10% by increasing 1% the void content [Guerdal 1991]. In the literature has been detected a negligible influence of the reduction of tensile strength for fabrics of NCF carbon-epoxy manufactured by RTM [Protz 2015; S. Sisodia 2015].

Intra-laminar shear modulus

The in-plane shear modulus and out-of-plane shear modulus are both matrix-dominated properties; therefore, the void content has a severe impact on the reduction of these properties. Numerical result showed [H. Huang 2005] a 6-7% drop in G_{12} for 5% increase in void content in UD carbon-epoxy. A different work shows how reduction of 10% in the in-plane shear modulus for UD carbon-epoxy parts with 1% of voids subjected to torsion [Hancox 1977]. Above this 1% void content, the authors demonstrate a severe shear modulus drop, reducing in 70% the modulus with 5% of void content. Experimental work show that the out-of-plane tensile modulus, are sensitive to void content as 1% increase in void content leads to a 10% reduction [Guerdal 1991].

Compression modulus and strength

Only two work have been found that analyse the void effect in CF-Epoxy prepreg under compression loads. One of the results [Hernández 2013] showed a small effect of voids in compression modulus whereas the second work [Cinquin 2007] observed a linear drop in compression modulus. Obtaining for 6% of the void content a decrease of 9% in the modulus. Voids affect the compression failure as they can cause fibre misalignment and longitudinal fibre debonding inside the composite part [Hernández 2013]. For UD CF-Epoxy laminates a reduction of 11% in compression strength for 4% of void content [Uhl 1988] and a reduction of 16% with 6% of void content have been found [Cinquin 2007]. In the case of woven CF-epoxy laminates, a reduction of 10% and 19% of compression strength with a percentage of voids of 4% have been published [Hernández 2013]. The effect of void content in the transverse compressive strength has been less studied in

the literature. A numerical study shows that 1% void content is able to reduce the strength by 15% in dominant transverse load [Vajari 2014].

Flexural modulus and strength

In order to understand the voids effect in the flexural performance it is necessary to analyse the void influence on ILSS, tensile strength and compression strength [Mehdikhani 2019]. The void effect on the flexural modulus of UD CF-epoxy laminates manufactured by Prepeg autoclave is analysed in the literature. A reduction of 25% for 5% of void content [Kakakasery 2015] and a decrease of 10% for 1% of void content [L. Liu 2006] has been published. A similar decrease of flexural modulus in a multidirectional NCF CF-Epoxy manufactured by RTM is reported [Montoro 2011]. When flexural failure strength is analyse, a loss of 20% with 2.5% of voids [L. Liu 2006] and 17% reduction with 3% increase in voids is found [Stamopoulos 2016] for CF-epoxy Prepeg laminates.

Inter-laminar shear strength (ILSS)

The most studied property in the literature is the Inter-Laminar Shear Strength (ILSS), as it is a matrix-dominated property that is very sensitive to void defects [Mehdikhani 2019]. In the UD fabrics manufactured by prepreg-autoclave, this reduction have been cuantified by the following way: an almost linear reduction of 6% for each 1% in void content [L. Liu 2006], a reduction of 50% in the case of 7% void content [J. M. Tang 1987], 10% decrease of ILSS by 1% increase of void content [Ghiorse 1993].

In the case of Woven fabrics manufactured by prepeg-autoclave manufacturing techniques, a reduction of almost 15% for a 3% void content [Tretiak 2022] and a reduction of 25% for a 6% of void content have been found [Di Landro 2017]. The effect of void content on composite parts manufactured by RTM showed a reduction of ILSS of 7% for harness laminated and 4% for plain weave laminate by each 1% void content. Several authors have concluded that the sensitivity of the ILSS to voids is due to a reduction of the inter-laminar area as well as the concentration of stresses around the voids [Mehdikhani 2019; Wisnom 1996].

Inter-laminar fracture toughness

Inter-laminar fracture toughness is the required energy in the creation of new surface area in delamination. It is also known as critical strain energy release rate or delamination toughness. Inter-laminar fracture toughness of a composite can be measured in each of the modes of crack propagation that contemplates the mechanics of the fracture: mode I (normal opening), mode II (Sliding shear) and mode III (tearing shear).

The contribution of mode III, however, is considered irrelevant to the delamination phenomenon [Jensen 2001], because the energy in this mode is much higher that the other modes [Robinson 2000]. Therefore, the delamination phenomenon in a composite material

is considered the combination and mixed-mode of mode I and mode II crack propagation [Tay 2003]. It has been observed that in the void presence, two different phenomena occurs. Firstly, the voids enable the initiation and propagation of the crack, as they are free surfaces. On the other hand, they obstruct the crack increasing its surface, and blunting the crack tip [Mehdikhani 2019]. There is no clear agreement in the literature about void effects on inter-laminar fracture thoughness. A paper that analyses the void effect in CF-Epoxy prepeg laminated states that there is no clear effect in the fracture thoughness at crack initiation in any fracture mode [Asp 1997]. The same authors confirm an increase of 75% of the fracture thoughness at propagation in mode I in presence of voids. A study about the effect in infused NCF CF-Epoxy laminates compares a totally degassed and post bleeded part with no degassed composite part without quantifying the void content [Carraro 2015b]. The results show higher Mode I inter-laminar fracture toughness in parts with high void content in crack initiation and crack propagation.

Impact properties

It is proved that voids have greater effects on the reduction of out-of-plane properties than in-plane properties [H. Huang 2005]. The effect of voids on out-of-plane impacts has been studied only at low-energy impacts: less than 1 J [Kakakasery 2015; Kousourakis 2006] and less than 6 J [Arthurs 2015]. The results were not entirely conclusive since they showed that the voids could facilitate the initiation and propagation of crack, but at the same time could stop propagation due to plastification of the matrix. One of the limitations of these studies is that they were focused at very low impact energies. In addition, all reviewed studies used prepeg composites where voids (mostly intra-laminar) were generated by curing cycle modification. No studies have been found about the effect of voids on out-of-plane impacts in NCF-RTM composites.

2.3 Property-Performance

This section covers several studies carried out on composite materials for the prediction of final product performance **(Property-Performance)**. Since out-of-plane impact is a critical event in composite materials, the study focuses on different approaches to the modelling of such impacts.

NCF composites manufactured by RTM, which are suitable for out-of-plane impacts, need predictive models that take into account the different failure mechanisms [Greve 2006]. However, the failure mechanisms of composite materials differ from those of metal structures.

Depending on the level of abstraction, models have been developed at different scales (Figure 2.11): 1D Spring-mass model, 2D Plate model, 3D macro-mechanical model, 3D meso-mechanical model and 3D micro-mechanical model [Bogenfeld 2018].

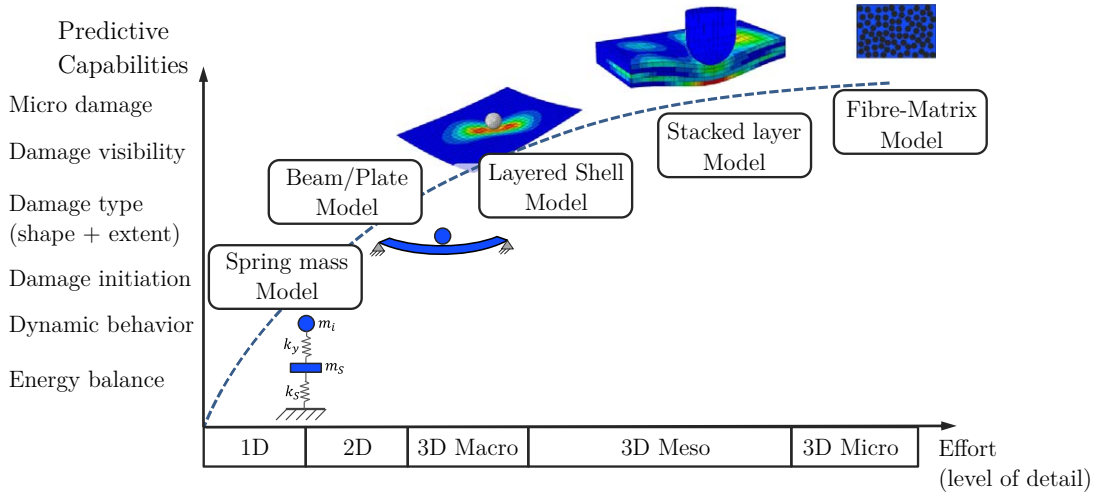

Figure 2.11: Impact methods for different scales [Bogenfeld 2018].

1D models based on the Spring-mass principle were the first analytical models developed. These models were based on simple multi-body systems composed of different masses and springs [Abrate 1991; Christoforou 1998]. They allowed to predict the elastic response of the part during impact as a function of deformations, contact times and maximum contact force. However, they were only useful for sub-critical impact energies that did not cause damage to the material. The first to include delamination damage to the analytical were Olson *et al.* [Olsson 1992], who introduced stiffness reduction systems to spring-mass models. It was Olson [Olsson 2001] again who proposed a 2D orthotropic plate model impacted by a hemispherical impactor. This was based on the approach proposed by Dobyns [Dobyns 1981] years earlier and proved to be more accurate than the 1D model.

However, the analytical models described have limitations due to a multitude of simplifying assumptions. Models based on the Finite Element Method (FEM) allow predicting impact problems in a more realistic way, as they allow considering loading, frictional contact, damage and other phenomena [Shah 2019].

The most simplified case in the multi-scale modeling is the so-called 3D macro-mechanical model and has a relatively low computational cost. In this case, the laminate is considered as a homogeneous material and is modelled using shell elements or continuum elements [González 2017]. In this case intra-laminar damage is considered using the Continuum Damage Mechanics (CDM) approach [Dávila 2005; Maimí 2007]. However, this approach does not take into account the phenomenon of delamination.

3D meso-mechanical model method considers each of the plies as homogeneous solids and models the interaction between the adjacent plies. Therefore, ply-associated damage and delamination-associated damage are introduced separately, referred as intra-laminar damage and inter-laminar damage, respectively. Most of the recent publications on

out-of-plane impact modelling use this modelling approach due to high accuracy and affordable computational time [Bogenfeld 2018].

3D micro-mechanical model is based on the modelling of the individual fibres and the surrounding matrix. Considering the fibre shapes, volume fraction and spatial distribution it is possible to predict the performance of the composite for different load cases [Okereke 2014; Zhang 2010]. However, this method is not suitable for simulating out-of-plane impact cases because the computational cost is too high.

Reviewing the works in the literature, it can be stated that the most commonly used method is the 3D meso-mechanical model [Bogenfeld 2018]. This approach allows the prediction of impact behaviour, considering the different failure mechanisms, in a very accurate way and with affordable computational costs. In the following section, Section 2.3.1, the aim is to further investigate 3D meso-mechanical approach. To this end, it is explained how both intra-laminar damage and inter-laminar damage are modelled. In addition, the relevant modelling considerations are reviewed.

2.3.1 Impact damage modeling

In out-of-plane impacts, two types of failure occur: (i) matrix cracking and/or fibre breakage, and (ii) delamination between plies [Lopes 2014]. Due to the complexity of damage modelling, the 3D meso-mechanical approach considers intra-laminar damage and inter-laminar damage separately. The shells represent each composite layer and are modelled as a layer of orthotropic elastic material that includes intra-laminar damage due to micro-cracking of the fibre and matrix [Dassault Systèmes 2021]. In addition, the laminates are bonded together by a cohesive zone, either by elements or by surface, which is capable of modelling interlaminar damage or delamination.

Initiation and evolution of Intra-laminar damage

For the modelling of intra-laminar damage, different failure criteria have been developed. These criteria can be classified into two subgroups referred to as failure criteria that do and do not consider the interactions between the different stress components [Nali 2012].

On the other hand, failure criteria that do consider interactions between different stress components can be classified into two subgroups. In the first subgroup, there are the criteria that propose a single equation encompassing the different stress components: The Hoffman [Hoffman 1967], Tsai–Wu [Tsai 1971], Liu–Tsai [K. S. Liu 1998] and Tsai–Hill [Hill 1965; Tsai 1971]. With regard to the second subgroup, there are the criteria that combine interacting and non-interacting conditions: Hashin and Rotem [Hashin 1973], Hashin [Hashin 1980], Puck and Schürmann [Puck 1998], LaRC03 [Dávila 2003] and LaRC04 [Pinho 2005].

For the modelling of out-of-plane impact, different damage initiation criteria have been adopted. The most frequent are the Larc04 and Hashin Linear softening based on equivalent displacement criteria.

Once the damage criterion is reached (Figure 2.12a-point A), the material is considered to be damaged. This is controlled by different damage parameters ranging from 0 (no damage) to 1 (total damage). This damage evolution can be modelled using different softening laws, such as; linear, bi-linear, exponential and power law [Xue 2021]. This approach considers the fracture energy of each failure mode and translates it into the equivalent displacement [Camanho 2002].

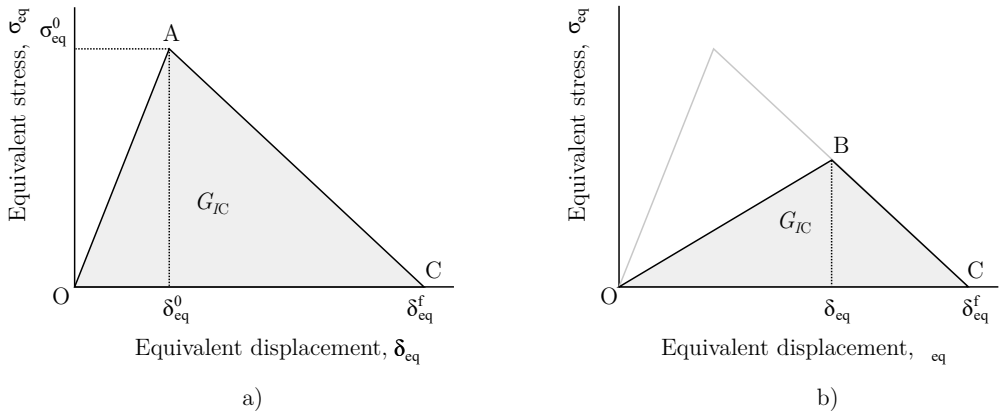

Figure 2.12: Intra-laminar failure behaviour a)before damage, and b) after damage occurs.

Initiation and evolution of Inter-laminar damage

Two main strategies are known for the modelling of inter-laminar delamination: models based on fracture mechanics and models based on Continuum Damage Mechanics (CDM) [Tay 2003]. Among the models based on fracture mechanics the so-called Virtual Crack Closure Technique (VCCT) stands out, and they are able to predict crack propagation accurately. However, this method is based on the modelling of a known crack and is therefore not as useful for predicting damage initiation [Turon 2018].

CDM based models are able to model the initiation and propagation of a crack within a potential crack plane, which is the inter-laminar plane in the case of composites [Camanho 2003; Pinho 2005; Aymerich 2009]. Turon and Camanho proposed a bi-liner law to model the interfacial behaviour. Hence, two regions are considered: (i) a linear-elastic response defined by a stiffness parameter K, and (ii) once the maximum supported stress is reached, the material initiate to gradually lose stiffness until total unbonding (Figure 2.13).

Damage initiation is followed by damage propagation and this can be modelled by considering the displacement or dissipated energy. Energy-based criteria are most

commonly used in impact modelling and are based on fracture toughness to determine damage propagation in mixed mode I/II [Turon 2018]. The most commonly used criteria are the power law and the Benzeggagh-Kenane (B-K) criterion [Kenane 1997].

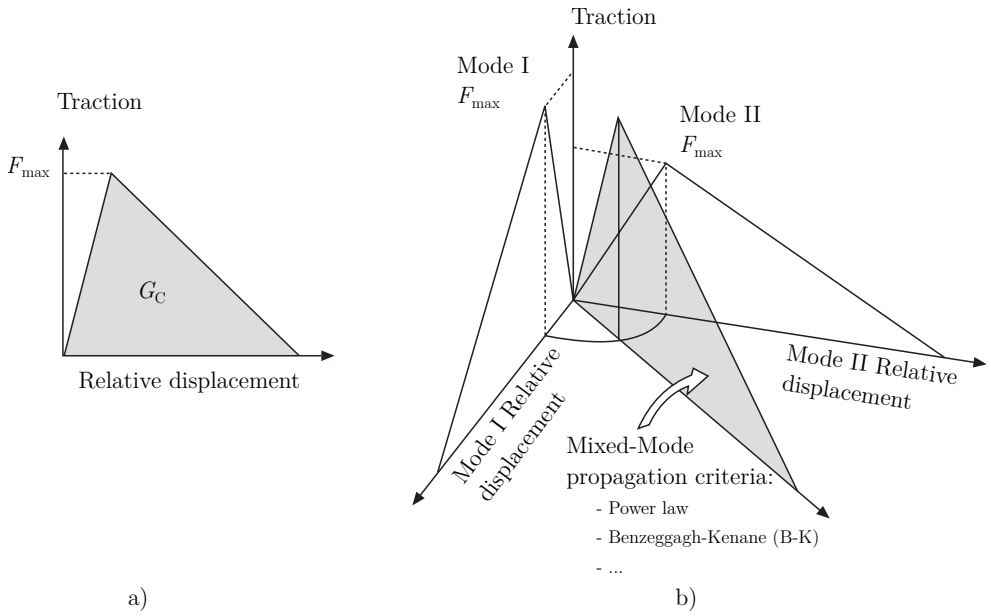

Figure 2.13: Bi-linear traction displacement relationship for: a) single mode, and b) mixed mode [Hallett 2008].

2.3.2 Impact modeling considerations

For the development of an accurate predictive model, reliable material data are essential and and those are obtained according to ASTM standards. Young's modulus and maximum strength in the longitudinal and transverse directions are obtained by ASTM D3039-07. In the same way, it is possible to quantify the principal Poisson's ratio. In case of compression loads, the modulus and compression strength for the longitudinal and transverse directions are characterised by the ASTM D3410-03. For the shear properties, both the shear modulus and the shear strength, ASTM D3518-18 is usually used. Intra-laminar fracture energies in longitudinal and transversal direction for tensile and compressive loads can be obtained following the experimental procedure described by Pinho *et al.* [Pinho 2005]. The inter-laminar properties, the fracture energies in mode I and mode II are obtained using ASTM D5528-13 and the procedure described by Martin *et al.* [Martin 1999], respectively. Besides, The Benzeggagh-Kenane (B-K) interaction requires the characterisation of the B-K coefficient. This is possible by means of the Mixed-Mode Bending (MMB) test method, standardised by ASTM D6671-01.

It has been shown in the literature that reduced integration elements can be effective in reducing the bending locking effect caused in meso-scale models [Laulusa 2006]. One of the most commonly used elements are the continuum shell elements (called SC8R in

Abaqus®), as they allow bending loads to be taken into account [Bogenfeld 2018]. This are a 8-node first-order hexahedral continuum shell elements with reduced integration (SC8R) and are suitable for out-of-plane impacts [Heimbs 2014].

The cohesive zones that bond the plies together can be modelled using cohesive surfaces or cohesive elements. In the case of cohesive surfaces, the cohesive constraint is enforced at each slave node as contact problem. On the other hand, in the case of cohesive elements, the cohesive behaviour is discretised by means of discrete elements. Both techniques provide good results in the modelling of inter-laminar delamination, but several studies have preferred the implementation of cohesive elements due to their accuracy in impact modelling [Turon 2018].

2.4 PSPP-based Digital Twin

Historically, the physical product and the virtual product have been developed and analysed separately. In the virtual world, both the manufacturing process and the subsequent mechanical behaviour of the manufactured parts are simulated for optimisation purposes. The product is manufactured and subsequently characterised in order to understand the real state and mechanical behaviour of the product. The new digital revolution that is taking place in the 21st century aims to combine both, the physical and the virtual elements in order to generate the so-called Digital Twin (DT). DT integrates multiphysics, multiscale and probabilistic simulations with sensor updates to obtain a highly accurate virtual representation of the physical process/product updated in real time [Glaessgen 2012].

Uncertainty in manufacturing processes is inevitable, and even more in processes such as composites [Henning 2014; Heieck 2017; Mayer 2016a]. Therefore, DT aims to incorporate the uncertainties and potential defects generated from the production stages to the performance of the final product [Kärger 2015; Mayer 2016b]. For the specific case of composite materials, the DT must be able to predict and integrate the defects induced in the process (fibre undulations, voids...) and transfer them to the subsequent stages until the final performance of the product. Therefore, the generation of reliable simulation models, suitable material characterisations methods and the connections between the models themselves are of vital importance [Henning 2019]. In this way, the Digital Twin will give a much more realistic view of the part and provide information on "as manufactured" in contrast to "as designed" [Heinecke 2018]. Furthermore, by considering defects in the prediction of product performance, it is possible to distinguish relevant defects from irrelevant ones. This is a paradigm shift, since by replacing quality-based criteria with product performance-based criteria, it is possible to reduce the level of defectiveness.

For this, a deep knowledge in materials science and more specifically in the Process-Structure-Propert-Performance-Performance (PSPP) relationship is necessary [G. B.

Olson 1997]. Where the cause-effect relationship is realised through three main links. The Processing-Structure link relates the process parameters directly to the structural model of the material at either the nanoscale, microscale, mesoscale or macroscale. The second link, the structure-property link, relates the effect of the structure to each of the physical, chemical and mechanical properties. Finally, the property-performance link determines the properties of a material under specific operating conditions and environmental effects [Agrawal 2016].

For the creation of these PSPP based Digital Twins, different methods based on the Virtual Process chain have appeared. This approach consists of the concatenation of diferent FEM models, with the aim of predicting the final performance of the manufactured part. In the pioner work carried out by Allison *et al.* [Allison 2006], the aluminium casting process steps were integrated: from the thermal data obtained in the process, the microstructural characteristics of micro-porosity, eutectic phases and precipitate phases were predicted (process-structure link), this microstructure information was used for the prediction of the mechanical properties of yield strength and fatigue stength (structure-property link), and finally, these mechanical properties were used for the prediction of residual stresses and durability of an engine block. In the same way, works have been found where virtual process chains were generated for final part performance prediction considering residual stresses after forging [Tersing 2012], after AM process [O'Brien 2021] and after oil quenching heat treatments [Afazov 2021]. For composite materials, it has been demostrated that textile draping can generate local defects that affect the mechanical performance, and therefore, these defects should be considered in structural simulations using continuous process chains [Kärger 2015; Kärger 2018].

However, physics-based simulations involve very high computational times. This limits their use to the design phase only, as it is unfeasible to implement them in the in-line process [Henning 2019]. As a solution to this challenge, new data-driven approaches have emerged in the last years. Machine Learning (ML) methods, which is a technology within Artificial Intelligence field, have proven to be efficient in finding complex patterns within all types of data [Vieira 2019]. They are called predictive models and are suitable for the integration within the DT mainly for two reasons. First, they allow in-depth analysis of all monitoring data in real time in order to detect and correct disturbances [Wuest 2016]. And second, ML-based surrogate models, which are computationally simpler models, can be very useful to perform real-time simulations [Bárkányi 2021]. Thus, ML-powered DT technology is expected to provide demand-driven manufacturing with the ability to operate in real-time for the multi-objective optimisation [Z. Huang 2021].

2.4.1 Machine Learning for Digital Twin

Machine learning is a subfield of artificial intelligence that focuses on the development of learning algorithms that allow acquiring "knowledge" from data in order to make future decisions. This method is the evolution of automation, where the human is not needed to generate models from large amounts of data [Raschka 2019]. This technology is not new; it has simply been enhanced by advances in computer technology, which allow the store and process large amount of data [Alpaydin 2010]. Four methods can be distinguished within the ML technology: supervised learning, unsupervised learning, semi-supervised learning and Reinforcement Learning. The predictive model must be generated using the appropriate method and algorithm or combination of algorithms, which depends on the nature of the problem and the type of data [Pham 2005]. Since manufacturing data is frequently labeled and expert judgment is available, supervised machine learning was identified to be the greatest fit for the challenges and problems encountered in manufacturing applications [Wuest 2016; Lu 1990]. The main types of supervised algorithms used are shown in table 2.1.

Table 2.1: Most used supervised learning algorithms for composite materials.

	Class	Name
Individual		Decision trees (DT)
		Support Vector Machine (SVM)
		Kriging or Gaussian Process Regression (GPR)
		Gaussian Process Classification (GPC)
		k-Nearest Neighbors (KNN)
		Logistic Regression (LR)
		Naive Bayes (NB)
Ensemble	Boosting	Gradient Boosting Machine (GBM)
		eXtreme Gradient Boosting (XGBoost)
		AdaBoost
		LightGBM
		CatBoost
	Bagging	Meta-bagging
		Random Forest (RF)
	Stacking	Many individual models stacking
Deep Learning	Convolutional	Convolutional Neural Network (CNN)
	Recurrent	Long short-term memory (LSTM)
	ANN	Artificial Neural Network (ANN)

2.4.2 Supervised learning for composite material

Due to the great advances in ML and data-driven methods, many areas of science and engineering have started to apply it for different applications. In the area of composite materials, supervised methods have been widely used [Gomez 2021; C. T. Chen 2019;

Sharma 2021]. The different applications can be classified according to the PSPP approach, i.e. they are classified according to the generated linkage process-structure, structure-property and property-performance.

ML-based Process-Structure linkage for composite materials

ML methods have been used for a multitude of polymer matrix composite manufacturing processes. In the textile draping process, ML has been used to quantify the maximum shear angle [Pfrommer 2018; Zimmerling 2019]. In the pultrusion process, by measuring the pull speed and mold temperature at various points, it was possible to predict the composite temperature and degree of cure using ANNs [X. Chen 2010; X. Chen 2012]. Hurkamp *et al.* [Hürkamp 2020] applied ML to the thermoforming process of continuous fiber-reinforced thermoplastic sheets (Organosheet) with a thermoplastic overmoulding process. They used bagging ensemble methods (Adaboost, RF and XGBoost) to predict the temperature distribution of the part and thereby the bonding quality. In the Automated fibre placement (ATL) process, ML-based predictive models have been widely used to detect the different types of defects generated [Sacco 2020; Meister 2021].

Regarding RTM, several authors used the pressure signal and a CNN model to detect permeability variations [González 2020] and dry zones [Stieber 2021]. In this way, an online evaluation of the quality of the impregnation can be developed. Matsuzaki *et al.* [Matsuzaki 2021], proposed an ANN-based predictive model for resin flow impregnation prediction in a RTM process, computationally less expensive than traditional FEM models. Furthermore, for the curing phase, ML-based models have proven to be valid for the prediction of the degree of curing of the composite during the curing process [Aleksendrić 2015].

ML-based Structure-Property linkage for composite materials

Recent studies have shown that it is possible to predict the elastic mechanical properties of a composite by knowing its microstructural configuration. This was very useful for design optimisation [Gu 2018; Liu 2015], as well as for post-process property prediction [Ye 2019; Qi 2019; Z. Yang 2019]. As these were grid-based inputs, which would be the same as an image with pixels, the authors mostly used deep learning methods of the CNN type. Seythan *et al.* [Seyhan 2005] employed ANN for the prediction of compressive strength property, knowing the composite structure (in terms of fibre volume, thickness and amount of binder) generated during the VARTM process. In addition to mechanical properties, ML methods have been used to relate the structural properties of the composite to thermal properties, such as thermal conductivity [Rong 2019].

ML-based Property-Performance linkage for composite materials

In the case of failure analysis, ML-based predictive models have been used for structural health monitoring (SHM) and non-destructive testing (NDT). For SHM, ML has enabled the detection of structural behaviour and failure during product performance. Detection of delamination during loading using sensors and ML has been shown to be possible [Kesavan 2008], as well as prediction of damage tolerance in out-of-plane impacts using Acoustic emission and ANN [Ramasamy 2014]. Similarly, using ML-enhanced NDT techniques it was possible to detect the defect location and its its typology; by means of ultrasound with ANN [Barry 2016] and with k-means [You 2016], Dielectric sensors with RF [Elenchezhian 2018], and thermography with k-means [Marani 2018].

The nonlinear behavior exhibited by composite materials is often caused by one or more nonlinear mechanisms at the microscale, where plasticity, viscoelasticity and damage are the most prominent. As it is often not feasible to obtain a constitutive model from experimental tests, several studies have been published for the constitutive modeling of composite materials by ML methods [Xin Liu 2021]. The computational time of nonlinear physics-based models is often high and it is not feasible to solve them during the process. Therefore, surrogate ML-based models, also known as metamodels or emulators, can be a powerful solution [Bárkányi 2021]. For stress-strain analysis, ML-based surrogate models have proven to be useful for the modelling of nonlinear constitutive models of composite materials. Studies have used ML for the prediction of elastoplasticity (stress-strain curve) [Lefik 2003; Wu 2020; Mozaffar 2019], hyperelasticity [Nguyen-Thanh 2020; Im 2021] and viscoelasticity [Yuan 2018] in composite materials. In the same way, surrogated ML-based models have been used to predict the performance of an open hole plate [Yan 2020] or buckling perfomance prediction [Wagner 2019], among others. In the case of surrogated out-of-plane impact models, only studies analysing the effect of laminate and impactor angle have been found [Mukhopadhyay 2021].

2.5 Critical study of the state of the art

RTM processes are becoming more popular because they provide great adaptability and rapid cycle times at a reasonable cost. Nonetheless, as compared to prepreg procedures, they still lack much of the robustness and reliability required to maintain consistent product quality. The intrinsic uncertainty associated with RTM processes leads to the generation of scrap with consequences on the manufacturing cost and the environment. Hence, the potential of composites is not exploited, as more conservative designs are used in addition to costly rework and scrap actions [Potter 2009].

The variations in textil geometry have shown to be critical [Mesogitis 2014] as it affects the permeability and consequently the local pattern of resin impregnation [Bodaghi 2019b]. Among the variations in textil geometry that affect permeability stitching,

shearing nesting or binder have shown to be critical. The permeability variations alter the local velocities of the impregnation, generating defects in the material. These RTM process-induced defects, and in particular voids make challenging to achieve the quality standards of the robust autoclave process.

The effect of voids on mechanical properties

Understanding void minimisation strategies and quantifying the effect of voids on mechanical performance is essential to manufacture zero-defect parts and achieve the robustness required by the industry [Hamidi 2018].

Many papers can be found in the literature demonstrating the importance of void reduction, and analysing the effect of void content on different mechanical properties. The consensus in the literature is that matrix-dominated properties are clearly affected by the void content, whereas in the fibre-dominated properties the effect is not so evident [Liu 2016]. The majority of these studies are related to prepreg textiles, where voids are generated by modifying the consolidation pressure [Mehdikhani 2019]. There are few works available about the effect of voids on the reduction of mechanical properties of NCF manufactured with RTM. To date, the detrimental effect of voids in NCF-LCM composites has been demonstrated in the following matrix-dominated properties: compression modulus and strength [Kosmann 2015], flexural modulus and strength [Montoro 2011], fatigue strength [S. Sisodia 2015; Protz 2015], and inter-laminar fracture toughness [Carraro 2015a]. Conversely, a minor or negligible reduction has been observed in the fibre-dominated properties such as longitudinal tensile modulus and strength [S. Sisodia 2015]. Likewise, it is proved that voids have greater effects on the reduction of out-of-plane properties than in-plane properties [H. Huang 2005]. The effect of voids on out-of-plane impacts has been studied only at low-energy impacts: less than 1 J [Kakakasery 2015; Kousourakis 2006] and less than 6 J [Arthurs 2015]. The results were not entirely conclusive since they showed that the voids could facilitate the initiation and propagation of crack, but at the same time could stop propagation due to plastification of the matrix. One of the limitations of these studies is that they were focused at very low impact energies. In addition, all reviewed studies used prepeg composites where voids (mostly intra-laminar) were generated by curing cycle modification. No studies have been found about the effect of voids on out-of-plane impacts in NCF-RTM composites.

Numerical modelling

Reliable in-line quality inspections, based on Digital Twins of the manufacturing process, have proven to be a promising strategy in identifying and reducing defects. Digital replicas of the physical process are developed by continuously collecting process data, enabling the detection of defects generated and their possible consequences [Hürkamp 2020]. For that, the manufacturing system must be enhanced with material science and process

technology intelligence, and stablish accurate Processing–Structure–Property–Performance (PSPP) relationships.

The PSPP approach has been used to generate a so-called virtual process chain (CAE chain) capable of continuously simulating the RTM process of CFRP parts [Kärger 2015]. It has been shown that through holistic simulation with FEM-based data exchange, it is possible to predict in-service performance using process information. However, no evidence has been published of any virtual process chain which integrates impregnation void defects into RTM processes. Additionally, it should be noted that no out-of-plane impact models have been found that consider the effect of voids generated during RTM processes.

Furthermore, CAE chains based on FEM concatenation are computationally expensive and are not suitable for integrating as an on-line quality assessment [Henning 2019]. Consequently, for modelling the whole PSPP relationships, computationally cost-effective models, so-called surrogate models or meta-models, are needed to predict the behaviour of manufactured parts including process-induced defects.

Machine Learning in composite materials

Among surrogate modelling techniques, Machine Learning (ML) data-driven methods are gaining popularity in composite materials manufacturing. Whereas it has not been used for the entire PSPP composite process chain, it has been widely used for individual links in the PSPP chain: Process-structure models, structure-property models, and property-performance models.

In manufacturing processes, and especially in composite materials, it has been observed that supervised predictive models can be very effective. The data can come from experimental or numerical sources, so-called synthetic data. Although it is true that deep learning predictive models based on neural networks play an important role, the type of input data used is often in an unstructured format (image, text, etc.). It has been seen that for input data with a structured format, time series for example, traditional ML models shown a good accuracy. Among the models that showed good accuracy are ensemble methods that combine the predictions of weak models to generate a much more robust prediction.

3 Objectives

3.1 Main objective and technical objectives

The main objective of the present thesis was the development of scientific-technological knowledge about the Digital Twin generation for the RTM process that integrates the filling phase and the final mechanical properties of each part with a high level of fidelity. Based on this main objective, the following technical objectives were defined:

- **Objective I**: Experimental study of the effect of RTM process parameters on void generation (Process-Structure) and the effect of those voids on impact properties (Structure-Property). This involves the characterisation of the impregnation stage for the generation of plates with a homogeneous and controlled void content, followed by an impact behaviour assessment, by means of instrumented impact test, fractography and NDT analysis.
- **Objective II**: Development and validation of a ML methodology for diagnosing the quality of composite parts manufactured by RTM (Process-Structure). This involves the generation of a synthetic dataset based on reliable FEM models, data pre-processing, training and evaluation of the predictive models.
- **Objective III**: Development of a ML-based surrogate model of impact event which takes into account manufacturing defects (Structure-Property-Performance). This model builds a fast quality assessment system based on real in service performance and covers the generation of a numerical model that simulates the out-of-plane impact for as-manufactured composite plates, the synthetic dataset generation, data pre-processing, model training and final predictive model evaluation. The predictive model will be based on supervised learning, for classification, as well as single and multi-output regression.

4

Effect of voids on the impact properties

Contents

4.1 Introduction

The importance of void reduction has been extensively reported in the literature, as well as the effect of such defects on different mechanical properties. One of the most recurring observations is that matrix-dominated properties are affected by the occurrence of voids, whereas fibre-dominated properties are barely affected [Liu 2016]. The majority of these studies were related to prepreg textiles, where voids were generated by modifying the consolidation pressure [Mehdikhani 2019]. There are few works available about the effect of voids on the reduction of mechanical properties of NCF manufactured with RTM. Although NCFs have a potential for use in high-performance composites, they have certain features that influence the final performance. It is therefore necessary to investigate the behaviour of NCFs for different loading conditions.

This chapter presents a study on the effect of RTM process parameters on void generation and voids effect on out-of-plane impacts (drop-weight impact test) of CF-Epoxy NCF laminates. In this way, it was possible to quantify and experimentally confirm the effect of voids on out-of-plane impacts. To this end, a practical methodology similar to that used by Leclerc and Ruiz [Leclerc 2008] was followed. The mechanism of void formation in RTM variants was studied to find the method that minimised the formation of voids, and subsequently, samples with different levels of voids were fabricated. These samples were used to study the impact performance for subcritical and supercritical impacts.

In this way, two links of the PSPP chain were generated (Figure 4.1). First, the Process-Structure link was completed by relating the RTM processes with the generated void content. Then, the effect of void content on the impact properties was analysed, thus completing the Structure-Properties link.

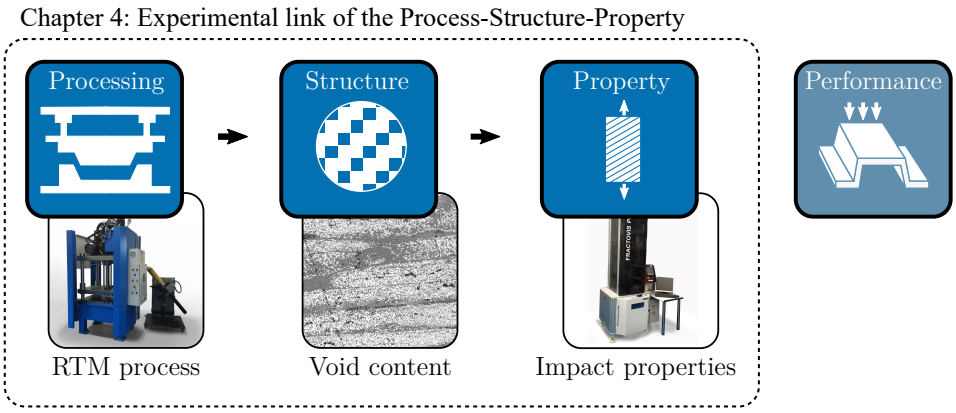

Figure 4.1: Experimental Process-Structure-Property link.

4.2 Materials and experimental methods

4.2.1 Materials

Symmetric laminates composed of four plies of a biaxial (0/90) NCF of 50k high resistance carbon fibre compacted to 3 mm (reference HPT 610 C090 from SGL) were used in this study. The fibre density and the preform areal weight provided by the manufacturer were 1750 kg/m^3 and 610 g/m^2, respectively.

An epoxy binder powder (Araldite LT 3366 BD) was added, 15 g/m^2 per layer, to maintain the integrity of the preform during cutting, handling and injection. The binder reduced the fraying of the edges during the cutting and handling of the preform, and consequently the risk of race-tracking on the preform edges was greatly reduced. Moreover, the binder kept the net-shaped preform compacted and prevented slippage between the layers during injection [Estrada 2002].

The resin system was composed of a fast curing epoxy resin (Araldite® XB 3585) and hardener (Aradur® 3475) supplied by Hunstman. The properties of the components as well as the proportions of the mixture were taken from the manufacturer data sheet and are shown in table 4.1. Regarding the mixture at room temperature (25 °C), the density was 1161 kg/m^3 whereas the viscosity was 900-1100 mPa s. This resin shows low viscosity at room temperature, however, due to its high reactivity, its viscosity increases rapidly once curing begins. This allows short cure cycles and is suitable for use in RTM processes for mass production of Automotive composites.

Table 4.1: Properties of the resin system.

	Araldite® LY 3585	Aradur® 3475
Parts by weight	100	21
Parts by volume	100	25
Density at 25 °C [g/cm^3]	1.15-1.20	0.92–0.99
Viscosity at 25 °C [mPa s]	6500–9000	5–40

4.2.2 Physical properties

Density

The density of the composite samples, ρ_c, was determined in accordance with the liquid displacement method (ASTM D792-20). This method is based on Archimedes principle, which states that a body immersed in a fluid experiences an upward buoyant force, which is equal to the weight of the fluid that the body displaces. By weighing the composite sample in air w_c, and immersed in distilled water w_i, the mass of the displaced water is obtained ($w_c - w_i$). As the density of the water ρ_w is known, the volume of the immersed part, which is the same of the displaced water, is obtained and consequently the density of the composite sample:

$$\rho_c = \frac{\rho_w w_i}{w_i - w_c} \tag{4.1}$$

Ohaus Galaxy™ 110 (1 mg accuracy) balance was used for all measurements and each sample was measured three times in air and other three times in water.

Fibre, resin and void Volume Fraction

The burn-off method described in ASTM D3171-22 was used to determine the fibre volume fraction, v_f, resin volume fraction, v_r, and the void volume fraction, v_v, of the samples.

Bodaghi *et al.* [Bodaghi 2019a] carried out thermogravimetric measurements to confirm that carbon fibre is stable in the range of 300-500 °C and degrades beyond 900 °C. This way, they demonstrated the suitability of the burn-off method for void content and fibre volume determination in CFRP.

To confirm the suitability of the method with the material used in the present study, resin and fibre samples were burned separately at 450 °C, 500 °C and 550 °C. For each temperature, five fibre samples and five matrix samples were prepared. Each of the matrix and fibre samples was extracted from the muffle at an interval of 1 hour and their mass was measured (Figure 4.2). It can be seen that the carbon fibre was stable and always retained about 98% of its mass. This loss of 2% mass was associated with the removal of sizing, which is a polymer coating used to increase the processability and structural integrity of the fibres. Therefore, it was confirmed that the burn-off method is stable for the material used in this study, as it was not degraded.

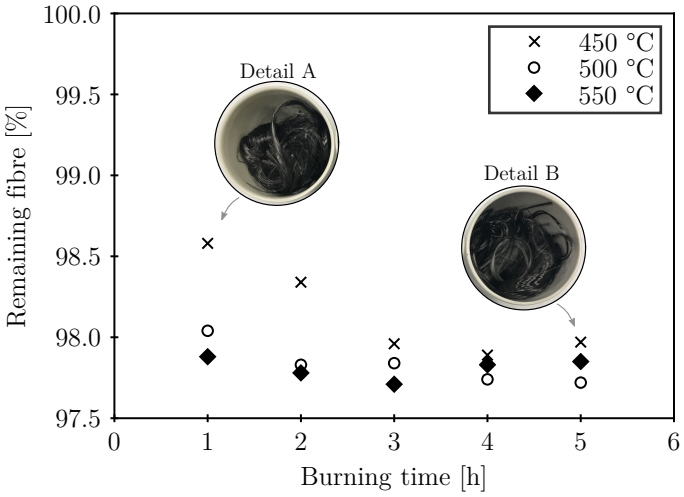

Figure 4.2: Remaining fibre after burn off.

Therefore, for the determination of fibre, resin and void volume fractions the samples to be analysed were burned for 5 h at 500 °C in a muffle. The composite samples were weighted before burning (w_c) and after burning of the matrix, where only fibre was left (w_f).

By means of the manufacturer's theoretical fibre density ρ_f, characterising the density of the matrix ρ_m, and the density of the composite sample ρ_c, it was possible to quantify the fibre v_f, matrix v_m, and void v_v volume fractions:

$$v_f = \frac{V_f}{V_c} = \frac{w_f/\rho_f}{w_c/\rho_c} \tag{4.2}$$

$$v_m = \frac{V_m}{V_c} = \frac{(w_c - w_f)/\rho_m}{w_c/\rho_c} \tag{4.3}$$

$$v_v = 1 - v_f - v_m \tag{4.4}$$

4.2.3 Material characterization

Optimum capillary number, Ca^*_{opt}

Each resin-fabric system has an optimum modified capillary number, Ca^*_{opt}, and is calculated by the following equation:

$$Ca^*_{\text{opt}} = \frac{\mu v_{\text{opt}}}{\gamma \cos\theta} \tag{4.5}$$

where μ is the viscosity of the resin, v_{opt} is the optimum velocity of the flow-front, γ is the surface tension of the resin, and θ is the resin fibre contact angle. In order to obtain the Ca^*_{opt} that ensures the lower void content, these parameters where characterized using the methods described below.

Viscosity

For the determination of the resin viscosity, a Brookfield viscometer was used (PCE-RVI 2 with L2 type spindle). A stirrer placed in the liquid resin measures the increasing torsional resistance of the fluid due to the curing of the resin. However, the high reactivity of the resin at high temperatures made it difficult to determine the Ca^*, as the viscosity increased exponentially over time. Therefore, the resin viscosity was analysed at low temperatures (<40 °C), where it hardly changed over the duration of the tests.

Surface tension

The surface tension was measured by the modified Wilhelmy plate method [Wilhelmy 1863] on a Textechno Favimat equipment. This machine is located at *IMDEA Materials Institute* and the test were performed together with the experts from the same institute. In this method of a thin plate (paper, glass or platinum) is immersed in the liquid to be analysed (Figure 4.3). The plate is pulled up with a thin wire at a slow rate (1 mm/min), and the force on the plate due to the wetting is measured by a tensiometer. While the plate is immersed in the fluid, gravity force F_{g}, buoyancy force F_{b}, and surface tension F_{st} are acting on the plate. Once the plate starts to emerge from the liquid, the buoyancy force decreases to zero. At the last instant of contact between the whole perimeter w of the plate and the liquid, the force is maximum F_{max}, and is the sum of the gravitational force F_{g}, and the surface tension F_{st}:

$$F_{\text{max}} = F_{\text{g}} + F_{\text{st}} = mg + 2w\gamma\cos(\theta) \tag{4.6}$$

where g is the gravitational constant. When the plates emerges from the liquid, F_{g} is the only acting force. Taking the force drop ($F_{\text{max}} - F_{\text{g}}$), and assuming that the contact angle between the plate and the liquid θ is zero, the surface tension γ can be calculated as follows:

$$\gamma = \frac{F_{\max} - F_{\mathrm{g}}}{2w} \tag{4.7}$$

where w is the width of the plate. The original Wilhelmy method uses a platinum plate. However, paper filters are just as effective but much cheaper and more accessible. To ensure that the surface tension is invariable over time, different measurements were taken at different curing times (2 min, 6 min, 12 min, 24 min, 36 min, and 48 min).

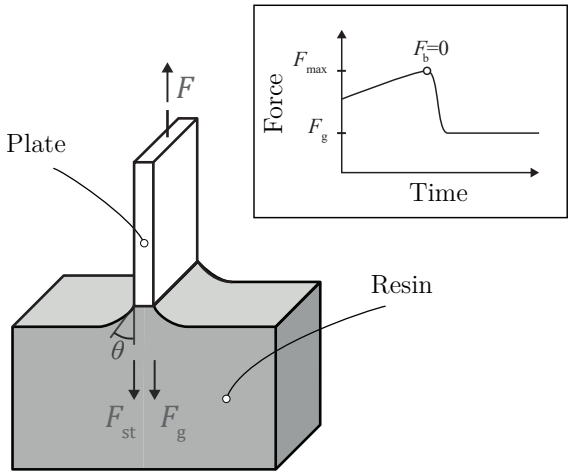

Figure 4.3: Wilhelmy method: prior to the total emersion of the plate $F_{\mathrm{b}} = 0$ [Wilhelmy 1863].

Contact angle

The contact angle between the resin and the fibre was measured by X-ray micro-computed tomography (XCT) (Phoenix Nanotom 160 kV) [Castro 2020]. The machine in question is located at *IMDEA Materials Institute* and the measurements were carried out under the supervision of experts from the centre.

For this purpose, a single carbon fibre tow was placed in a vertical borosilicate glass tube of 0.8 mm diameter and 95 mm height. This tube was placed in a cubic tank containing liquid resin (Figure 4.4). The capillary forces caused the resin to rise and impregnate the carbon fibre tow. The resin was then cured at room temperature for 24 hours. The XCT scanning produced a 3D volume containing 2304 transverse slices with 1180 × 1180 pixels. Several meniscus images were detected, which were processed by means of a Python® code for the segmentation of the air, resin and fibre phases. The contact angle between the fibre and resin was calculated by fitting the meniscus parabola and the fibre line (detail in Figure 4.4).

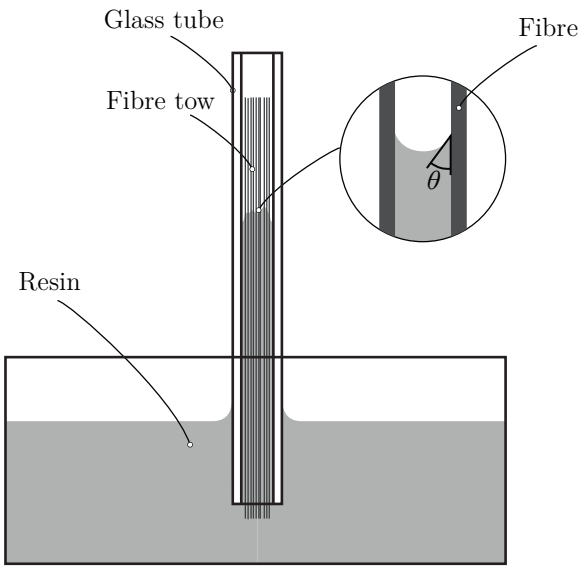

Figure 4.4: Wicking test fixture used for posterior contact angle detection in XCT [Castro 2020].

Void volume at different impregnation velocities

The last step in obtaining the Ca^*_{opt} was the determination of the void content as a function of the impregnation velocity. A strategy of constant pressure injection cannot ensure a constant impregnation velocity during the filling, since the flow-front position increases and thus the pressure gradient and the impregnation velocity are reduced over time. For that reason, in order to obtain an invariable impregnation velocity, a controlled flow-rate injection strategy was chosen [Lystrup 2020]. The theoretical impregnation velocity for a given injection flow-rate Q_{inj}, mould cavity thickness h, mould length y, and porosity ϕ, is calculated according to the following equation:

$$v_{\text{ff}} = \frac{Q_{\text{inj}}}{\phi h y} \tag{4.8}$$

A stainless steel mould was used to manufacture composite plates (Figure 4.5). It was mounted in a hydraulic press (Hidrogarne MV-80) and the plate dimensions were 350 mm $\times$ 250 mm with a thickness of 3 mm. The temperature of the mould was controlled with a hydraulic heater system (Regloplas 300s). The temperature was chosen based on viscosity measurements to ensure a filling time shorter than the gel time. The injection point was connected to the electric injection system (2100cc Series RTM RADIUS Injection System), which controlled the resin injection with a constant flow rate. A preferential channel was placed at the inlet of the cavity to obtain a homogeneous rectilinear impregnation.

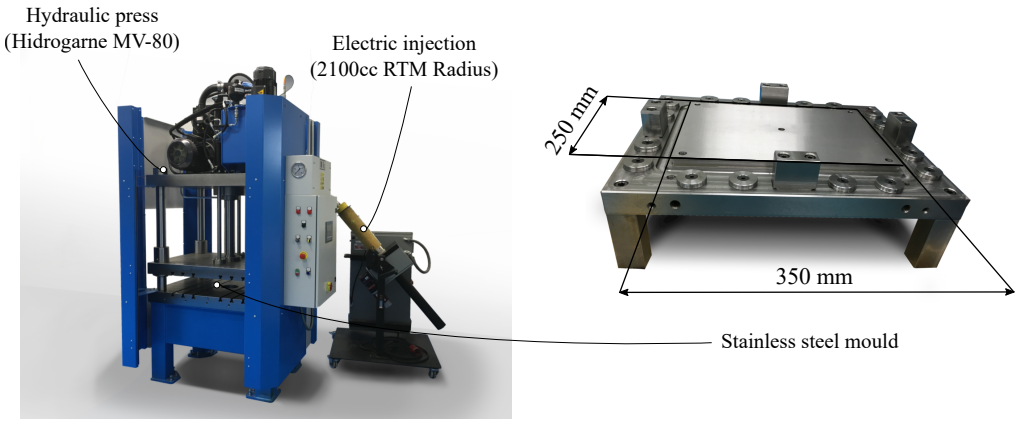

Figure 4.5: Manufacturing system with hydraulic press, electric injection and metallic mould.

From the plate, nine 60 mm × 60 mm specimens were obtained for impact tests. The distribution was 3 rows of 3 specimens as shown in Figure 4.6. To determine the impregnation velocity of these specimens, a velocity control line was assigned to each row. In this way, it was possible to determine the impregnation velocity for each of the specimens. On the other hand, to obtain the void content by burn off in each of the impact specimens, 20 mm × 30 mm specimens were obtained from each of the rows of impact specimens.

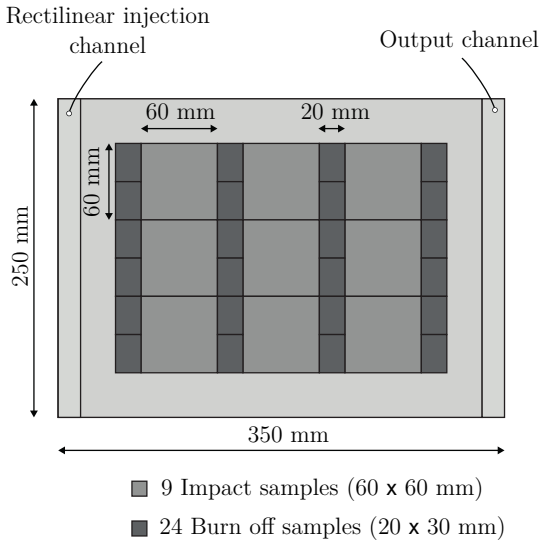

Figure 4.6: Position of specimens throughout the part.

After determining the void content as a function of the impregnation rate, Equation 4.5 was used to calculate the void content as a function of the capillary number. To select the manufacturing conditions, the original intention was to choose four levels of capillary number that would generate four levels of void content. However, it was not possible to obtain plates with void content lower than 1% or higher than 3%. Therefore, the four levels

of voids that were compared were manufactured as explained in table 4.2. The first type of plate ($VARTM_{opt}$) was manufactured with Vacuum Assisted RTM, and the flow front velocity was controlled to ensure the Ca^*_{opt} during the injection. The second case (RTM_{opt}) was similar to the previous case, optimum injection was applied, but without applying the vent for the evacuation of voids. The third case (RTM) was also manufactured using RTM, but in this case non-optimal injection parameters were used, i.e., the flow front velocity was not adjusted to the optimum velocity and no vacuum was applied at the outlet. In the last case Wet Compression Moulding (WCM) was used, since the void content is generally around 4-5% [S. Lee 2021]. A summary of the four techniques used can be found in table 4.2. To obtain a reliable result, at least three plates of each type were produced.

Table 4.2: Strategies used for the manufacture of the CF-Epoxy plates.

	Process	Ca^*_{opt}	Vent
$VARTM_{opt}$	RTM	✓	✓
RTM_{opt}	RTM	✓	-
RTM	RTM	-	-
WCM	WCM	-	-

4.2.4 Drop weight impact test

Low velocity impact tests were carried out at room temperature with a drop weight impact machine (Fractovis-Plus Ceast) (Figure 4.7), where impact energy is defined by setting the impactor mass (m) and height (h_0).

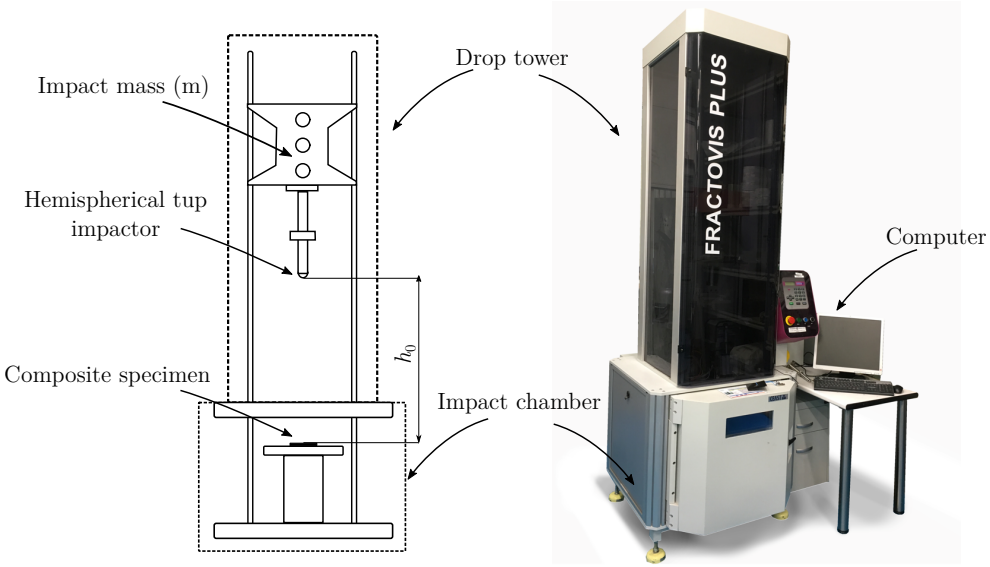

Figure 4.7: Drop weight impact test machine.

The sample was clamped with a circular ring of outer and inner diameter of 60 mm and 40 mm, respectively. In addition, the testing machine was equipped with an anti-rebound system to avoid multiple collisions that could alter the results. A hemispherical metallic striker with a diameter of 20 mm was used, and it was equipped with a 20 kN cell load that enabled the force-time $F(t)$ data during the impact. From the $F(t)$ curve, the dissipated energy $E(t)$, and the deflection of the sample $\delta(t)$ were calculated using the following equations:

$$\delta(t) = \int_0^t [V_i - \frac{1}{m} \int_0^t F(t)\ \mathrm{d}t]\ \mathrm{d}t \tag{4.9}$$

$$E(t) = \int_0^t F(t)[V_i - \frac{1}{m} \int_0^t F(t)\ \mathrm{d}t]\ \mathrm{d}t \tag{4.10}$$

where δ(t) and δ_i are the deflection at time t and initial deflection, V_i is the initial velocity of the impactor which depends on the impactor height h_0, $F(t)$ is the force at time t, and m is the impactor mass.

The delamination threshold energy, E_d, was used to classify the impacts as supercritical or subcritical based on whether the incident energy was above or below this threshold, respectively.

For the characterisation of the residual stiffness curve, the three-test characterisation method defined by Feraboli and Kedward was followed [Feraboli 2004]. The samples were subjected to subcritical impacts (1 J) before and after the damage-inducing impact. The contact time ratios of subcritical impacts were used to obtain the relative residual stiffness curve equivalent to the normalised compression after impact [Feraboli 2006].

4.2.5 Impact damage inspection

Non-destructive ultrasonic inspection

Non-destructive ultrasonic inspections was performed on each impacted specimen in order to determine the shape and area of post-impact delamination. The set-up (Figure 4.8) is composed of: (i) OmniScan MXU portable flaw detector module, (ii) a broadband phased array probe of 64 elements (10 mm × 0.6 mm each) and a center frequency of 5MHz, (iii) Zero-degree wedge for the coupling of acoustic energy in straight-line (iv) two-axis GLIDER™ encoding scanner and, (v) the sample to be tested. Piezoelectric crystals located in the probe expand when they are electrically charged, thus generating an acoustic wave. This ultrasonic wave, travels through the material until it encounters a defect. A part of the wave incident on the interface of the two materials is transmitted and a part is reflected (echo) back to the probe. These defects, which are basically air, have a very low acoustic impedance and practically all the energy incident on it is reflected. By knowing the speed of sound in the tested material and measuring the elapsed time, it is possible to determine the position of the defects in the material. To facilitate the

transmission of the ultrasonic waves between the probe and the composite sample, a high impedance coupling gel was used on the impacted surface. The images generated using the OmniScan MXU module were extracted and by using a Python® image processing code, it was possible to quantify the delaminated area in each sample.

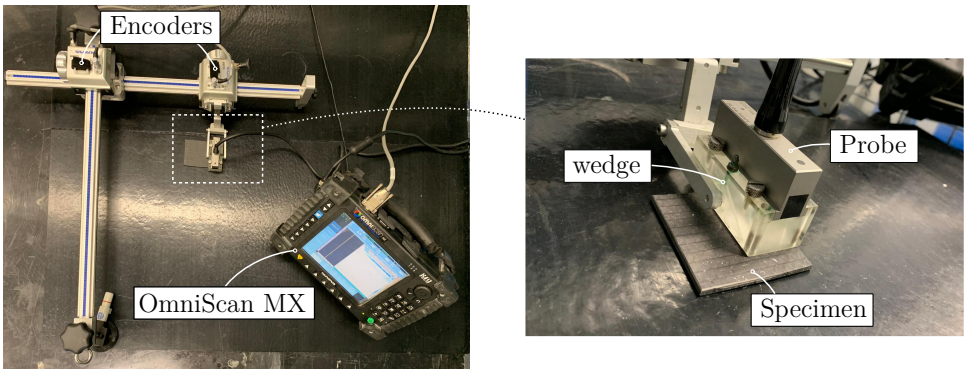

Figure 4.8: Description of the ultrasonic NDT system.

Optical microscope

The microstructure of the cross section of the part was analysed by means of an optical microscope (Leica DM300). 20-magnification lens was used and a scanning was performed along the section. In order to analyse the samples under the microscope, they were first cut on a metallographic saw using an abrasive disc. Afterwards, an initial polishing with silicon carbide abrasive paper and final polishing with a synthetic diamond compound on the inspection face were performed.

4.3 Specimen fabrication

To define the injection conditions, the first step was to characterise the viscosity of the resin and to choose the injection temperature. The following two injection criteria, among others, had to be met: (i) the injection time had to be shorter than the gel time (in order to ensure complete impregnation) and (ii) the viscosity of the resin had to remain relatively constant during injection. The second criterion was established in order to control the Ca^*. By keeping the viscosity constant and controlling the impregnation velocity, it was possible to produce plates of constant Ca^*. As the resin is highly reactive, its viscosity was characterised at low temperatures (20 °C, 30 °C, 40 °C) as shown in Figure 4.9a. In addition, its evolution was analysed in the first 450 seconds, which was sufficient for manufacturing the plates as is demonstrated in the results section. Figure 4.9b shows that the variability of the viscosity is quite low in that time window, 2.79% for 20 °C, 7.75%

for 30 °C, and 14.19% for 40 °C. Therefore, the temperature chosen for the manufacturing the plates was 40 °C, with a viscosity of 613 ± 87 mPa s.

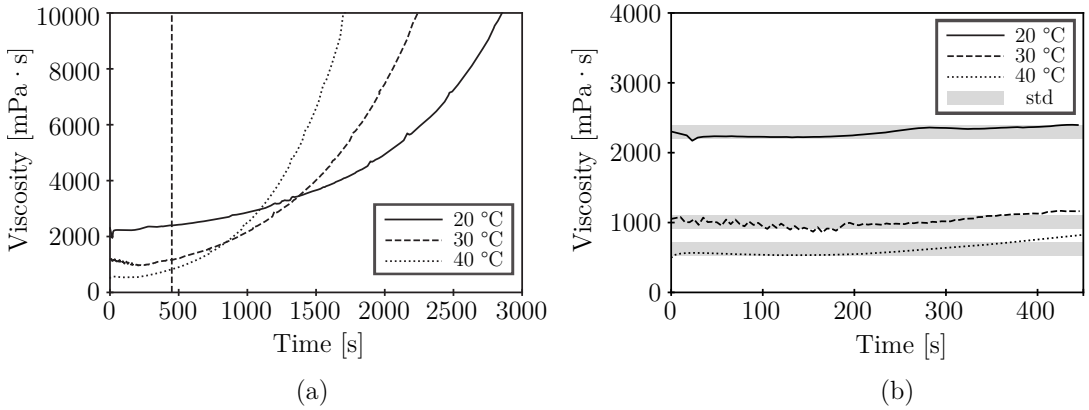

Figure 4.9: Resin viscosity for 20 °C, 30 °C, and 40 °C in 3000 seconds, and b) in 450 seconds.

The surface tension measurements showed no variation over time and a value of 56.92 ± 6.03 N/mm was obtained (Figure 4.10).

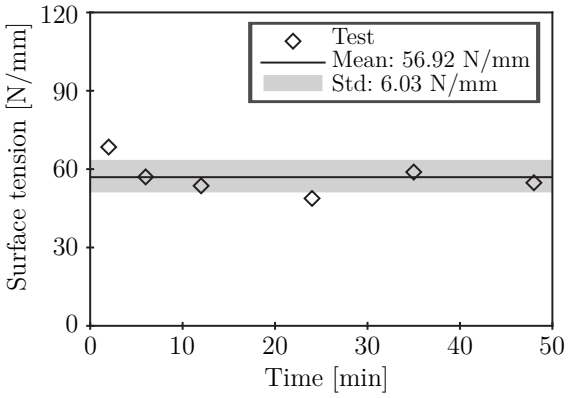

Figure 4.10: Surface tension evolution over time.

For the calculation of the contact angle, rendered XCT volumes were scanned and nine fibre-resin menisci were obtained (Figure 4.11). An image-processing algorithm developed in Python® was used to calculate the contact angle, which resulted in a value of 47.80 ± 3.52 °C.

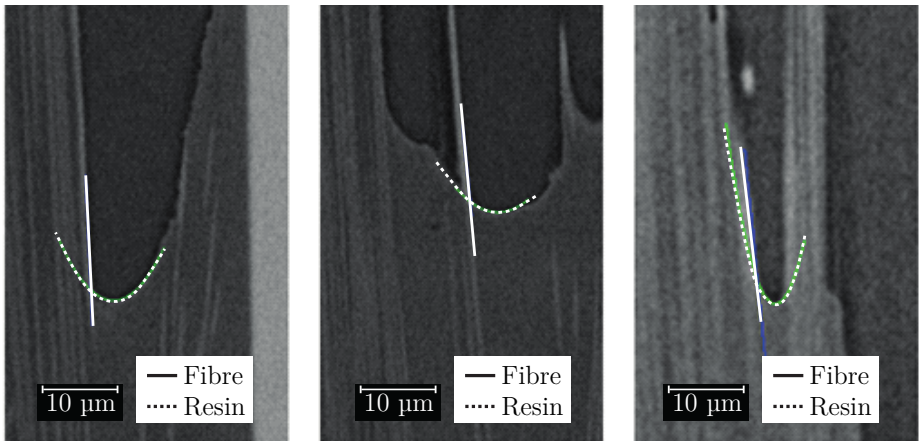

Figure 4.11: Calculation of the contact angle using images from XCT.

Finally, plates were produced at different injection flow-rates, and by means of the Ca^* equation (Equation 4.5) it was possible to related the void levels and Ca^* numbers (Figure 4.12). The high reactivity of the resin did not allow a value of Ca^* of less than 0.02, since a reduction of the injection velocity or viscosity (by increasing temperature) resulted in premature curing without total impregnation of the part. In addition, it was not possible to produce plates with a Ca^* higher than 0.14, as increasing the viscosity or the injection velocity resulted in excessive internal pressure giving rise to textile deformation (washout) [Bodaghi 2019c]. It can be seen that between Ca^*=0.02 and Ca^*=0.14 it can be seen that there is a range around Ca^*=0.09 where the void content is the minimum but not less than 1%.

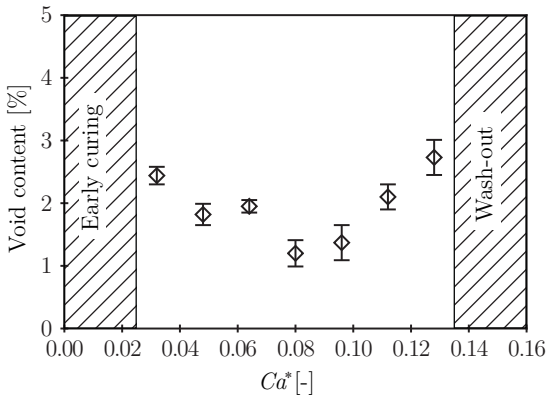

Figure 4.12: Void content for different Ca^* within processability limits.

To obtain plates with a void content of less than 1%, plates with Ca^*_{opt} were manufactured, and vacuum was applied at the mould outlet. On the other hand, to

manufacture plates with a void content higher than 4%, WCM was used. The results of the physical properties of fibre content, matrix and voids of the four types of fabricated plates are shown in table 4.3. It can be observed that the plates manufactured with RTM and following the criteria of Ca^*_{opt} ($\text{VARTM}_{\text{opt}}$) where vacuum was also applied, resulted in a void content lower than 1% (0.58 ± 0.18%). This result was in good agreement with the previous findings of Lebel *et al.* [Lebel 2017], who achieved plates with void content lower than 1% by searching for the optimum capillary number. In the case of the plates with the Ca^*_{opt}, but without vacuum (RTM_{opt}), the void content was 1.35 ± 0.28%. When RTM with non-optimal conditions was used, the void content obtained was 2.44 ± 0.14%. Plates manufactured with WCM showed a higher level of voids, even exceeding 4% (4.34 ± 0.31%). Lee *et al.* [S. Lee 2021] obtained similar void content (4.9%) for CF-Epoxy NCF manufactured with WCM. Figure 4.13 shows in detail the qualitative difference in void content between the $\text{VARTM}_{\text{opt}}$ and WCM samples.

Table 4.3: Void content and fibre volume for the four types of plates.

	Fibre volume [%]	Void content [%]	Nomenclature
$\text{VARTM}_{\text{opt}}$	46.18 ± 0.91	0.58 ± 0.18	$V_{0.6\%}$
RTM_{opt}	46.53 ± 0.92	1.35 ± 0.28	$V_{1.4\%}$
RTM	45.85 ± 0.80	2.44 ± 0.14	$V_{2.4\%}$
WCM	46.27 ± 1.36	4.34 ± 0.31	$V_{4.3\%}$

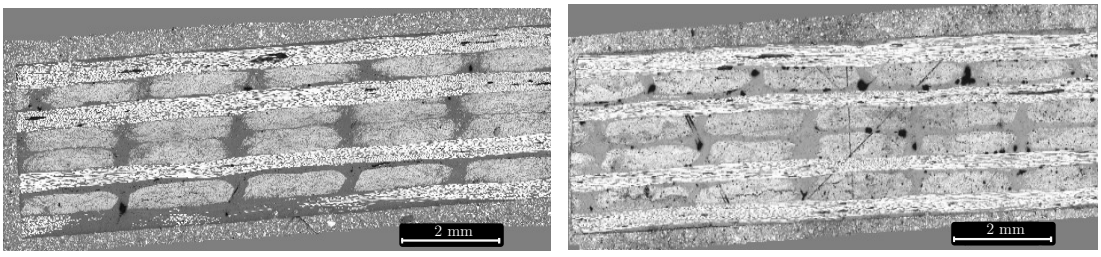

a) b)

Figure 4.13: Microscope images for the detection of voids for a) $\text{VARTM}_{\text{opt}}$ and b) WCM.

4.4 Drop weight impact test

4.4.1 Single impact

For the classification of the energy regimes, the damage threshold (delamination threshold) was first determined by 70 J impacts (Figure 4.14). The delamination energy, E_{d}, at which the damage initiated, was identified by the force F_{d} which caused a reduction in stiffness [Feraboli 2006; Zabala 2014].

Impact energies below E_d were labelled as subcritical impacts, and those above E_d as supercritical impacts. The E_d was very similar for all void contents, and had a value of 1.5 J ± 0.2 J. The peak force F_p, gives information on the onset of fibre breakage, and the energy threshold of fibre fracture E_{ff}, could be determined being 19.8 J ± 0.3 J, very similar for all four types of plates. Thus, supercritical impacts were classified into supercritical inducing delamination (Supercritical I: 1.5-19.8 J) and supercritical inducing fibre failure (Supercritical II: > 19.8 J).

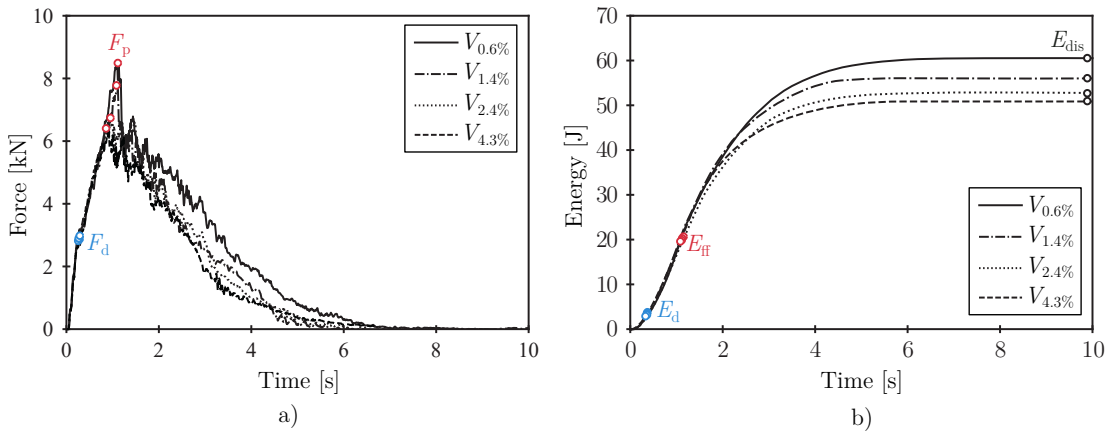

Figure 4.14: Evolution of a) force and b) energy over time for 70 J supercritical impacts.

In the fractographic analysis carried out (Figure 4.15), it was observed that impacts induce breaks of different types: After overcoming E_d, delamination begins to occur between the layers and breakage of the matrix. Once E_{ff} is exceeded, the fibre starts to break near the impact zone.

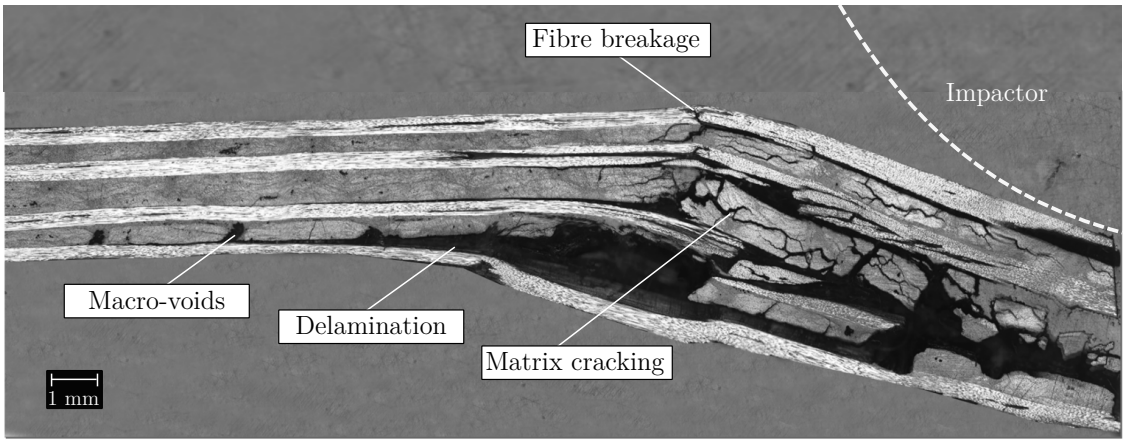

Figure 4.15: Different failure mechanism in supercritical II (70 J) impacts.

The F_p and the dissipated energy E_{dis} was different for each of the plates. Figure 4.16 shows the F_p (Figure 4.16a) and E_{dis} (Figure 4.16b) obtained for the four types of fabricated plates. The reduction of both properties can be observed for an increase in

void volume. The F_p was reduced by as much as 25.9% for void contents between 4-5% frequently obtained in WCM ($V_{4.3\%}$). On the other hand, in the case of energy dissipation, the plates with high void content ($V_{4.3\%}$) dissipated 9.57% less energy.

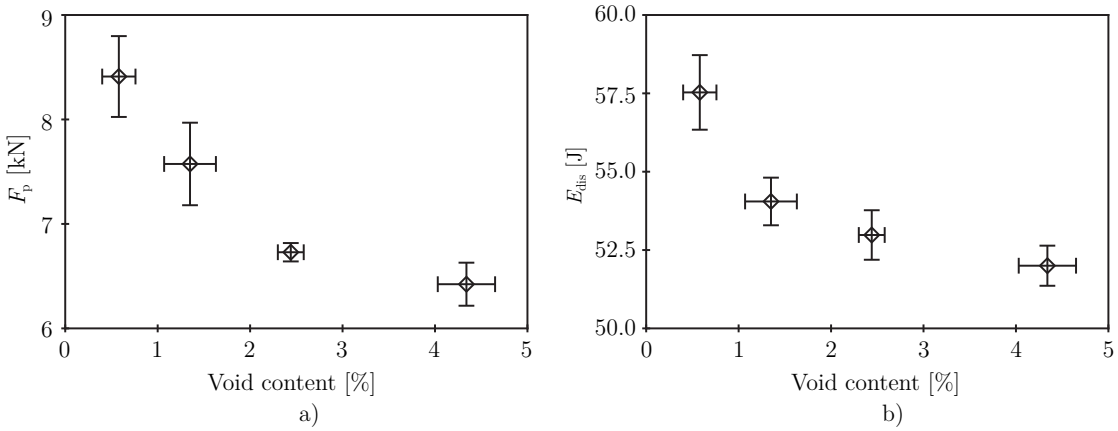

Figure 4.16: Reduction of a) the peak force, F_p, and b) the dissipated energy, E_{dis}.

For clarity, in the subsequent analysis only the values of the two extremes of void content are shown, i.e., $V_{0.6\%}$ and $V_{4.3\%}$. The samples were subjected to several single impacts from which the F_p recorded in each of the tests was extracted. Figure 4.17 shows the same F_p for the samples with low void content ($V_{0.6\%}$) versus the samples with high void content ($V_{4.3\%}$). The results obtained with samples $V_{2.4\%}$ and $V_{3.4\%}$ have been omitted for clarity. It can be seen that both samples followed the same trend, however the values for the high void content ($V_{4.3\%}$) samples were slightly lower. The graph shows how below E_{ff} the maximum force increases with the impact energy. Furthermore, it can be seen how the $V_{0.6\%}$ values are slightly higher than $V_{4.3\%}$. At E_{ff} (which is similar for both samples), the F_p reaches a plateau at 8,411 ± 387 N and 6,423 ± 206 N for low ($V_{0.6\%}$) and high void content ($V_{4.3\%}$), respectively.

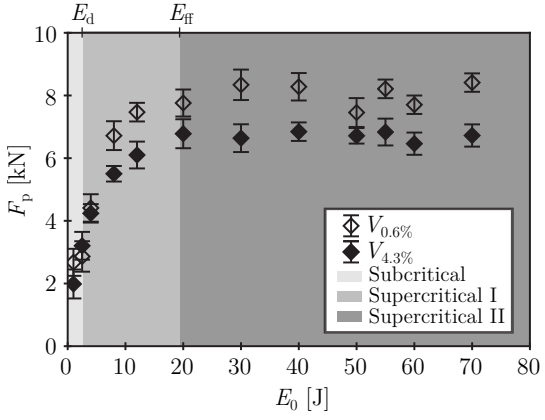

Figure 4.17: Peak force, F_p, versus impact energy, E_0, for low and high void content.

Figure 4.18 plots the evolution of the dissipated energy E_{dis} versus the impact energy E_0. The dashed line represents the limit where E_{dis} is equal to E_0, which is physically impossible to exceed. Above 50-55 J, perforation threshold, the specimen is perforated and the dissipated energy remains constant. However, the maximum dissipated energy is lower for $V_{4.3\%}$, 51.5 ± 1.3 J compared to 56.1 ± 1.1 J for $V_{0.6\%}$.

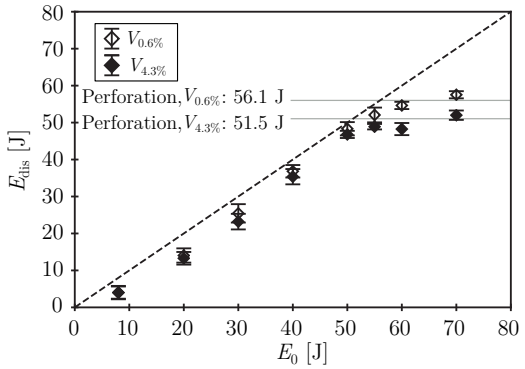

Figure 4.18: Dissipated energy E_{dis} versus impact energy E_0, for low and high void content.

The recorded force-time curves for subcritical impacts (1 J) revealed a different behaviour for the low and high void content samples (Figure 4.19). Firstly, the contact time between the impactor and the specimen was slightly different: A contact time of 2.54 ± 0.06 ms and 3.08 ms ± 0.11 ms was recorded for the low and high void content plates, respectively. This represents a 20% increase in contact time of high void content samples, $V_{4.3\%}$. In the same way, at low void contents, $V_{0.6\%}$, the peak force was 35% higher: 2,676 ± 452 N to 1,985 ± 219 N. In both cases, the asymmetric curve is a clear example of energy loss even at subcritical energies [Aurrekoetxea 2012].

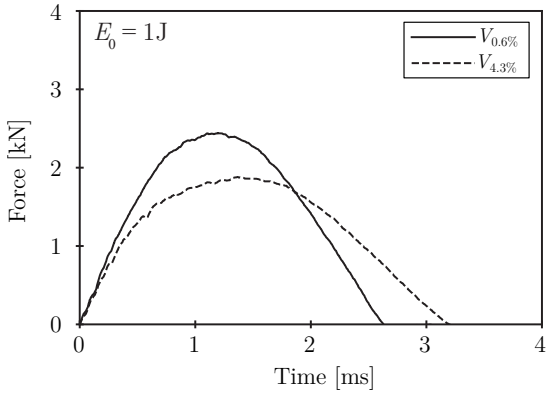

Figure 4.19: Force-time curve of subcritical impact (1 J) for low and high void content samples.

In order to quantify the difference in bending stiffness, the force-displacement curve of both samples were analysed (Figure 4.20). The force increased linearly to a maximum

(load phase), and then returned to the origin (unload phase, not shown in the figure). The difference in slopes is associated with the difference in bending stiffness [Shah 2019], with 2100 N/mm and 1365 N/mm corresponding to the stiffness of the samples with low,$V_{0.6\%}$, and high void content, $V_{4.3\%}$, respectively. This represents a reduction in stiffness of 35% when comparing the low and high void content plates. Liu *et al.* [L. Liu 2006] obtained similar results, showing a stiffness reduction of 7% for every 1% increase in void content, which would be 28% for 4% void content.

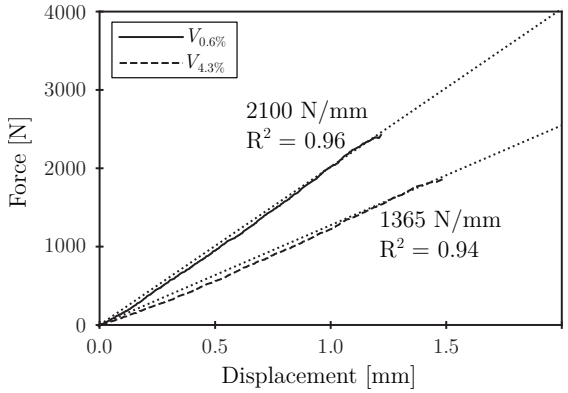

Figure 4.20: Force-displacement curve of subcritical impact (1 J) of low and high void content.

Energies higher than E_d (1.5 J) caused damage to the specimen. The specimens were analysed for supercritical I impact, where delamination and matrix failure ($E_0 > E_\mathrm{d}$) exists but without reaching fibre failure, ($E_0 < E_\mathrm{ff}$). The Figure 4.21 shows an impact of 8 J for both specimens at different void levels. It can be seen that in both cases the onset of delamination occurs above 2 kN, being slightly lower in the case of $V_{4.3\%}$. After this delamination, the loss of stiffness in the case of $V_{4.3\%}$ is greater, thus indicating that there was greater matrix failure. This caused the peak force F_p to be lower.

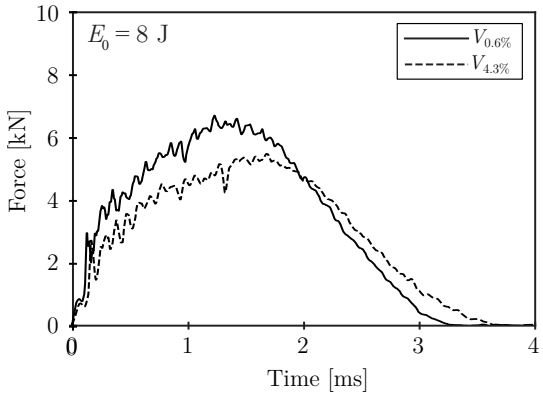

Figure 4.21: Force-time curve of supercritical impact (8 J) for low and high void content.

Figure 4.22 shows the $F(t)$ plot of a 20 J impact on the high, $V_{4.3\%}$, and low void content specimens, $V_{0.6\%}$. It can be seen that the onset of damage occurs around 2000-2500 N, being slightly lower in $V_{4.3\%}$ case, and a reduction in the slope occurs. However, after the onset of damage, the propagation is more severe in the case of the high void content specimens, $V_{4.3\%}$. Several papers in the literature have shown how void content has a detrimental effect on interlaminar shear strength [S. Sisodia 2015; Varna 1995] and out-of-plane intralaminar shear strength [S. Sisodia 2015; Carraro 2015a] for carbon/epoxy NCF laminates manufactured with RTM. Furthermore, Hou *et al.* [Hou 1996] demonstrated that the fracture toughness of mode II crack propagation decreases with increasing void content.

This causes fibre breakage to start at a lower energy for a higher void content, thus reaching a lower peak force. In the case of the low void content plate $V_{0.6\%}$, the peak force is around 7500 N. On the other hand, in the case of the high void content plate ($V_{4.3\%}$), the F_{p} was lower, 6700 N.

In conclusion, both the E_{d} and F_{p} were lower at higher void contents. It is worth mentioning that the E_{d} detected in the 8 J and 20 J impacts was the same as that previously detected in the 70 J impacts, as it is independent of the incident energy [Cartié 2002].

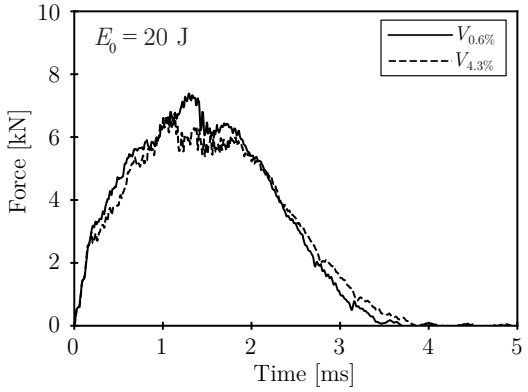

Figure 4.22: Force-time curve of supercritical impact (20 J) for low and high void content.

4.4.2 Damage tolerance

The effect of impact energy on residual properties was studied by means of the three-test characterisation method. Figure 4.23 shows the residual stiffness, which was calculated as the ratio of contact time in subcritical impacts, before and after damaging the specimen. For both cases, the stiffness was reduced up to 50% with impacts of 20 J.

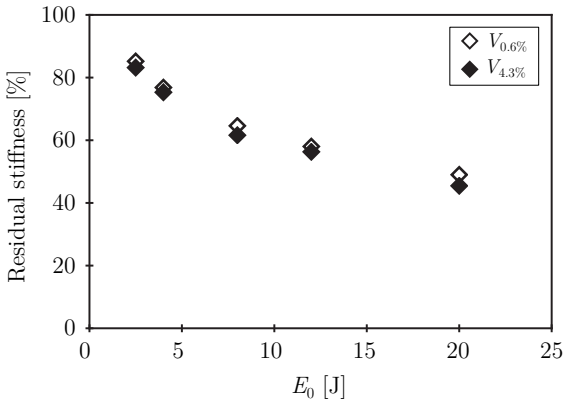

Figure 4.23: Residual stiffness evolution curve for low and high void content.

In the 20 J impacts, a slight decrease in the residual stiffness of $V_{4.3\%}$ versus $V_{0.6\%}$ could be appreciated, being 45.8% and 49.1% residual stiffness respectively. The effect of voids is less noticeable in residual properties than in single impact properties. This may be because once the part is delaminated, the effect of delamination is more pronounced than the effect of void content.

This loss of stiffness is mainly due to the delamination generated in the part. Delamination is one of the main failure modes of fiber-reinforced composites out-of-plane impacts events. It occurs in areas of high interlaminar stress where interlaminar crack initiation and propagation can occur. High interlaminar stress zones usually appear at singular points in the laminate, such as free-edges, internal ply drops and voids [Turon 2018]. These defects are stress concentrators and usually show the highest interlaminar stresses.

To validate this effect, both samples were analysed by C-scan ultrasonic inspection. Figure 4.24 shows the delaminated area of both specimens. In both cases a circle of 40 mm diameter is shown, this was the free clamping area of the 60 mm specimens clamped by means of a ring fixture.

In both cases the shape is a somewhat irregular circle around the impact area. However, in the case of WCM (Figure 4.24b) the geometry is somewhat more irregular and at first glance the area is larger. The delaminated areas were quantified by means of a code developed in Python, giving as a result a 16% larger delaminated area in the WCM specimen. It is confirmed, therefore, that the specimen with higher void content suffered higher delamination and therefore the residual stiffness was lower. An increase in defects of this type can result in a reduction of properties and can lead to catastrophic failure in apparently undamaged structures [David-West 2008].

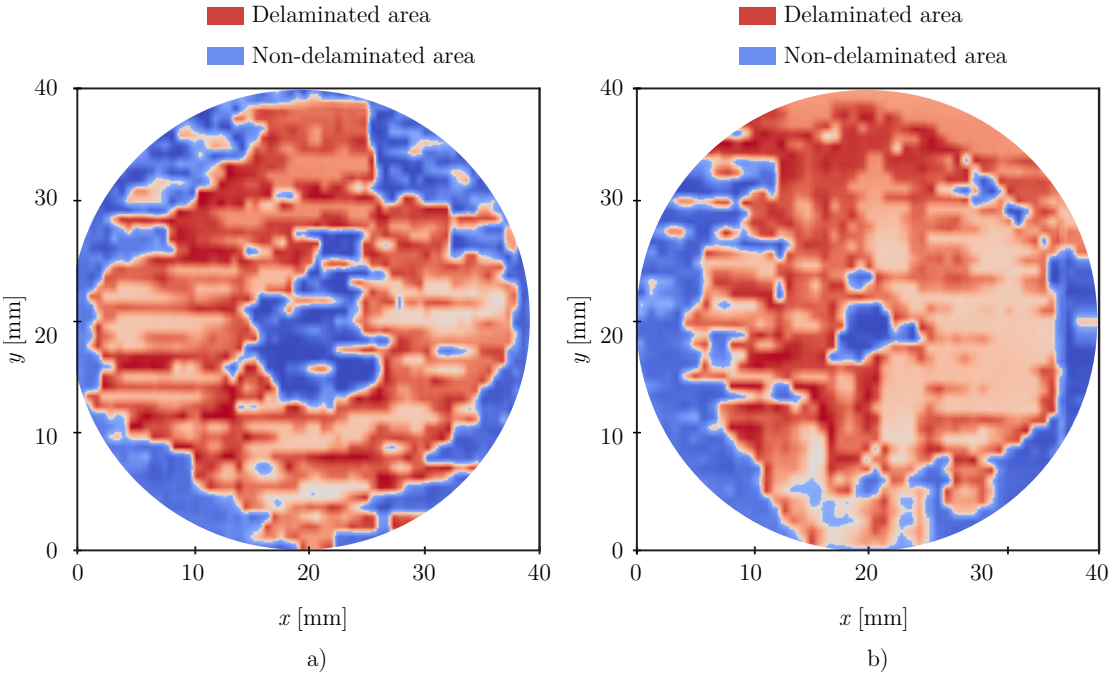

Figure 4.24: Delaminated area of a) low void content, $V_{0.6\%}$, and b) high void content, $V_{4.3\%}$.

4.5 Conclusions

In the present chapter, different RTM variants were compared, and their effect on void generation and subsequent impact properties was experimentally quantified. The WCM process and three variants of RTM were analysed, in which the effect of different injection parameters (application of vacuum and velocity control by capillary number) on void generation was analysed. To obtain the optimum capillary number, the viscosity and surface tension of the resin, and the contact angle between the resin and the fibre were characterised. The process that generated the lowest void content was the VARTM process optimised by capillary number (0.58 ± 0.18%). The RTM process without vacuum application and with velocity control by capillary number generated plates with 1.35 ± 0.28% void content. As regards the third RTM variant, the conventional RTM without vacuum application and velocity optimisation, the void content was 2.44 ± 0.14%. Finally, the WCM process generated the highest void content (4.34 ± 0.31%) as compared to the RTM variants.

Regarding impact properties, the increase of void content caused a reduction of 25.9% in the peak force, F_{p}, and 9.57% in dissipated energy, E_{dis}. The damage threshold for the different void contents was similar (1.5 J). The perforation and penetration limit was lower in the high void content ($V_{4.3\%}$) plates; 20% and 30% lower, respectively. In terms of bending stiffness, the low void content plates presented a higher stiffness of 2100 N/mm

compared to 1365 N/mm for the high void content plates. Interestingly, the post-impact residual properties were slightly affected by increasing the void content. At high and low voids levels, after an impact of 20 J the specimen retained 45.8% and 49.1% of the stiffness, respectively. The effect of void content is less pronounced on residual properties than on the first impact properties. This may be because once damage is generated in the specimen, the effect of the damage itself is greater than that of the voids.

From the results obtained in this research it can be concluded that manufacturing parameters in RTM processes have non-negligible effects on void generation and thus on the impact properties of the composite. Furthermore, it is shown that the optimisation of the flow front based on the optimum capillary number combined with the application of vacuum, can lead to the lowest void content (lower than 1%), and hence better impact properties.

In this way, the first operational objective of this thesis was fulfilled and the Process-Structure-Property link of the RTM process has been analysed experimentally.

5

Impregnation quality diagnosis by machine learning

Contents

5.1 Introduction

Since manufacturing defects induced at the impregnation stage reduce mechanical properties, the industry has adopted severe acceptance criteria with 1-2% as the threshold of acceptance, resulting in costly rework or scrappage [Hamidi 2018]. RTM process is complex and sensitive, as local permeability variations caused by multi-scale geometrical heterogeneities of the preform induce impregnation defects such as dry zones and voids [Bodaghi 2019c]. This level of sensitivity requires smart manufacturing systems that can modify the process in order to achieve zero-defect manufacturing or minimise rejected parts [Wuest 2014]. To achieve this, the production system must collect sufficient information from the process and be able to detect irregularities in-line. In other terms, it must build a Digital Twin of the physical process which accurately recreates the RTM process.

For digital modeling, numerical simulation technology is widely used in RTM, since flow, cure and mechanical models optimize the manufacturing process [Sozer 2012]. Furthermore, they are based on generalised boundary conditions that do not take into consideration the fluctuations of the preform permeability of each part. It is therefore necessary to know the real status of the process through process monitoring. Several data acquisition systems are used for RTM, but pressure sensors are particularly advantageous [Di Fratta 2013]. It is possible to associate pressure values measured at discrete points with resin flow-front position at any time [Di Fratta 2016]. The pressure evolution in the resin during the filling stage can be related to the void formation [Gourichon 2008], but in order to detect hidden patterns data-based modelling are needed. Data Analysis, such as Machine Learning (ML), has demonstrated to be well aligned with the ZDM philosophy [Wang 2013] and they can operate with high-dimensional multi-variate data to extract implicit patterns from dynamic and large-scale data sets [Wuest 2016]. This enables future predictions and data-driven decisions to be made. There are different ML approaches: Supervised Learning, Unsupervised Learning, Semi-Supervised Learning and Reinforcement Learning. In manufacturing processes, there is a huge amount of data, but their interdependencies are complex and patterns are not obvious. For this reason, Supervised Learning (SL) is the most widely used ML technique in the industry [Lu 1990; Wuest 2016].

This chapter presents a methodological approach for the generation and validation of a predictive model based on supervised learning for the diagnosis of defects in RTM filling stage. From process monitoring the micro-structure of the part, voids and dry zones, was predicted (Process-Structure link).

First, 10,000 different permeability maps were created and classified as defective or non-defective parts. These simulation results were used as synthetic data for training and validating the predictive model. In this way, generating the Process-Structure link, the first part of the PSPP-based DT was created (Figure 5.1).

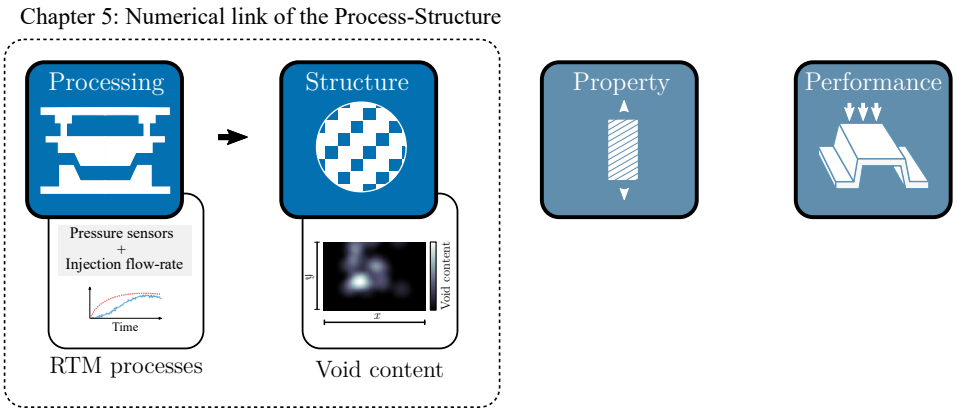

Figure 5.1: Numerical Process-Structure link.

5.2 FEM-based numerical model of the injection phase

A FE/CV based model was developed on the commercial software Pam-RTM® in order to simulate the impregnation stage of the RTM process.

Assuming that the flow is incompressible (i.e. the density is constant) the mass conservation equation (also known as continuity equation) is expressed as follows:

$$\nabla \cdot \vec{v} = 0 \tag{5.1}$$

and introducing Darcy's law into the continuity equation, the following is obtained:

$$\nabla \cdot (\frac{k}{\mu} \cdot \nabla P) = 0 \tag{5.2}$$

The following assumptions were made for the impregnation simulation: (I) The stiffness of the mould was considered infinite. (II) The preform thickness and permeability were constant. (III) Race-Tracking effect (inhomogeneity in flow due to the higher permeability between the mould and the fabric) was not considered. (IV) The resin was incompressible. That means, that the density of both resin and the fibre was considered constant, ρ_r and ρ_f, respectively. (V) The pressure generated inside the cavity does not deform the preform, i.e. the permeability is not modified for this phenomena [Advani 2010].

5.2.1 Materials properties

The fibre used was a biaxial Non-Crimp Fabric (NCF) of 50k high resistance carbon fibre, reference HPT 610 C090 from SGL. The fibre orientation was 0/90 and surface density was 610 g/m^2. Permeability variation due to binder application was taken into account in the simulations. The in-plane permeability measurements for both, preform with and without binder, were carried out by means of a rectilinear and saturated injection at constant flow-rate [Sozer 2012]. The binder was an epoxy resin in powder state (Araldite LT 3366 BD). The applied binder amount was 15 g/m^2 per layer. Two different permeability values for each zone were defined [Baskaran 2018] (Table 5.1); one without binder (k_{ref}) and a higher permeability with binder (k_{binder}), which is justified by the creation of new flow channels by the binder [Dickert 2012].

Table 5.1: Permeability values with and without binder [Baskaran 2018].

	k_{ref}	k_{binder}
Reference	HPT 610 C090	HPT 610 C090 + 15 g/m^2 binder
k_{xx} [m^2]	$4 \cdot 10^{-11}$	$8 \cdot 10^{-11}$
k_{yy} [m^2]	$5 \cdot 10^{-11}$	$9 \cdot 10^{-11}$

The resin used was a fast curing epoxy resin (XB 3585) and hardener (Aradur® 3475) supplied by Hunstman. The resin was injected at 100 °C and the rheological model used as input for the simulation was provided by the manufacturer's technical data sheet.

The Kamal-Sourour model [Kang 2001] was used to define the curing kinetics. The general equation for the resin with n components is as follows:

$$\alpha = \sum_{i=1}^{n} C_i \alpha_i \tag{5.3}$$

$$\frac{\mathrm{d}\alpha_i}{\mathrm{d}t} = K_i(T)\alpha_i^{m_i}(1-\alpha_i)^{P_i} \tag{5.4}$$

where $\frac{\mathrm{d}\alpha_i}{\mathrm{d}t}$ is the rate of reaction for component i in s-1, C_i is the amount of each reaction, α is the conversion at each instant and K_i is a variable defined by the Arrhenius law:

$$K_i = A_i \exp\left(\frac{-E_i}{\mathrm{R}T}\right) \tag{5.5}$$

where E_i is the activation energy, R is the universal gas constant, and T is the absolute temperature of the resin. The constants A_i, m_i and p_i were determined experimentally (Table 5.2) from differential scanning calorimetry tests [Keller 2015] (Figure 5.2a).

The viscosity of the resin depends on the temperature and the degree of conversion. Increasing the temperature decreases viscosity but accelerates the curing reaction, and viscosity increases with the degree of conversion. The most widely used model for determining viscosity as a function of temperature and viscosity as a function of temperature and degree of conversion is governed by the following equation [Advani 2010]:

$$\mu(T,\alpha) = A_\mu \exp\left(\frac{E_\mu}{\mathrm{R}T}\right) \tag{5.6}$$

where E_μ is the activation energy,

$$E_\mu = a + b\alpha \tag{5.7}$$

and the coefficient A_μ is defined:

$$A_\mu = a_0 \exp(-b_0\alpha) \tag{5.8}$$

where a, b, a_0 and b_0 are empirical constants of the material and they are shown in Table 5.2.

Table 5.2: Constant for the curing kinetics and rheology models [Keller 2015].

Curing kinetics costants		Rheology costants	
A_i	3.17	a	2797
E_i	83.70	b	9631
m_i	0.55	a_0	$1.2 \cdot 10^{-4}$
p_i	2.28	b_0	-0.35

The Figure 5.2b shows the evolution of the resin viscosity over time for different process temperatures taken from the material data-sheet.

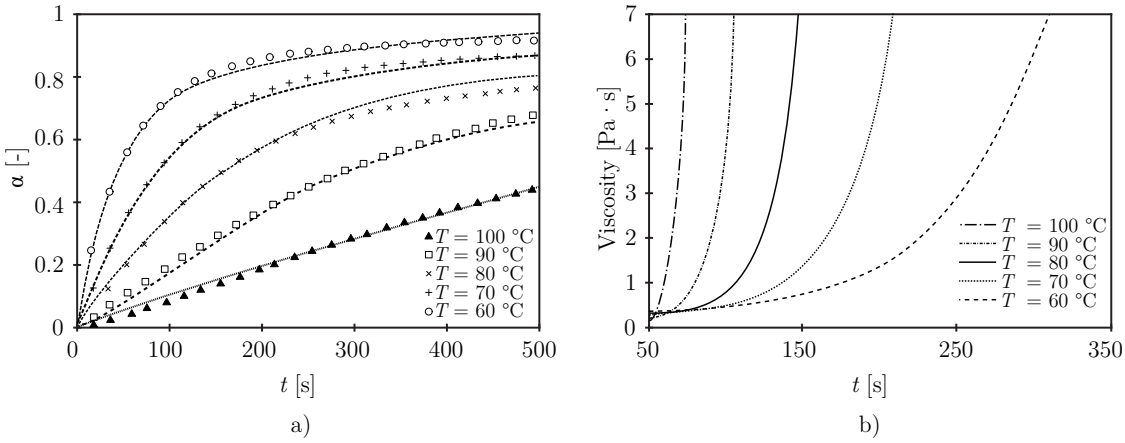

Figure 5.2: a) Degree of cure [Keller 2015], and b) Viscosity as a function of time and temperature.

5.2.2 Geometrical modelling and boundary conditions

The studied geometry was a 350 mm × 250 mm × 3 mm plate. The resin was injected from a central injection port, creating a radial flow pattern in the earliest stage. Furthermore, four vent ports were placed in the vertexes of the mould. The part was segmented into 32 zones in order to create different permeability scenarios (Figure 5.3). In addition, a virtual monitoring point was located in the middle of each zone to record pressure evolution during the injection stage.

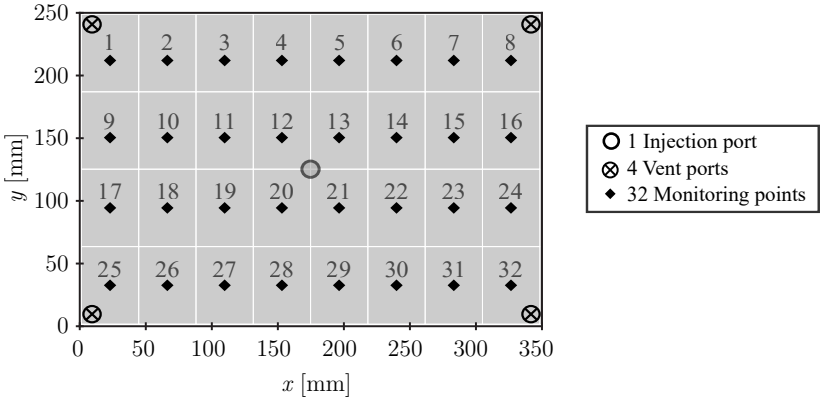

Figure 5.3: Rectangular plate segmented into 32 zones.

The mesh size has a strong influence on the numerical results, so a convergence study was carried out in order to balance the resolution and computational cost. This study showed that the result converged from 10,000 elements. The geometry was meshed with 4 mm size 12,288 triangular thin shell elements.

5.2.3 Impregnation velocity optimization

In Chapter 4, a full characterisation of the materials in terms of viscosity (μ), contact angle (θ) and surface tension (γ) was made. In addition, the Ca^*_{opt} that ensures the minimum void content was also identified (Values shown in Table 5.3).

Table 5.3: Impregnation properties values.

Property	Value
Contact angle, θ [°]	47.80
Surface tension, γ [N/mm]	56.92
Ca^*_{opt} [-]	0.09

The optimum impregnation velocity $v^{\text{opt}}_{\text{imp}}$, which ensures the minimum void content, can be calculated as follows:

$$v^{\text{opt}}_{\text{imp}} = \frac{ca^*_{\text{opt}}\gamma\cos\theta}{\mu} \tag{5.9}$$

and Ruiz *et al.* [Ruiz 2006], proposed a methodology in which they demonstrated how the Ca^*_{opt} based injection flow-rate control system allowed them to generate parts with a minimum void content. This flow control allowed to increase or decrease the injection flow rate at time step $k+1$ to ensure the capillary number close to its optimal value along the entire flow front. To do this, it is necessary to calculate the capillary number in all elements of the flow front in time step k ($\|\sum_{i=1}^{n} Ca^*_i\|$) and correct the flow rate in the time step $k+1$ ($Q_{\text{inj}\|k+1}$):

$$Q_{\text{inj}\|k+1} = \left(\frac{Ca^*_{\text{opt}}Q_{\text{inj,k}}}{\|\sum_{i=1}^{n} Ca^*_{i,k}\|}\right) \tag{5.10}$$

In all simulations performed in this chapter, this flow control strategy was used for the void content minimisation.

5.3 Machine learning-based predictive model for impregnation quality diagnosis

Once the impregnation model was generated, a predictive model based on supervised learning was developed to classify the quality of the voids and the unfilled zones of a RTM composite parts. For this purpose, the guidelines of The Cross Industry Standard Process for Data Mining (CRISP-DM) approach [Wirth 2000] were followed. The CRISP-DM methodology determines that between the definition of the problem and its final deployment, four phases must be followed (Figure 5.4): Data acquisition, data pre-processing, model training, and model evaluation.

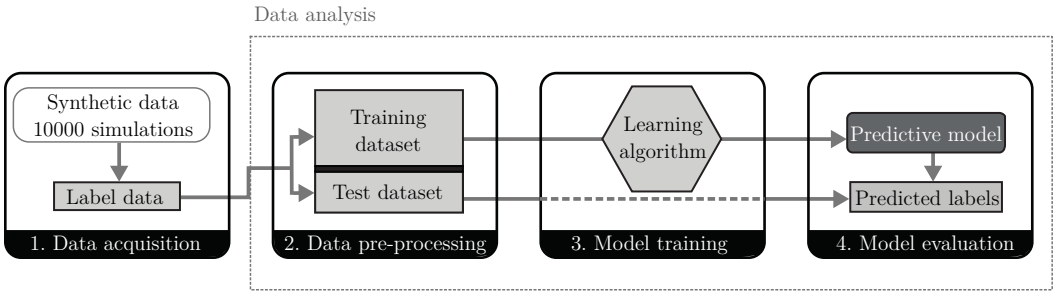

Figure 5.4: Cross Industry Standard Process for Data Mining.

In the data acquisition phase, synthetic data was gathered using the numerical simulation method of the RTM process. The objective of this phase was to generate different scenarios of the RTM process by introducing local permeability variation that generated different quality outputs (voids and unfilled zones). The part to be manufactured was a rectangle segmented in 32 zone, but the four corner zones (vent ports location) were not considered in the quality analysis. Each zone was assigned a permeability from two possible values (with and without binder, K_{bin} and K_{ref}, respectively). The resulting 28 zones and 2 possible permeability values for each zone give 268,435,455 possible combinations. Within all these possible combinations, they were classified into groups according to the number of zones with K_{bin} permeability (n-group). That is, "3-group" had 3 zones with K_{bin} permeability and the 25 with K_{ref} permeability. To limit the cases, a maximum of 400 simulations were randomly selected from each n-group. This gives a total of 10,014 cases, but considering that 14 were discarded, 10,000 simulations were performed.

In each of the simulations, injection flow-rate and the pressure time series at the central point from the 28 zones were recorded. Each simulation was labelled as good/defective quality according to the void content and filling factor criteria. A part was considered defective if it had, at least, one zone with a void content higher than 1% or a filling factor lower than 99.5%.

Then, in the pre-processing phase, flow-rate and pressure time series were processed and structured to obtain their descriptive features by analysing them in the time, frequency and Hilbert domains. Once the data was structured, it was split into training dataset and testing dataset, the 80% and the 20% of the data respectively.

In supervised learning, model training is defined as the phase in which the machine learning algorithm builds a predictive model that relates the input features with target variable (good/defective). In this way, the model is able to predict the label when fed with new input features. In order to optimize the algorithm selection phase, AutoML was used to find the most suitable algorithm and its hyper-parameters [Weng 2019]. Finally, the built predictive model was evaluated using flow-rate and pressure time series features from testing dataset.

5.3.1 Data acquisition

As previously mentioned, 10,000 simulations (6 minutes each one) were carried out, with different permeability scenarios. Python scripting was used for generating inputs for each scenario, launching it and acquiring the output data in an automated way. The acquired output data were the pressure evolution in the middle point of each zone, flow rate evolution, void content of each zone and filling factor of each zone. The corner zones (Z1, Z8, Z25 and Z32) were excluded in order to avoid irregularities at the vent port.

Among the 10,000 simulations performed, 5,041 were labelled as good quality and 4,959 as defective quality. Among the defective quality simulations, 1,582 have at least 1 zone with more than 1% of void content, 1,959 have dry zones and 1,418 have both defects. This results on a correctly balanced dataset (almost 1:1 ratio). Although unbalanced datasets can be used, it is preferable to use balanced data in classification problems. This is because the majority of machine learning algorithms used for classification, were developed based on the hypothesis that each class has equal number of samples. Consequently, the predictive model may be biased and ignore the minority class [Raschka 2019]. Three representative results were analysed. One without any defects (S_I), another with void content higher than 1% (S_{II}), and the last with dry zone (S_{III}) (Figure 5.5).

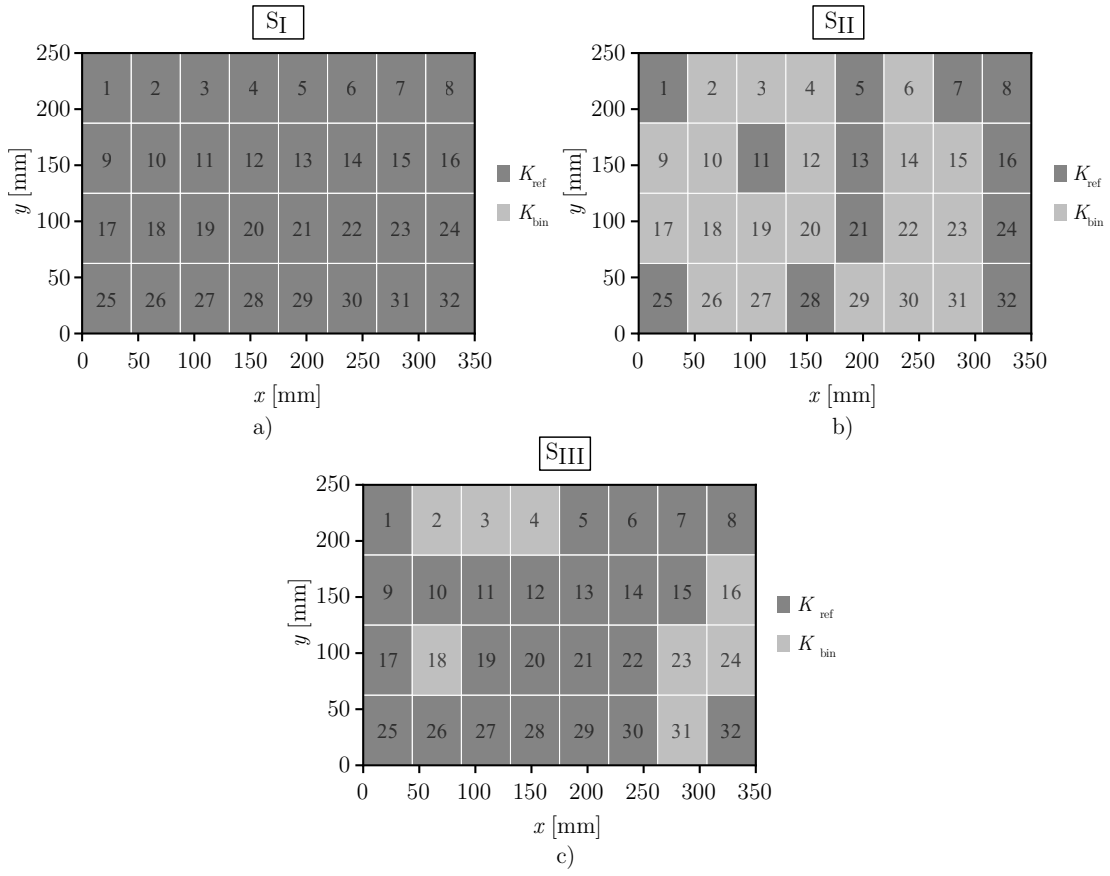

Figure 5.5: Case studies: no defects (S_I), void content higher than 1% (S_{II}) and dry zone (S_{III}).

Flow-rate

The velocity optimizer module modified the injection parameters in order to assure the optimum capillary number, and consequently it kept the flow-front velocity at its optimum value. Two stages can be detected by analysing the flow profile for the S_I, S_{II} and S_{III} simulations (Figure 5.6). The first stage went from the beginning of the simulation to about 50% of the filling. It described the radial flow pattern of the resin before touching the nearest mould walls. If the viscosity would be constant, the flow rate increase would be linear since the perimeter of the flow-front would increase linearly. However, as the viscosity of the resin increased over time, the flow-front velocity decreased over time in order to assure the optimum capillary number. As the optimum flow-front velocity decreased over time, the rate of change of the flow-rate also did. In the second stage, from the moment the resin touched the wall until the complete impregnation of the mould, the flow-front area remained constant. In the same way, as the resin viscosity increased, the optimum flow-front velocity and thus the flow rate decreased. These results confirmed that to ensure the minimum void content, a variable injection was necessary [Ruiz 2006]. Furthermore, this variable injection was not always be the same for the identical geometry.

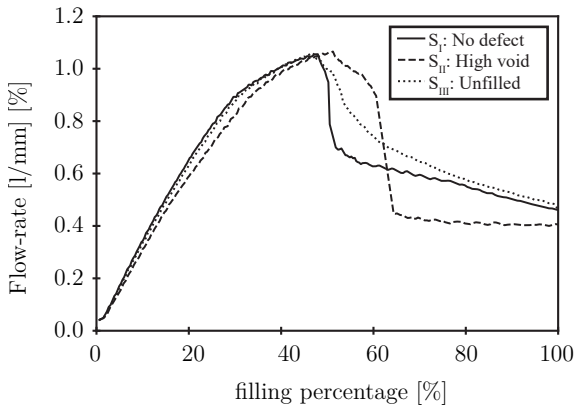

Figure 5.6: Evolution of the Flow-rate with the filling percentage.

Dry zone defect

Figure 5.7 shows the evolution of filling pattern of both S_I and S_{III} at 20%, 60% and 95% of the filling. At 20% of filling, both simulation followed the same pattern. Once the flow-front arrived to the closer wall, the higher local permeability in second, third and fourth zones of the S_{III}, allowed a faster flow-front as can be seen when filling is at 60%. Consequently, at 90% of filling, the fastest flow-front arrived to the vent port before total filling of the cavity and a dry zone was generated (Region-A).

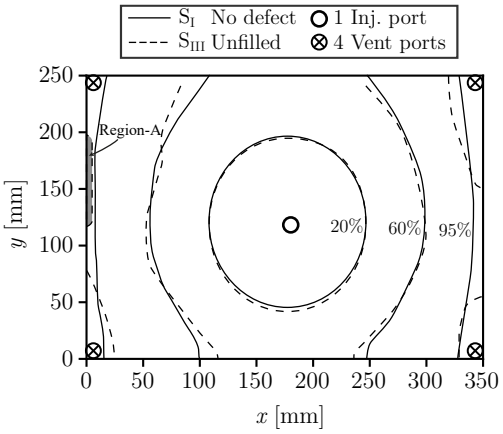

Figure 5.7: The evolution of filling pattern of S_I and S_{III} simulations.

Void content defect

The simulations S_I and S_{II} were compared in terms of void content. As it can be seen in Figure 5.8a the void content was homogeneous and generally lower than 0.5%, fulfilling the quality criteria of 1% void content in all zones. Nevertheless, in Figure 5.8b a higher void content can be visualized, where a high void content band (>1.5%) stands out. The location of the band, coincide with the boundary of K_{ref} and K_{bin} zones seen in the permeability map approximately at $x = 300$ mm. It can be observed how a local variation of permeability can induce an increase in void content. In this case, the permeability variation was due to the application of binder, however, textile heterogeneities, nesting effect or race-tracking [Mesogitis 2014] could also induce local permeability variations and therefore could compromise the quality of the part in the same way.

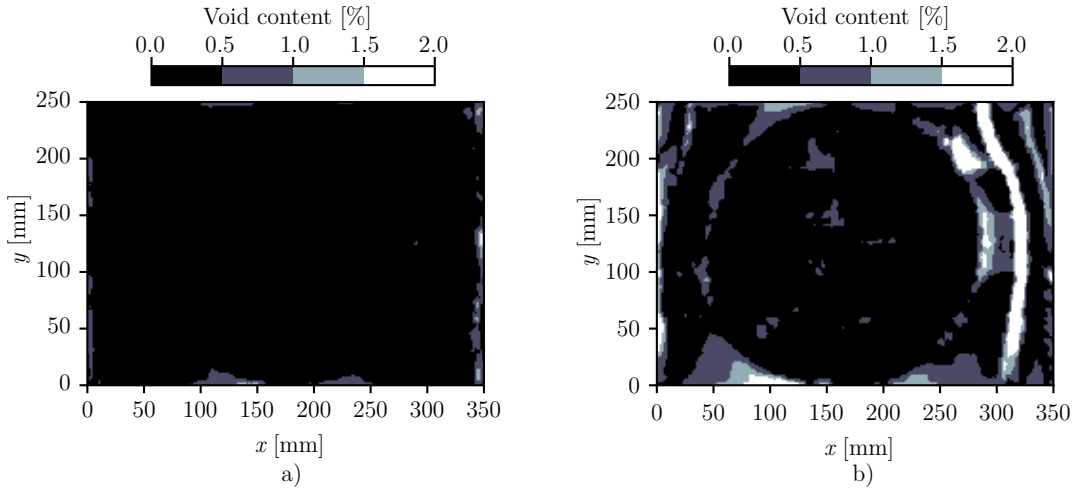

Figure 5.8: Final void content of a) S_I and b) S_{II}.

Pressure evolution

Unlike recording the pressure at the injection port, the monitoring points placed in the centre of the zones can give information about the arrival time of the flow-front, its evolution and thus deduce the homogeneity of filling. It was analysed the pressure evolution in zone 13 (one of the four zones of the injection point) for the tree cases (S_I, S_{II} and S_{III}) to understand its evolution for different permeability scenarios (Figure 5.9). Although zones 12, 20 and 21 were as close as zone 13, zone 13 was arbitrarily chosen to analyse the overall pattern. In all cases, once the resin reached the centre of the zone, the pressure started to increase until it reached a maximum value between 40% and 50% of the filling. This maximum coincided with the maximum injection flow rate shown in Figure 5.6 and occurred when the resin reached the closest wall of the mould. The slope of pressure evolution and the instant of the peak differed in S_{II}, which was due to a higher permeability (K_{bin}) in the zones around the injection port. Then, as the area of the flow-front was reduced, the flow-rate was reduced and thus the pressure inside the cavity. The pressure started to increase again until the injection was finished, when the resin arrived to one of the four vent ports.

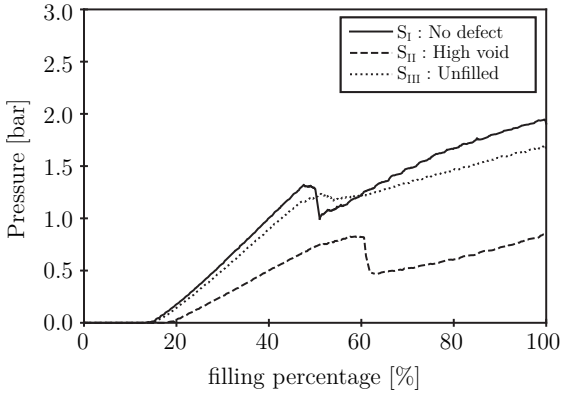

Figure 5.9: The evolution of the pressure of the analysed cases.

Each of the monitoring point recorded the arrival of the flow-front and its evolution after arrival. This information was key to identify the evolution of the flow inside the cavity and be able to determine if the part was filled correctly without defects. However, it was impossible to detect hidden patterns with the naked eye and it was necessary to apply to data analysis methods.

5.3.2 Data pre-processing

The 10,000 simulations were divided in two parts; 8,000 were used for training and 2,000 for testing. The time series from the simulations were pre-processed and the two-dimensional (time-dependent) time series were transformed into one-dimensional arrays

(time series features). In this way, an array containing the time series features and the quality label was obtained from each simulation. Feature extraction was performed on time series data, extracting relevant statistical features (Table 5.4). Time, frequency and Hilbert-frequency domains transformations were used for getting different points of view on the data. After each data transformation, numerous statistical features were extracted. For the development of the time series feature extractor, the tsfresh library was used as a reference, but due to disagreements in the design and implementation, a new library was developed.

Table 5.4: Statistical features extracted from filling time series.

Feature	Time	Frequency	Hilbert
Standard error mean	✓	✓	✓
Signal energy	✓	✓	✓
Maximum	✓	✓	✓
Minimum	✓	✓	✓
Skewness	✓	✓	✓
Kurtosis	✓	✓	✓
Standard deviation	✓	✓	✓
Variance	✓	✓	✓
Length	✓	✓	✓
Mean	✓	✓	✓
Median	✓	✓	✓
Mean second derivative	✓	-	-
Cid ce (complexity)	✓	-	-
Sample entropy	✓	-	-
Augmented dickey fuller	✓	-	-
C3	✓	-	-
Large standard deviation	✓	-	-
Percentile	✓	-	-
Time reversal asymmetry	✓	-	-

After the extraction 8,159 features, the correlation between pairs of variables was measured, as the feature extraction process can produce highly correlated features. These features were filtered in an effort to reduce noise and obtain a simpler representation of the fabrication process. The features with a correlation higher than 90% were removed, leaving 1,054 features for data analysis.

One of the main challenges of ML models is to find the right fit and avoid underfitting and overfitting effects. The underfitting effect occurs when the model is not complex enough to identify patterns and therefore does not achieve good results when making predictions with new data. On the other hand, overfitting occurs when the model fits too closely to the known data but is not able to obtain general patterns and the predictions with new data are not as accurate. In order to optimize performance, Recursive Feature Elimination (RFE) was applied using a Random Forest classifier, identifying the most

relevant features. RFE is a backward elimination technique, which consists of removing the least relevant features iteratively eliminated to find the optimal number of features [Raschka 2019]. The optimal number of features was determined to be 64 (Figure 5.10).

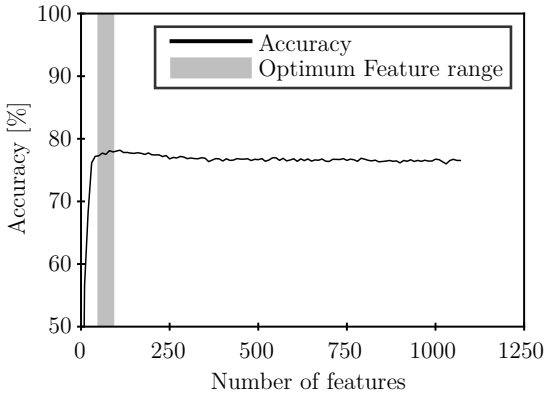

Figure 5.10: Recursive Feature Elimination (RFE) results.

5.3.3 Model training and evaluation

Model training method

Subsequently, the filtered data were used as input for the automatic model optimiser (Auto-ML), TPOT [R. S. Olson 2019] and Hyperopt [Bergstra 2011] library were used for this task. This approach simplified the data analysis process, as the phases where the most sensitive decisions taken were automated. Furthermore, as a consequence of using genetic programming, optimising multiple algorithms and doing hyper parameter combinations, the most efficient models were achieved. This optimization was performed setting an initial population of combinations of algorithms and hyper parameters, and through an iterative selection process called generations, only the most accurate pipelines were selected and evolved. When it comes to the selection process, the fitness of each pipeline was calculated on the accuracy of the 5-fold cross-validation technique of the estimator. This validation technique provides a clear indication of how well the model can generalize in a new dataset without overfitting. The final model was analysed for the purpose of gaining insight into the manufacturing process. The interpretation procedure was carried out focusing on the importance of each feature and the interrelations between them. Apart from the model suitability analysis, a feature importance and feature interrelation analysis were conducted. Finally, the obtained results were minutely analysed using the domain knowledge, in order to acquire new insight into the process.

Model training results

The pre-processed data feeds the AutoML, and pipeline determined that the most accurate model was Extreme Gradient Boosting (XGB) [T. Chen 2016]. Light Gradient Boosting Machine (LigthGBM) [Ke 2017], which also has a gradient boosting framework but is not included in TPOT, was included in the analysis showing also good results. The application of the AutoML system based on TPOT genetic programming shows that ML pipelines can be improved their effectiveness in supervised classification problems, even with low prior knowledge. This can be beneficial for processes, like RTM, where no experienced data science team is available. Analysing TPOT results, it was observed that the models with the greatest predictive capacity are the so-called Ensemble Methods Based on Decision Trees. These Ensemble algorithms combines multiple models (weak learners) to obtain a more robust predictive model reducing noise, bias and variance [Wuest 2016]. The way in which weak learners are combined varies, with Boosting and Bagging being two outstanding techniques. These methods, based on decision trees, overcome the artificial neural network (ANN) in classification problems when data come in structured rather than unstructured form (images, texts...). This explains the fact that it is better adapted to the RTM case study where featured and structured time series are available. It is observed that both XGB and LightGBM (Gradient-Boosting method) are more robust algorithms than Random Forest (Bagging method). This agrees with the literature, since Gradient-Boosting are commonly used in predictive modelling applied to failure diagnosis [M. Tang 2020]. Gradient-boosting methods can be better increasing accuracy and speed due to its parallel tree boosting capabilities, while bagging are better reducing overfitting.

Model evaluation method

Once the model was trained, it was ready for evaluation. The ML model made a good-defective prediction for each of the 2,000 test simulations, based on the time series features of each simulation. Each prediction was compared with the result obtained by FEM and it was determined how the prediction had been:

- **True Positive, TP**: the ML model predicted that the part was good and matched the FEM result (no defective areas).
- **True Negative, TN**: the ML model predicted that the part was defective and matched the FEM result (at least 1 defective zone)
- **False Positive, FP**: the ML model predicted that the part was good, but was wrong, as it did not match the FEM result (at least 1 defective zone)
- **False Negative, FN**: ML model predicted that the part was defective but was wrong, as it did not match the FEM result (no defective zones).

The performance of the model was measured by the confusion matrix and the Receiver Operating Characteristic (ROC) [Raschka 2019]. The confusion matrix is a square matrix that compares the real label (FEM results) with the predicted label (ML results). This matrix shows the general behaviour of the model by analysing the total number of True Positive (TP), True Negative (TN), False Positive (FP) and False Negative (FN). Accuracy parameter (ACC) provides general information about how many samples were correctly classified, and it is estimated as the sum of all correct predictions (TP+TN) divided by the number of total predictions [Raschka 2019]:

$$ACC = \frac{TP + TN}{FP + FN + TP + TN} \tag{5.11}$$

ROC curve compares models based on their performance, considering True Positive Rate (TPR) and False Positive Rate (FPR), for different decision thresholds [Bradley 1997]. To characterize the performance of each model, the Area Under the Curve (AUC) was used. The perfect model is the one with TPR of 1 and FPR of 0, which result in a value of AUC of 1 and a random guess, shows a linear ROC curve with a value of AUC of 0.5:

$$FPR = \frac{FP}{FP + TN} \tag{5.12}$$

$$TPR = \frac{TP}{FN + TP} \tag{5.13}$$

In data analysis, all the features were not equally relevant predicting the output. Feature importance measures how relevant a feature is in building the predictive model. More a feature is used, higher the relative importance. The relative importance was computed for each feature and all the features were compared between them.

Model evaluation results

As mentioned, Extreme Gradient Boosting (XGB) [T. Chen 2016] and Light Gradient Boosting Machine (LigthGBM) [Ke 2017] were selected as the most accurate models. Once the hyperparameters were optimized, both reached AUC values of 0.92 (Figure 5.11).

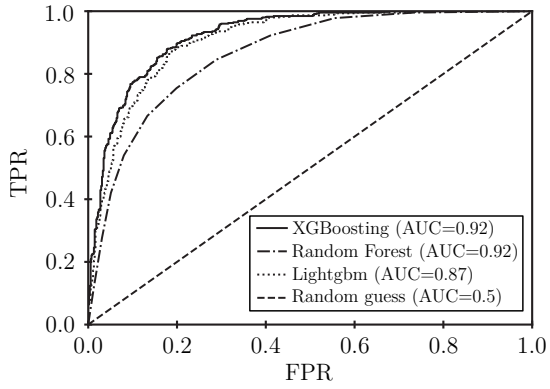

Figure 5.11: Receiver operating characteristic (ROC) curves.

The comparison of the optimized models showed that the XGB algorithm accuracy, 84.9% (Figure 5.12a), was slightly greater than the accuracy obtained by the LigthGBM model, 83.3% (Figure 5.12b), both of them above 2-sigma.

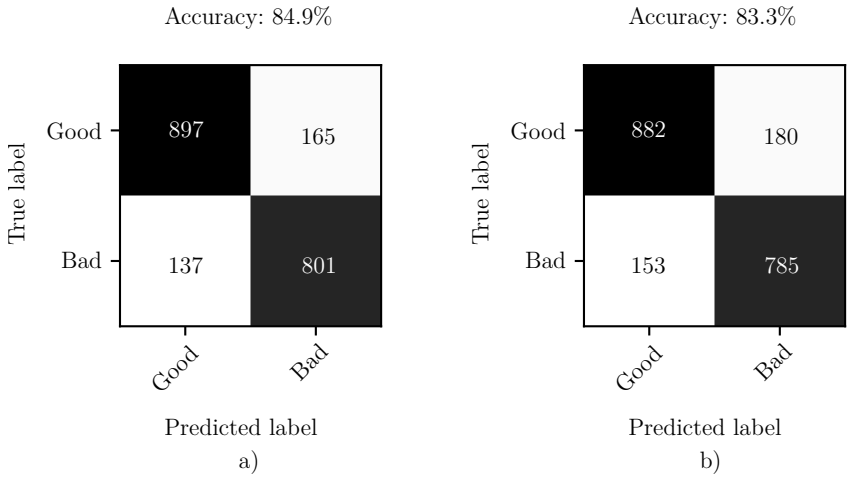

Figure 5.12: Confusion matrix for a) XGB and b) LigthGBM.

Once the behavior of the model was evaluated, the cases used for this evaluation were analyzed. It was observed that although the velocity optimization reduced the overall void content in all simulations, local defective zones were created. The ML model efectiveness detecting void zones was increased when the overall void content was high or there where several defective zones. When the defective zones were greater than or equal to 2, the succes rate was 98.84%, and when the overall void content was higher than 0.55% the succes rate was 100% (Figure 5.13a). On the other hand, analysing the parts with unfilled zones (Figure 5.13b), it can be seen that the error rate is less than 10% in both FN and FP. Moreover, over 1 unfilled zone no FP cases were found, being 100% the accuracy of

the model. This showed that the model was capable of rejecting the most deviated parts and it only failed when their quality was close to the quality threshold.

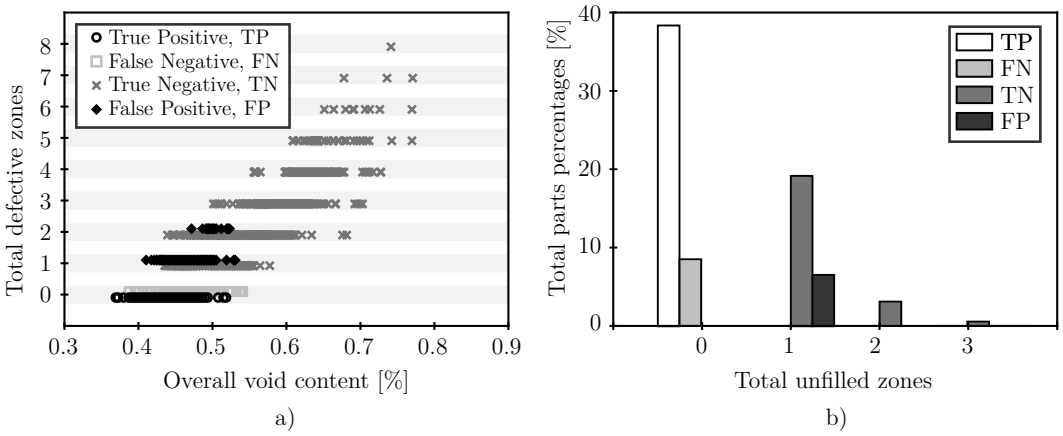

Figure 5.13: a) Void quality analysis, b) filling quality analysis.

All ML problems rely their prediction on data; the greater the volume of the data, the better accuracy was achieved. Figure 5.14 shows the accuracy in function of training datasets volume for XGB model. As can be observed, at 4,000 datasets the accuracy reached a plateau around 83%. Consequently, the 8,000 datasets used for training were considered enough for the modelling.

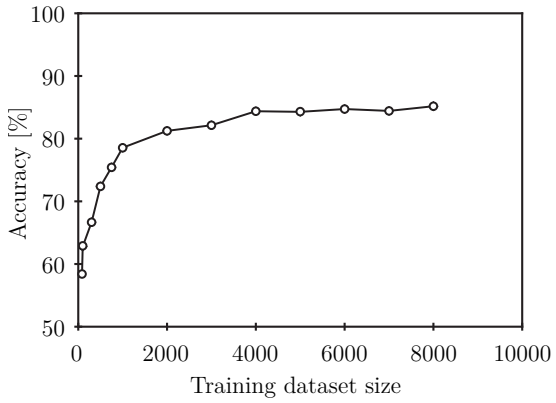

Figure 5.14: Effect of the trainning size on accuracy.

In an attempt to understand the process, a feature importance analysis was made, by computing and gathering them by zones (Figure 5.15). As can be seen, the zones 9, 16, 17 and 24, which were the last zones to be filled, had the highest importance when predicting the overall quality of the part.

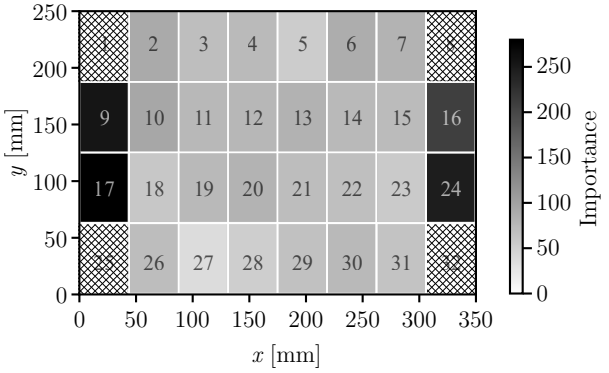

Figure 5.15: Importance of each zone for quality diagnosis.

In a process like RTM is not feasible to place too many sensor in the mould. Therefore, the objective should be to minimize the number of sensors without losing information about the process. For that reason, the reliability of the XGB and LigthGBM models was analysed by only feeding it with the features of the aforementioned four most important zones. The number of features was reduced to 15, showing that LightGBM results were better with an accuracy of 76.7% (Figure 5.16a) and an AUC of 0.87 (Figure 5.16b), which is still above 2-sigma like with 32 monitoring points. LightGBM has proven to be faster in training, using less memory and getting more accuracy and coincides with the results of studies that compare gradient boosting methods [Zhao 2020].

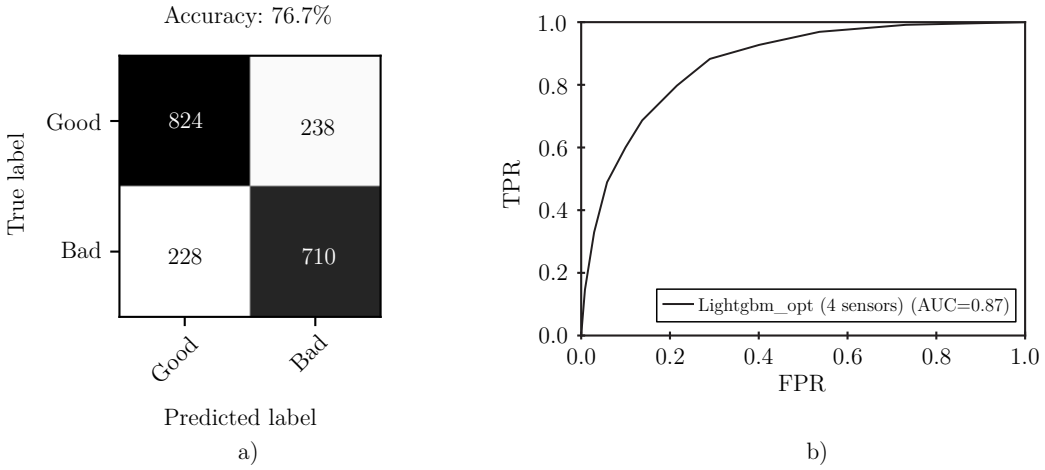

Figure 5.16: LightGBM model evaluation with 4 sensors by a) confusion matrix and b) ROC.

In order to understand when and why the model fails, defective parts were analysed. For this purpose, the zones with excessive void and/or unfilled, as well as their position, were compared when the model was correct (TN) and when the model failed (FP)

(Figure 5.17). The results show that the zones furthest from the injection point are the most critical, as the model does not ensure total prediction success for defects located in these zones. Nevertheless, when the NDI is needed, it may be sufficient to analyse the zones where the model can fail. Thus, ML-based NDI can be a way to reduce costs and speed up quality control process.

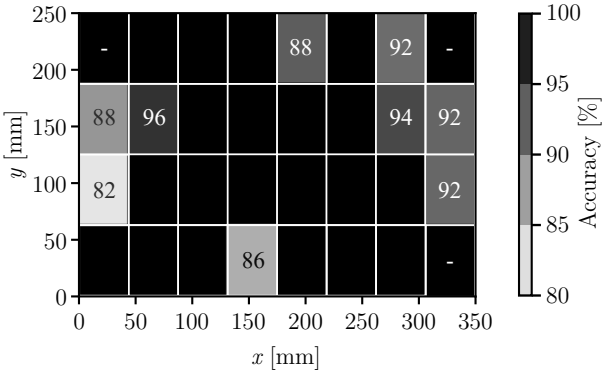

Figure 5.17: Void and/or filling detecting accuracy by zones.

To obtain a more concrete result about the position of the defect, the model was scaled to the quality prediction of each zone. In this way, the model was not only able to predict the overall quality of the part but also to detect the defective zone location. As a validation, the quality of the S_I, S_{II} and S_{III} (analysed in the previous section) simulations was predicted.

In Figure 5.18, ML and FEM results are superimposed, it can be seen how the defect predictions of the ML model matched FEM results in all cases. In the first case, S_I (Figure 5.18a), the ML model correctly predicted its quality and did not predict any defective zone. In the second case, S_{II} (Figure 5.18b), there were zones with high void content, and the model was able to detect such zones (Zones 7, 16, 24 and 27). Finally, in the same way, in the S_{III} simulation (Figure 5.18c), the ML model is also able to detect the position of the unfilled zone (Zone 9). These results are promising as they allow to detect the position of the defects in the fabricated parts. In this way, decisions such as rejecting the part or reworking the defective zones can be made and the robustness of the RTM process is improved.

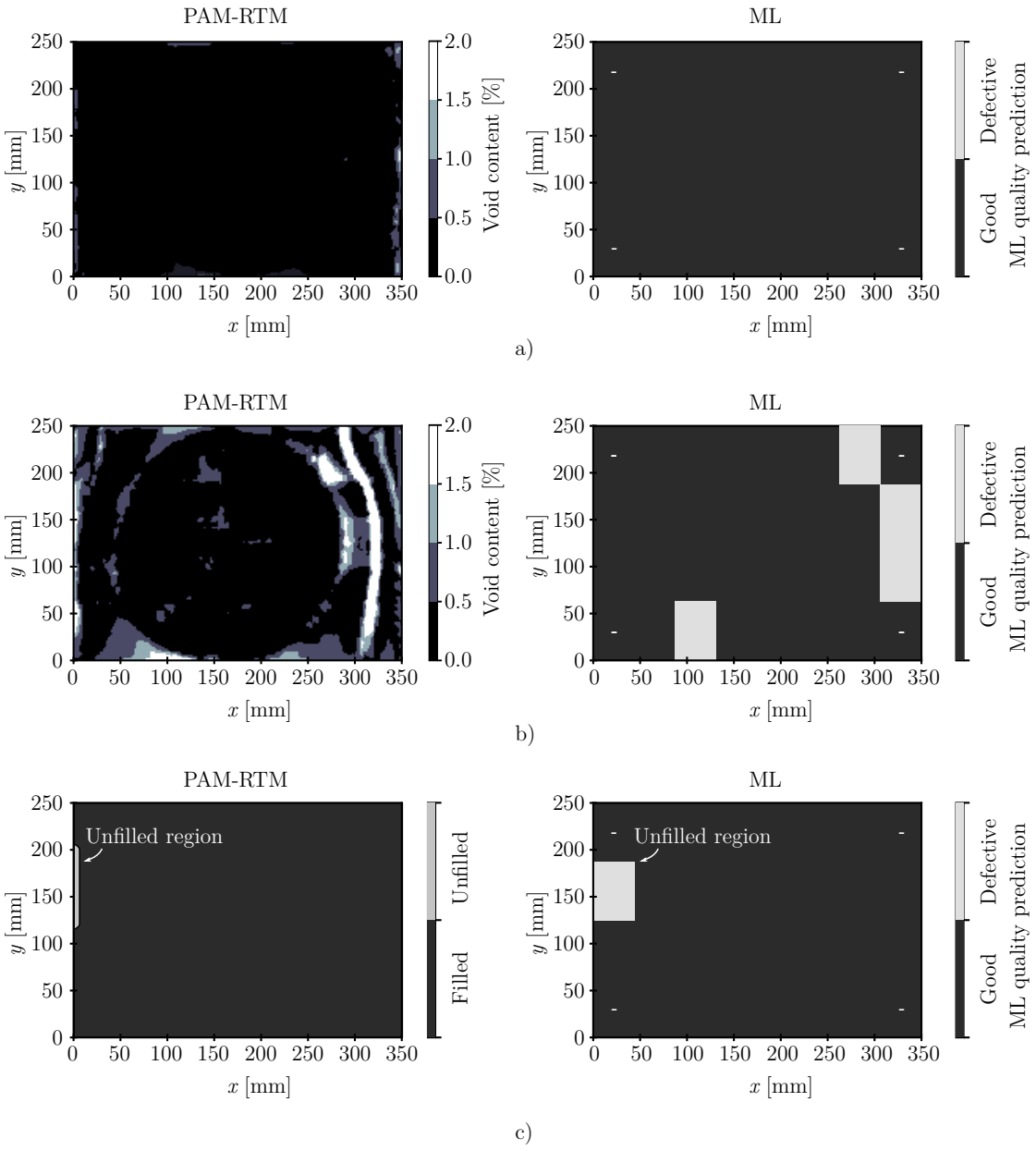

Figure 5.18: PAM-RTM results vs ML results.

Finally, the computational cost of Finite Element Method (FEM) and Machine Learning (ML) were compared. For that the average running time and data size of each simulation was compared (Table 5.5). It can be stated that once the ML model is trained, the predictive model reduce the computational time and storing data size comparing to FEM models. This reduction can be beneficial for its implementation in the process line where the time available for the diagnosis of each part is limited.

Table 5.5: Computational cost of FEM model and ML model.

Method	Running time [s]	Data size [MB]
FEM	360	27,000
ML	1	600

5.4 Conclusions

Part-quality after injection stage of Resin Transfer Moulding has been diagnosed based on binary classification of Supervised Learning trained with synthetic datasets. Diagnosis tools like SL are necessary, since the local permeability variability generates parts with unacceptable levels of void and/or dry zones. In fact, even if variable injection strategies for reducing void content are used, the amount of defective parts is high. Results of the 10,000 numerical simulations run with different permeability maps showed that 1582 have void content defects, 1959 have dry zone defects and 1418 have both. That is, 4959 simulations were classified as defective compared to 5041 good ones. This provided a balanced data set (with a ratio of almost 1:1) to avoid training problems in binary classification.

The algorithm and the hyper-parameters that defines the predictive model were chosen automatically by the use of TPOT and Hyperopt libraries. AutoML results showed that XGB and LightGBM were the most accurate models for predicting the filling quality of RTM, both with an AUC value of 0.92, whereas the ACC values are 84.9% and 83.35%, respectively. In this way, the application of AutoML is validated in a complex process like RTM and shows that it may useful tool for process engineers as it automates part of the pipeline. It has been demonstrated that Ensemble methods based on decision trees are the optimal ones for the selected case study, coinciding with several works of literature.

Feature importance analysis identified that the last filled zones have the highest importance when predicting the overall quality of the part. Consequently, the amount of pressure monitoring points can be reduced. The performance of the models fed with the pressure evolution of the four monitoring points located at these zones showed that LigthGBM is more reliable than XGB, being its ACC 76.7% and AUC 0.87. Reducing the amount of monitoring points from 32 to 4 reduces the diagnosis quality, but it is still above 2-sigma. Another advantage of using SL instead of conventional FEM process-simulations is the lower computational cost, reducing computing time from 360 s to 1 s (after training) and reducing the data-size from 27 GB to 600 MB.

Training SL predictive models with synthetic dataset may be an effective approach to get accurate diagnosis of the impregnation quality with an accuracy above 2-sigma. The predictive model allowed the identification of the number and location of the pressure sensors in the mould, and it may be fast enough to be integrated in real process between injection and curing stages. The present case study was focus on permeability variation due

to local binder content, but the methodology can be extrapolated to any other permeability variation sources, such as different fibre compaction level, nesting effect, shearing or others.

Once the injection is complete, the predictive model may be able to determine if the part is defective or not. If it is defective, the part can be rejected once it has sufficient stiffness without waiting for total curing. This might be a substantial improvement in saving time and energy to improve the robustness of the RTM process.

6

Machine Learning based surrogate modelling for low velocity impact

Contents

6.1 Introduction

The results obtained in Chapter 4 concluded that manufacturing parameters in RTM processes have non-negligible effects on void generation, and thus, on the impact properties of the composite. Furthermore, in Chapter 5 it is shown that by using supervised predictive models it is possible to detect the generation of voids during the injection phase. In this way the RTM process can approach zero defect manufacturing (ZDM).

However, a paradigm shift is occurring in manufacturing engineering, going from zero-defect manufacturing to in-service performance-based production [Wuest 2014]. The new approach does not focus on manufacturing defect-free parts, but parts with a number of defects that do not compromise its structural integrity. For that, the manufacturing system must be enhanced with material science and process technology intelligence, and establish accurate Processing–Structure–Property–Performance (PSPP) relationships [Gomez 2021]. Kärger *et al.* [Kärger 2015], following the PSPP approach, introduced a continuous virtual process chain (CAE chain) capable of continuously simulating the RTM process of CFRP parts. Through holistic simulation with FEM-based data exchange, they predict the in-service performance based on the post-draping fibre orientations. Same approach could be used to introduce void defects into the virtual chain, and predict the impact response of the part being fabricated. Nevertheless, CAE chains based on FEM concatenation are not computationally feasible and are not suitable for integrating as an on-line quality assessment [Henning 2019].

The contribution of this chapter is the generation of ML-based surrogate model that allows relating the impregnation defects, such as voids, with the impact response of the part. This model builds a fast quality assessment system based on real in-service performance. For this purpose, a FEM model of a low velocity impact considering void content has been developed and experimentally validated. The void map was parameterised, modifying the position and level of the defect, to generate 2050 different impact performance cases. The predictive model built from these samples, was based on supervised learning classification, as well as single-output and multi-output regression and the link from structure to final performance was done (Figure 6.1).

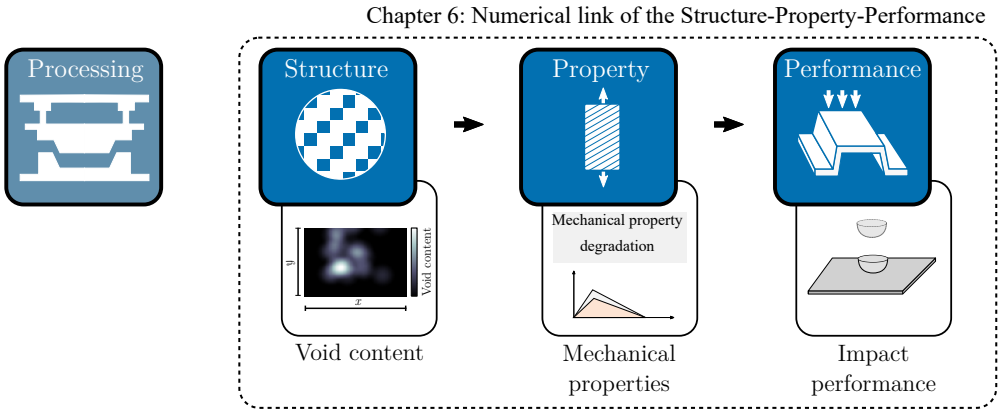

Figure 6.1: Numerical Structure-Property-Performance link.

6.2 FEM-based numerical model of the low velocity impact

6.2.1 Damage modelling

During the out-of-plane impact event, both matrix and fibre breakage and delamination between the different plies occur and can interact with each other. However, due to the complexity of modelling both the onset and evolution of failure modes, intra-laminar damage and inter-laminar damage are modelled separately using a stacked shell approach [Sachse 2020; Zhu 2010]. Shells represent each composite ply and they are modelled as orthotropic elastic material that include intra-laminar damage due to fibre and matrix micro-cracking [Dassault Systèmes 2021]. Moreover, each ply are connected with cohesive elements that model inter-laminar damage or delamination. The properties of the laminate were based on the work of Sachse *et al.* [Sachse 2020], as the material used by them also was a biaxial carbon NCF-epoxy composite. The fibre used by them was a carbon fibre biaxial non-crimp fabric (TENAX-E HTS40 F13 12K) with a weight of 557 g/m^2 close to the 610 g/m^2 fabric employed in this study. Regarding the resin, they used a mono-component Epoxy RTM6, instead the bi-component Epoxy (Araldite XB 3585) and hardener (Aradur 3475) used in the present work. Some parameters were not characterized by them and they adapted based on data available in literature for similar materials.

Intra-laminar damage initiation and propagation

Due to the computational cost associated with modelling the physical phenomena occurring at the microscopic level, intra-laminar damage models based on continuum damage mechanics are widely used in literature [González 2017]. For that, damage variables are used to quantify the level of damage and reduction of material properties. The intra-laminar behaviour of the composite is assumed to be elastic-linear until the damage initiation criterion is reached. At this point, the stiffness of the composite starts to degrade until absolute damage is reached. Hashin's physically-based failure criteria [Hashin 1973], implemented in commercial code Abaqus®, was used for the intra-laminar damage initiation. This failure criteria takes into account four main failure modes; (i) fibre tension $F_{\mathrm{f}}^{\mathrm{t}}$, (ii) fibre compression $F_{\mathrm{f}}^{\mathrm{c}}$, (iii) matrix tension $F_{\mathrm{m}}^{\mathrm{t}}$, and (iv) matrix compression $F_{\mathrm{m}}^{\mathrm{c}}$. Failure is activated when damage activation conditions reaches the value of one in any of the following criteria:

$$F_{\mathrm{f}}^{\mathrm{t}} = (\frac{\sigma_{11}}{X^{\mathrm{T}}})^2 + \alpha(\frac{\sigma_{12}}{S^{\mathrm{L}}})^2 = 1 \tag{6.1}$$

$$F_{\mathrm{c}}^{\mathrm{t}} = (\frac{\sigma_{11}}{X^{\mathrm{C}}})^2 = 1 \tag{6.2}$$

$$F_{\mathrm{m}}^{\mathrm{t}} = (\frac{\sigma_{22}}{Y^{\mathrm{T}}})^2 + \alpha(\frac{\sigma_{12}}{S^{L}})^2 = 1 \tag{6.3}$$

$$F_{\mathrm{m}}^{\mathrm{c}} = (\frac{\sigma_{22}}{2S^{\mathrm{T}}})^2 + [(\frac{Y^{\mathrm{C}}}{2S^{\mathrm{T}}})^2 - 1]\frac{\sigma_{22}}{Y^{\mathrm{C}}} + (\frac{\sigma_{12}}{S^{\mathrm{L}}})^2 \tag{6.4}$$

where σ_{11}, σ_{22} and σ_{33} are the stress applied in the fibre direction, transverse fibre direction and the in-plane shear, respectively. Regarding material strengths, X^{T} represents the longitudinal tensile strength, X^{C} the longitudinal compressive strength, Y^{T} the transversal tensile strength, Y^{C} the transversal compressive strength, S^{L} the in-plane (Longitudinal) shear strength and S^{T} out-of-plane (Transversal) shear strength. The coefficient α determines the contribution of shear to the onset of damage in the stress criterion in the fibre direction. The intra-laminar elastic properties are summarized in Table 6.1 and elastic strengths in Table 6.2.

Table 6.1: Intra-laminar elastic properties [Sachse 2020].

Description	Unit	Variable	Value
Longitudinal Young modulus	GPa	E_1	140
Transversal Young modulus	GPa	$E_2 = E_3$	8.6
Principal Poisson's ratio	-	ν_{12}	0.3
Shear modulus	GPa	$G_{12} = G_{23} = G_{13}$	4.2

Table 6.2: Intra-laminar elastic strengths [Sachse 2020].

Description	Unit	Variable	Value
Longitudinal tensile strength	MPa	X^{T}	2160
Longitudinal compressive strength	MPa	X^{C}	1236
Transversal tensile strength	MPa	Y^{T}	67
Transversal compressive strength	MPa	Y^{C}	67
In-plane shear strength	MPa	S^{L}	70

Prolonged loading after reaching the damage initiation criterion results in degradation of the stiffness properties as damage variables increase. These damage variables range from zero (not damaged) to one (fully damaged) based on the fracture energy dissipated during the damage process, being this a generalization of the approach proposed by Camanho *et al.* [Camanho 2002]. To alleviate from the meshing dependence, the characteristic length is introduced in the formula and thus the constitutive law is expressed as an equivalent stress-displacement relation. Formulae for obtaining the equivalent displacement $\delta_{I,\mathrm{eq}}$ and equivalent stress $\sigma_{I,\mathrm{eq}}$ from the characteristic length L_{c} for each failure mode can be found in the literature [Dassault Systèmes 2021]. Assuming that the damage evolution (i.e. softening) is linear, the damage parameters are calculated in this way:

$$d_I = \frac{\delta^{\mathrm{f}}_{I,\mathrm{eq}}(\delta_{I,\mathrm{eq}} - \delta^{0}_{I,\mathrm{eq}})}{\delta_{I,\mathrm{eq}}(\delta^{\mathrm{f}}_{I,\mathrm{eq}} - \delta^{0}_{I,\mathrm{eq}})} \tag{6.5}$$

where $\delta^0_{I,\mathrm{eq}}$ is the equivalent displacement of the onset of damage for each failure mode and $\delta^{\mathrm{f}}_{I,\mathrm{eq}}$ is the equivalent displacement of totally damaged material calculated as:

$$\delta^{\mathrm{f}}_{I,\mathrm{eq}} = \frac{2G^{\mathrm{f}}_I}{\delta^0_{I,\mathrm{eq}}} \tag{6.6}$$

where, G^{f}_I is the fracture energy for each of the four main failure modes ($G^{\mathrm{f}}_{\mathrm{ft}}$, $G^{\mathrm{f}}_{\mathrm{fc}}$, $G^{\mathrm{f}}_{\mathrm{mt}}$ and $G^{\mathrm{f}}_{\mathrm{mc}}$). The intra-laminar fracture energies are shown in Table 6.3.

Table 6.3: Intra-laminar fracture energies in longitudinal and transversal direction [Sachse 2020].

Description	Unit	Variable	Value
Longitudinal tensile fracture energy	N/mm	$G^{\mathrm{f}}_{\mathrm{ft}}$	120
Longitudinal compressive fracture energy	N/mm	$G^{\mathrm{f}}_{\mathrm{fc}}$	30
Transverse tensile fracture energy	N/mm	$G^{\mathrm{f}}_{\mathrm{mt}}$	0.385
Transverse compressive fracture energy	N/mm	$G^{\mathrm{f}}_{\mathrm{mc}}$	1.5

Inter-laminar damage initiation and propagation

The cohesive elements placed between the plies were modelled with linear elastic traction-separation behaviour. This linear-elastic behaviour is followed by an initiation and evolution of damage similar to that of intra-laminar elements. The uncoupled traction-separation law for the linear-elastic behaviour, $t = \mathbf{K}\delta$, is defined as:

$$\begin{Bmatrix} t_{\mathrm{n}} \\ t_{\mathrm{s}} \\ t_{\mathrm{t}} \end{Bmatrix} = \begin{bmatrix} K_{\mathrm{nn}} & 0 & 0 \\ 0 & K_{\mathrm{ss}} & 0 \\ 0 & 0 & K_{\mathrm{tt}} \end{bmatrix} \begin{Bmatrix} \delta_{\mathrm{n}} \\ \delta_{\mathrm{s}} \\ \delta_{\mathrm{t}} \end{Bmatrix} \tag{6.7}$$

where $\mathbf{K}$ refers to the stiffness matrix of the cohesive elements, t refers to the interface traction of the cohesive elements and δ refers to the displacement of the cohesive elements. The subscripts t, n and s refer to the normal and two shear directions,sliding and tearing, respectively.

After this first range of linear elastic behaviour, at one point the inter-laminar damage (delamination) begins. The damage initiation criterion chosen was the maximum stress criterion, which dictates that damage is initiated when the maximum contact stress ratio reaches one [Dassault Systèmes 2021]:

$$\max\{\frac{\langle t_{\mathrm{n}}\rangle}{t^0_{\mathrm{n}}} + \frac{t_{\mathrm{s}}}{t^0_{\mathrm{s}}} + \frac{t_{\mathrm{t}}}{t^0_{\mathrm{t}}}\} \tag{6.8}$$

where t^0_{n}, t^0_{s} and t^0_{t} are the maximum values of contact stress for normal, sliding and tearing stresses. Note that Macaulay brackets indicate that a pure compression state does not initiate damage in normal direction. The inter-laminar elastic properties are showed in Table 6.4.

Table 6.4: Inter-laminar damage initiation properties [Sachse 2020].

Description	Unit	Variable	Value
Stiffness penalty in normal direction	N/m^3	K_{nn}	4200
Stiffness penalty in 1st and 2nd shear direction	N/m^3	$K_{ss} = K_{tt}$	4200
Max. shear stress in the normal direction	MPa	t_n^0	65
Max. shear stress in the 1st and 2nd shear direction	MPa	$t_s^0 = t_t^0$	65

The damage evolution is based on fracture energy, and the Benzeggagh-Kenane (BK) model was used for mixed mode behaviour [Kenane 1997]. The resulting fracture toughness for mixed-mode G^C is calculated:

$$G^C = G_n^C + (G_s^C - G_n^C)(\frac{G_{shear}}{G_T})^\eta \tag{6.9}$$

where G_T denotes the total energy done by normal and shear traction based on energy (G_n+ G_s+ G_t) and G_{shear} refers to the energy done by shearing traction (G_s+ G_t). Regarding the critical fracture energies G_n^C, G_n^C, and G_n^C are the critical fracture energy that cause failure in normal, first and second shear direction respectively. Finally, η is an empirically derived parameter (from mixed-mode test) called the B-K coefficient. The inter-laminar damage properties are summarized in Table 6.5.

Table 6.5: Inter-laminar damage propagation properties [Sachse 2020].

Description	Unit	Variable	Value
Inter-laminar fracture toughness in Mode I	N/mm	G_n^C	0.385
Inter-laminar fracture toughness in Mode II	N/mm	$G_s^C = G_t^C$	1.19
B-K coefficient	-	η	2.58

6.2.2 Geometrical modelling and boundary conditions

A 3D FE model was develop for the representation of the impactor and composite plate system. Two different geometries were generated (Figure 6.2) which differ only in the size and clamping configuration. The first model (Figure 6.2a) was developed to check the accuracy of the numerical results compared to the experimental results, and it replicated the experimental test conditions. In this model, the Ø60 mm specimen was clamped by means of an annular ring with an inner and outer diameter of Ø40 mm and Ø60 mm, respectively. The second model (Figure 6.2b), was developed as a particular case study used throughout the study. In it, a flat piece of 350 mm × 250 mm was modelled and the clamping was at the edge of the entire rectangular plate.

All configuration details explained hereafter are the same for both models and will therefore be explained only once. The laminate $[0/90]_{2s}$ was symmetrical and each 0/90 layer was modelled separately as two unidirectional plies (0.75 mm each 0/90 ply).

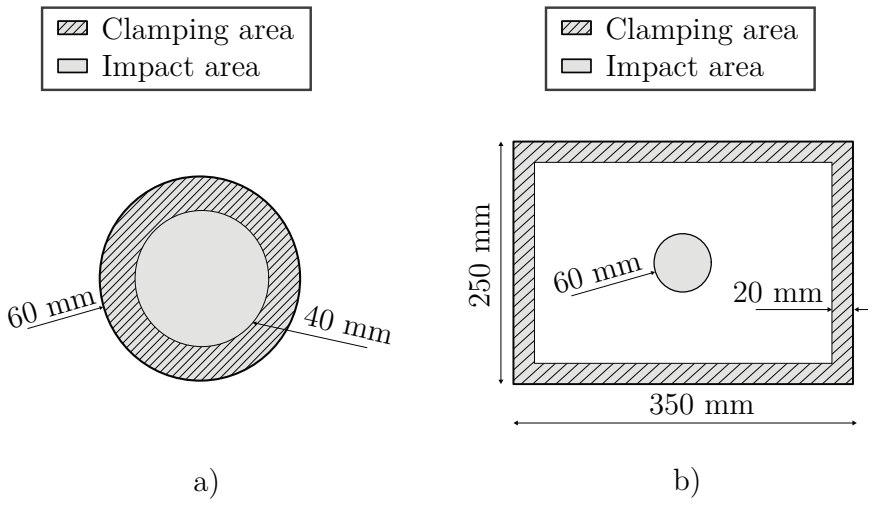

Figure 6.2: Composite plate model for a) experimental validation and b) the case study.

A hemispherical impactor with a diameter of 20 mm was used and the corresponding initial and boundary conditions were applied (Figure 6.3). An initial velocity of -4427 mm/s was applied in the Z-axis (Velocity of a falling object after one meter) and the translation and rotations of the impactor were restricted except for the Z-axis translation. The applied impact energy was controlled through the weight of the impactor as the initial velocity was fixed. A mass of 2.04 kg was applied to achieve an impact energy of 20 J.

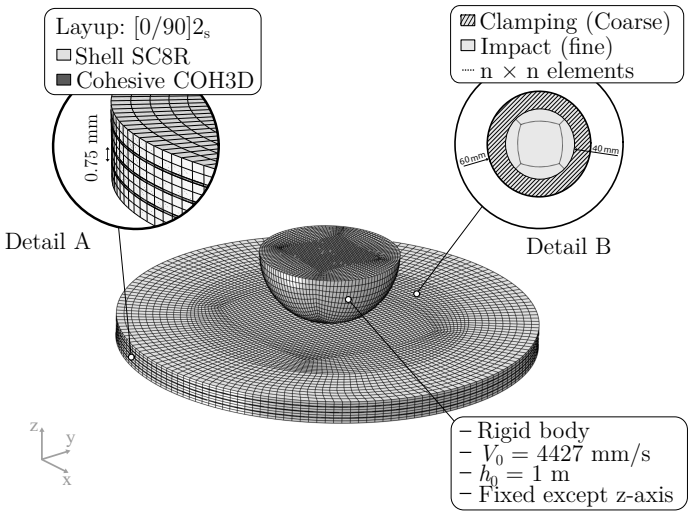

Figure 6.3: Geometry and boundary conditions of the FEM model of a low velocity impact.

6.2.3 Mesh density and element type

The FE semi-spherical impactor was modelled as four node-3D bilinear discrete rigid quadrilateral-R3D4 elements. The element overall size was 0.35 mm × 0.35 mm with a total amount of 4202 finite elements in impactor part. Laminates was composed of four

plies of a biaxial (0/90) NCF of 50k high resistance carbon fibre compacted to 3 mm. Each of the laminates was modelled separately as unidirectional plies (0.75 mm each ply) using an 8-node first-order interpolation, hexahedral continuum shell elements with reduced integration (SC8R). The cohesion between plies was created with a zero-thickness 8-node three-dimensional cohesive element (COH3D8). In order to reduce the computational cost, a fine mesh in the central impact zone was combined with a coarser mesh in the furthest zone. Structured O-grid meshing, based on multi-block meshing method, was used for the circular plate in order to avoid highly skewed elements that could alter the results (detail B in Figure 6.3). Thus, hexahedral elements were used in the critical impact zone, which are suitable for contact problems [Dassault Systèmes 2021]. In order to define the number of elements in the impact zone, three different grids, $n \times n$ where n is the number of elements, were compared: (i) 20×20, (ii) 40×40 and, (iii) 60×60. In all cases, there were two elements in thickness direction in each of plies.

6.2.4 Contact modelling

It has been observed in literature that friction can considerably affect the absorption capacity of composite materials [Esnaola 2016]. This is due to the tangential interaction when delamination occurs between the laminates. The inter-laminar friction coefficient in the aligned $0°/0°$ interfaces can be around 0.2 and on the other hand, when the interfaces are not aligned $0°/90°$ this coefficient can be as high as 0.8. Therefore, an intermediate value of 0.5 was used for all types of interactions as was done by many authors [Shi 2012; Lopes 2014]. In addition, the contact behaviour between the impactor and the composite laminate was defined by hard contact.

6.2.5 Void effect

The effects of process-induced voids on the mechanical properties of composite materials was implemented using the method proposed by Dong *et al.* [Dong 2016]. Among the proposed models for property degradation based on void content, both fibre-dominated and matrix-dominated properties can be found. Table 6.6 shows the property degradation models for different void V_v and fibre contents V_f. The numerical coefficients of the reduction models are shown rounded to their second decimal in order to increase readability. It can be observed that matrix-dominated properties are the most affected by void presence, whereas fibre-dominated properties have little or no effect.

Table 6.6: Property degradation models due to void content [Dong 2016].

Description	Variable	Value
Longitudinal Young modulus [GPa]	E_1	$1 - 1.76V_\mathrm{v}$
Transversal Young modulus [GPa]	$E_2 = E_3$	$1 - (2.79 - 3.09V_\mathrm{f})V_\mathrm{v}$
Shear modulus [GPa]	$G_{12} = G_{23}$	$1 - (1.87 - 1.15V_\mathrm{f})V_\mathrm{v}$
Longitudinal tensile strength [MPa]	X^T	No effect
Longitudinal compressive strength [MPa]	X^C	No effect
Transversal tensile strength [MPa]	Y^T	
Transversal compressive strength [MPa]	Y^C	$(0.49 - \frac{0.03}{V_\mathrm{f}^2})V_\mathrm{v}^{-(0.15+\frac{0.02}{V_\mathrm{f}^2})}$
In-plane shear strength [MPa]	S^L	

Regarding inter-laminar strengths in normal and two shear directions, the reduction model for the ILSS proposed by Dong *et al.* [Dong 2016] was used. It is the same as the other matrix-dominated properties (Table 6.7).

Table 6.7: Inter-laminar strengths degradation model due to void content [Dong 2016].

Description	Variable	Value
Max. shear stress in the normal dir.	t_n^0	$(0.49 - \frac{0.03}{V_\mathrm{f}^2})V_\mathrm{v}^{-(0.15+\frac{0.02}{V_\mathrm{f}^2})}$
Max. shear stress in 1$^\mathrm{st}$ and 2$^\mathrm{nd}$ shear dir.	$t_\mathrm{s}^0 = t_\mathrm{t}^0$	

6.3 Experimental validation of the FEM model

6.3.1 Mesh dependency study

In this section the results obtained from the FEM impact model are shown, and compared with the results obtained from the experimental tests. As mentioned in the previous section, three impact zone mesh densities were compared: i) 60 × 60 elements, ii) 40 × 40 elements, and iii) 20 × 20 elements. In order to compare them quantitatively, the computational time and the following characteristic impact parameters were taken into account: the force when delamination was initiated (F_d), maximum force (F_max), maximum displacement (δ_max), dissipated energy (E_dis), and the contact time (t_c).

As it is shown in Figure 6.4, the F_d for the experimental test was around 3.13 kN. In the case of the numerical results, the F_d for the finer mesh (60 × 60 elements) was 3.01 kN, while for the 40 × 40 elements and 20 × 20 elements grids, it was 3.05 kN and 3.38 kN, respectively. In that point the part began to delaminate and therefore started losing stiffness. After the onset of delamination, its propagation was similar in all cases. In the 60 × 60 mesh, the beginning of fibre failure was observed at 7.21 kN similar as in the experimental test, 7.30 kN. In the 40 × 40 mesh this failure occurred at 7.46 kN and in the 20 × 20 mesh, it was not generated any fibre failure. Finally,

it can be seen that the contact time in all cases was very similar to the experimental contact time, which was around 3.7 ms.

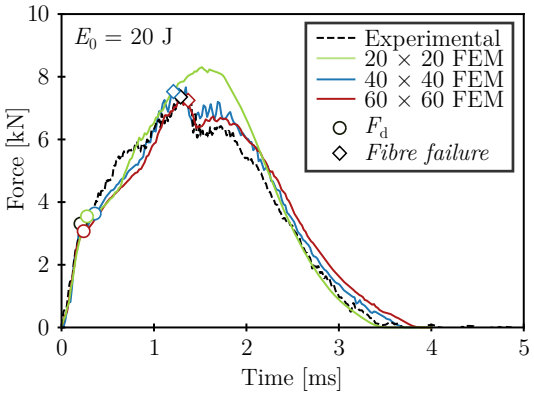

Figure 6.4: Effect of mesh in $F(t)$ curve.

In addition, the tests were also analysed in terms of force-displacement and energy-time curves (Figure 6.5). Regarding the maximum displacement (Figure 6.5a), the cases where fibre breakage was observed result in a slightly higher displacement due to the loss of stiffness. Moreover, these same cases, due to fibre breakage, dissipate more energy and come closer to the 15 J dissipated experimentally (Figure 6.5b).

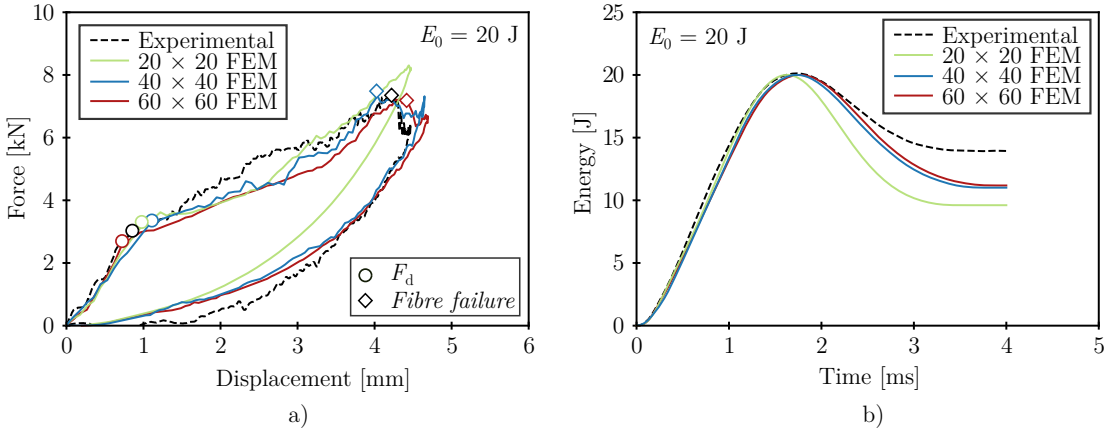

Figure 6.5: Effect of mesh in the model validation for a) force-deformation, and b) energy-time curves.

The absolute error with respect to the real F_{max}, Maximum displacement and E_{max} were quantified, taking into account the computational time for each mesh size (Table 6.8). It can be seen that the 40 × 40 meshing achieved an absolute error of less than 5% in F_{max} and maximum displacement while the computational time was less than 1 hour. Therefore, it was decided that the 40 × 40 mesh was suitable for further analysis, as it provided the best balance between accuracy and computational time.

Table 6.8: Mesh size errors.

Mesh size	F_{max} error[%]	Displ. error[%]	E_{dis} error[%]	Time [min]
20 × 20	13	1	45	7
40 × 40	2	4	22	33
60 × 60	1	7	18	111

In order to determine the validity of the 40 × 40 model, a wider range of impact events considering different damage levels were explored (Figure 6.6). Three different energies were selected, one for each damage zones detected in Chapter 4. Impact energy in the supercritical I regime (4 J), where the sample suffered delamination and partial matrix rupture (Figure 6.6a). Impact energy in supercritical regime II (20 J), where the sample, in addition to delamination and matrix breakage, started to suffer fibre failure (Figure 6.6b). And finally, impact energy in the supercritical II regime at perforation energy (55 J), where the fibre was also completely fractured and the impact passes through the sample. However, at so high energies the model was not able to simulate the fibre perforation correctly and the results were not accurate. It is believed that this may be due to the non-linear nature of fibre failure, which was very present at this impact energy.

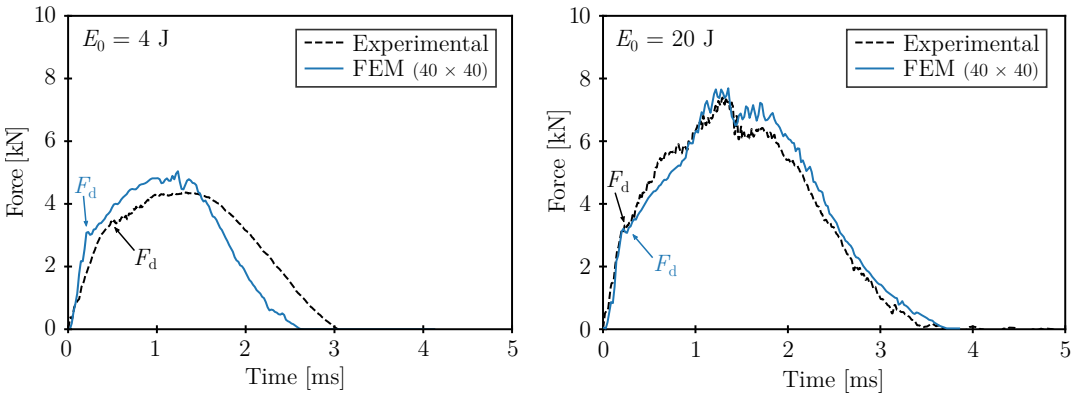

Figure 6.6: Numerical and experimental correlation for a) 4 J impact, and b) 20 J.

As 20 J was the maximum energy which the model performed correctly, the study in this chapter has proceeded with 20 J impacts.

6.3.2 Damage analysis

The model was able to predict the behaviour of a specimen subjected to 20 J impacts in terms of force, energy and displacement. In addition, the result generated in the numerical simulation for the intralaminar damage (Figure 6.7) showed the damage generated in the lower layer of the sample in terms of matrix and fibre damage under tensile stresses.

Although it was not possible to obtain the result of both in the experimental case, the numerical results shown a logical pattern.

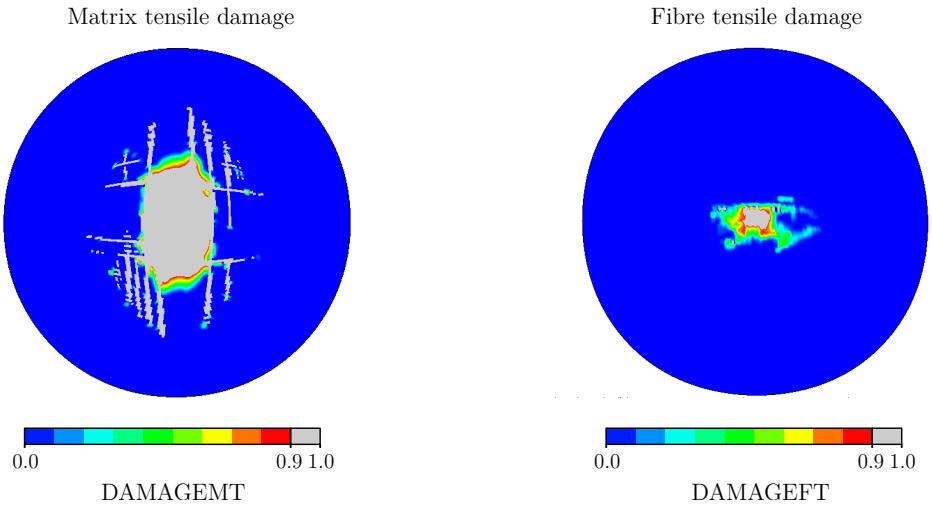

Figure 6.7: Intra-laminar damage analysis in the lower layer.

The tested specimen was subjected to non-destructive ultrasonic examinations (C-scan) to assess the shape and extent of post-impact delamination following the method described previously (Subsection 4.2.5).

The delamination generated during the experimental impact was compared with the delamination obtained from the numerical model (Figure 6.8). It is worth mentioning that both the experimental and numerical model results measure delamination in different ways. In the experimental case, the signal attenuation was measured and therefore the result obtained was the overlap of the delaminated surfaces. In the case of the numerical result, the delamination layer is shown.

Although in the experimental case the boundary was somewhat more irregular, it is clearly observed that the delamination diameter is similar in both cases. The delaminated area was similar in both cases; an error of 5% was measured.

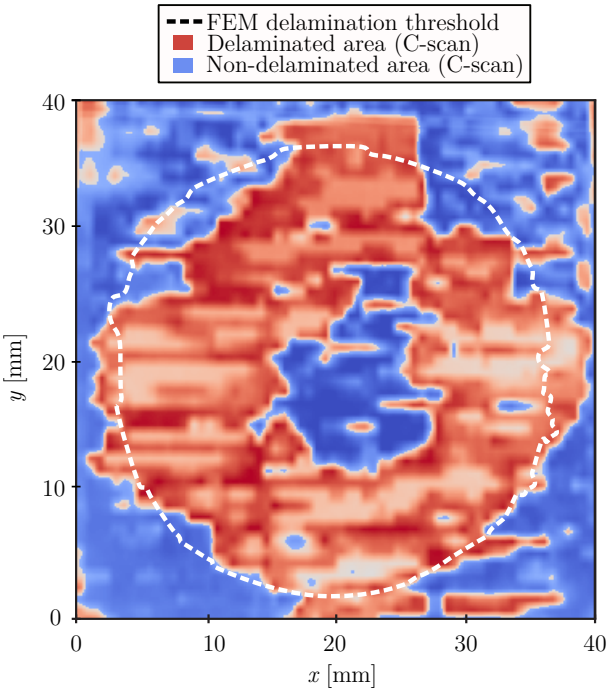

Figure 6.8: Delamination area for experimental and numerical model.

6.3.3 Void effect

For the analysis of the effect of the void on the impact properties, both the experimental test and numerical model were compared for two void contents: (i) low void content (<0.5%) (Figure 6.9a), and (ii) high void content (4%) (Figure 6.9b). As observed in Section 6.3.1, the experimental and numerical curves (40 × 40 mesh) were very similar. Moreover, it can be observed that when voids defects were introduced, the trend was similar in the experimental and numerical model as well. F_{d} was slightly lower in the cases of high void content; 4% in the numerical case and 8% in the experimental cases. This caused the curve of high void content to fall below the low void content curve, up to the F_{max}. The numerical model replicates the experimental behaviour well as it reaches the F_{max} point slightly earlier, around 1 ms. The reduction of F_{max} in the experimental case was 9% and 13% in the numerical case. For the contact time, differences were observed in the experimental case, being slightly longer in the case of high void content (4%). However, in the numerical case there were hardly any differences between both (1%). Thus, it can be concluded that the FEM model for the impact behaviour of void-dependent NCF fibre-reinforced epoxy composites worked accurately.

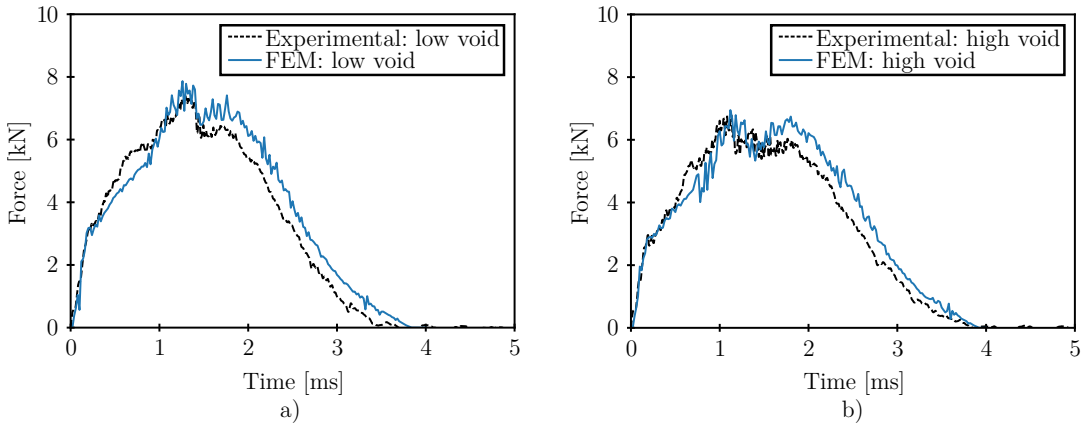

Figure 6.9: Comparison of experimental and numerical $F(t)$ curves for a) low void content (<0.5% void) and b) high void content (4%) samples.

6.4 Machine Learning-based surrogate model for impact test

As demonstrated in Chapter 5, by acquiring the pressure signal and using machine learning techniques, it was possible to detect the location and level of voids in the RTM manufactured parts. However, defects can have a very different effect depending on their location, so it is inadequate to discard a part only by the void content.

The classic FEM method could be useful to know the mechanical performance of each manufactured part by knowing its micro-structure (the position and level of void). In classic FEM, after defining geometry, material and boundary condition parameters, the partial differential equations are solved to obtain simulation results. This method allows very accurate results to be obtained, but at a certain computational cost.

In this work, it is proposed the generation of three surrogate models based on ML that determine the structural quality of the part in a fast and accurate way. The low computational cost makes them suitable for implementation in the RTM process, unlike the computational costly classical FEM models. The generated models are three: (i) classification model, (ii) single-output regression model and, (iii) multi-output regression model (Figure 6.10).

The three proposed methods were ordered from the simplest, the classification model, to the most complex, the multi-output regression model. For both the classification model and the single-output regression, it was necessary to define a critical parameter. Among the critical variables $\delta_{\max}$, $F_{\max}$ and $E_{\max}$ were identified and there were compared taking into account the numerical-experimental error of each variable. In addition, the numerical noise present in the force-time, energy-time and displacement-time curves was analysed.

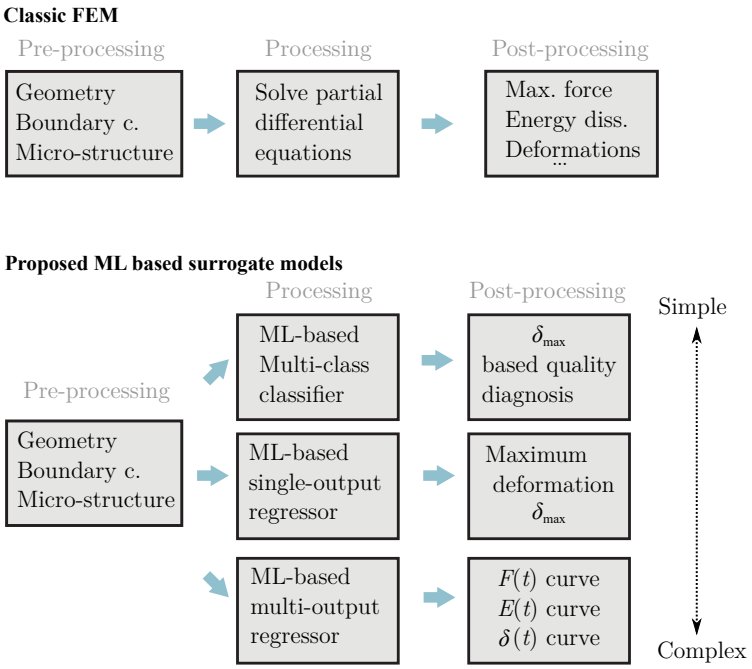

Figure 6.10: The methodology followed by a) classic FEM and b) proposed ML based surrogate models.

6.4.1 Data description

The impact simulations performed with Abaqus® were used as samples for model training. Those simulations were parameterised for the generation of defects with different locations and void levels. The code for the simulations was parameterised using Python language, making it possible to generate many different defect maps (in terms of defect position and void content). Furthermore, the programming enabled to launch it and acquire the output data in an automated manner. Time series representing force, displacement and energy dissipation were extracted from each simulation that lasted on average 60 minutes.

In a extensive review done by Mehdikhani *et al.* [Mehdikhani 2019], they analysed the effect of voids on a variety of mechanical properties. Most of the works cited in that review analysed specimens with voids ranging from 2% to 8%. Therefore, for this work, it was decided to use these two extremes and also to analyse another voids level in between, which was 6%.

To determine the size of the dataset used, similar works were analysed where ML techniques were applied for the prediction of mechanical properties. Qi *et al.* [Qi 2019] achieved an error rate between 18 % and 7% for different mechanical properties with 500 samples. Similarly for the prediction of mechanical properties, Liu *et al.* [Xing Liu 2022] achieved an R^2 of between 0.85 and 0.98 using 1900 samples. In this way, during the present research work, 2050 simulations were performed, being 670 with local defects of 2% voids, 680 with local defects of 4% voids and 700 with local defects of 10% voids

(Table 6.9). These 2050 simulations were used for training and testing the predictive models. In addition, it was decided to use new test samples with different void levels. These new samples had a different void level than the ones used during training (which were 2%, 4% and 8%) (Figure 6.11). 15 new cases were tested and their void levels were between 1% and 10% randomly located in the part.

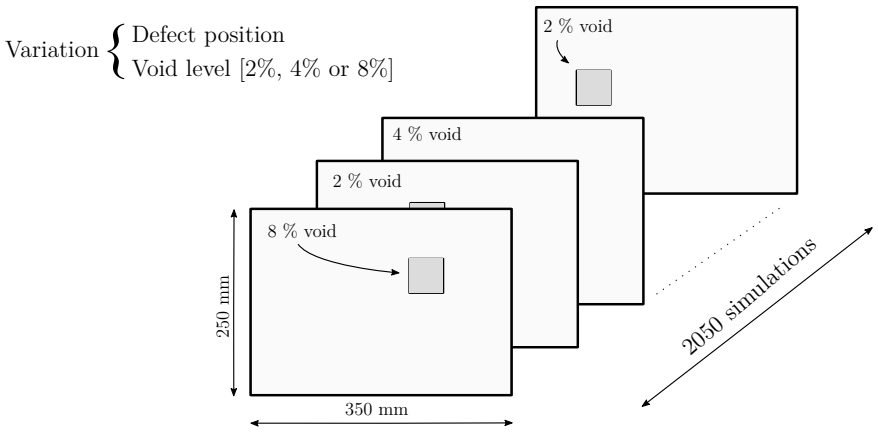

Figure 6.11: Parametrisation of position and void level to generate 2050 simulations.

Table 6.9: Description of the data used for training and testing.

Description	Void content	Total simulations	Defect position
Training and testing	2%	670	Random
	4%	680	Random
	8%	700	Random
New testing	Random $\{1\% - 10\%\}$	15	Random

For both the classification model and the single-output regression, it was decided to use the critical variable $\delta_{\max}$. E_{dis} was discarded, as it was the most inaccurate output calculated by the FEM model. Regarding F_{dis}, the force-time curves calculated using the FEM model were very accurate but the intrinsic noise of the curves added some unwanted variability for $E_{\max}$ prediction.

In the classification model, maximum displacement $\delta_{\max}$ criterion was established and three classes were defined: the most favourable class being (class 2); $\delta_{\max} \leq 7.75$ mm, the intermediate class (class 1); $7.75 \leq \delta_{\max} < 8$ mm, and finally the most critical class $8 \leq \delta_{\max}$ (class 0). From all the simulations performed, 765 samples resulted in a maximum displacement lower than 7.75 mm (Class 2), 743 samples with maximum displacement between 7.75 mm and 8 mm (Class 1), and 542 samples with maximum displacement higher than 8 mm (Class 0). The results showed that the defects that are close to the impact zone are the most vulnerable and can drastically affect the

behaviour of the part. However, a defect at some distance from the impact zone may not be so critical at low void levels (Figure 6.12a), or may be critical at higher void levels (Figure 6.12b). The classification of displacement levels is not possible with the naked eye, and therefore ML was used as a solution.

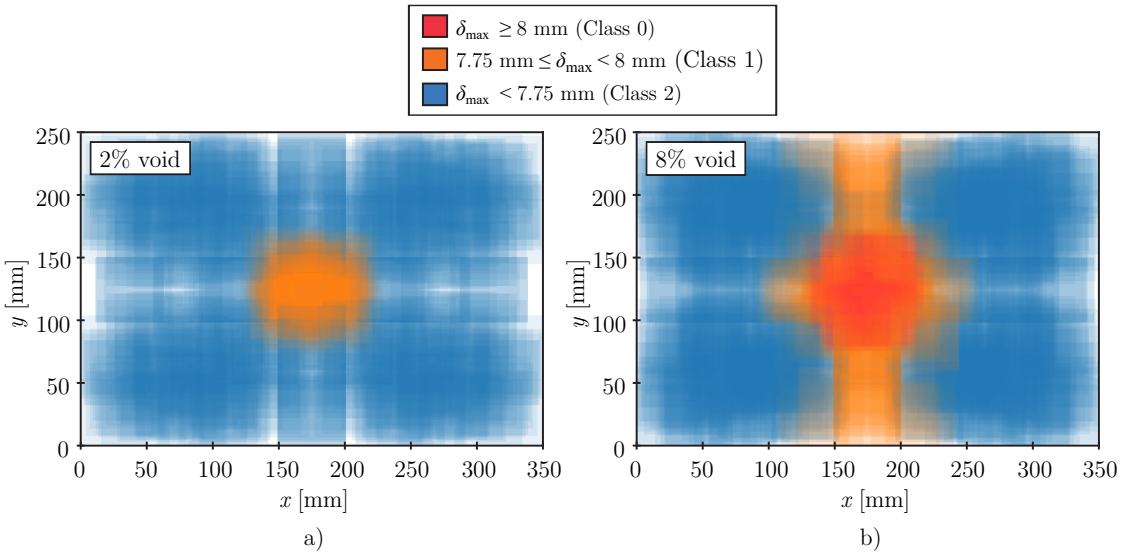

Figure 6.12: Effect of defect location on δ_{max} for a) 2% voids and b) 8% voids.

6.4.2 Data pre-processing

The generated dataset was divided into training and testing dataset, being 80% for training and 20% for testing. The features related to the inputs were the following: defect size, defect position in the x-axis and y-axis and, void content. Three different models are presented and each of them requires a different output. In the classification model, three classes were defined based on maximum displacement. In the single-output regression model, the output was numerical, representing the maximum displacement of the plate. Finally, in the multi-output regression model, force-time, energy-time and displacement-time curves were discretized in 22, 11 and 11 discrete values, respectively.

6.4.3 Model training and evaluation

Random Forest (RF) has been used to train the model [Cutler 2012]. RF is a bagging ensemble method where the outputs of different decision trees (weak learners) are combined to build a much more robust model (strong learner). Due to its good performance, reduced overfitting and good scalability, it has gained a lot of popularity in the last ten years [Raschka 2019]. Moreover, it has been shown to outperform Deep Learning Neural Networks on problems where data come in structured rather than unstructured form (images, texts ...) and data volumes are smaller [Jordan 2015]. In order to obtain competitive performance, hyperparameter tuning is highly recommended.

This can be done manually or by means of optimization techniques. In this case, a powerful hyperparameter optimization technique called grid search was applied. This method searches parametrically for the best combinations of hyperparameters to increase the objective score. The grid of hyperparameters for RF is shown in Table 6.10:

Table 6.10: Hyperparameter grid used for RF model training.

Hyperparameter	Parameter grid
$n\_estimators$	{100, 300, 500, 800, 1200}
Max_depth	{5, 10, 15, 25, 30}
$min\_samples\_split$	{2, 5, 10, 15, 100}
$min\_samples\_leaf$	{1, 2, 5, 10, 15}

For the selection of the model and its hyperparameters, if the test dataset is used, there is a high risk of overfitting. Cross-validation is a robust method that overcomes this risk, splitting the training dataset into training/validation sets used for model selection. To make it more robust, the k-fold technique divides the training dataset into k groups where k-1 are used for training and one fold for validation. This is repeated k times obtaining the mean and deviation of the training scores. In this case, the 5-fold cross-validation technique was used for model training.

Classification model

It is well known that more training samples improve the performance of the ML classification model; however, the trade-off between computational cost and performance is something to be taken into account. For this purpose, the RF classifier model was trained for different training sizes, this being 80% of the total dataset size. The largest data size in this analysis was 2050 samples, i.e. 1640 for training and 410 for testing.

Figure 6.13a shows the results for the 5-fold cross-validation of each of the training sizes. Although it is true that high accuracies were obtained, it is after 1200 training samples when the model obtained an accuracy of over 95% with a low deviation. The hyperparameters that allowed such high results are were Max_depth, $Min\_samples\_leaf$, $Min\_samples\_leaf$ and $N\_estimators$ of 10, 1, 2 and 300, respectively. The optimized model were then tested with the testing dataset and the results are plotted in the following confusion matrix (Figure 6.13b). The test results show an accuracy of 95.8%. It can be seen that the samples of Class 0, were correctly classified in their totality. That is, the model is able to classify perfectly a part with a non-critical defect.

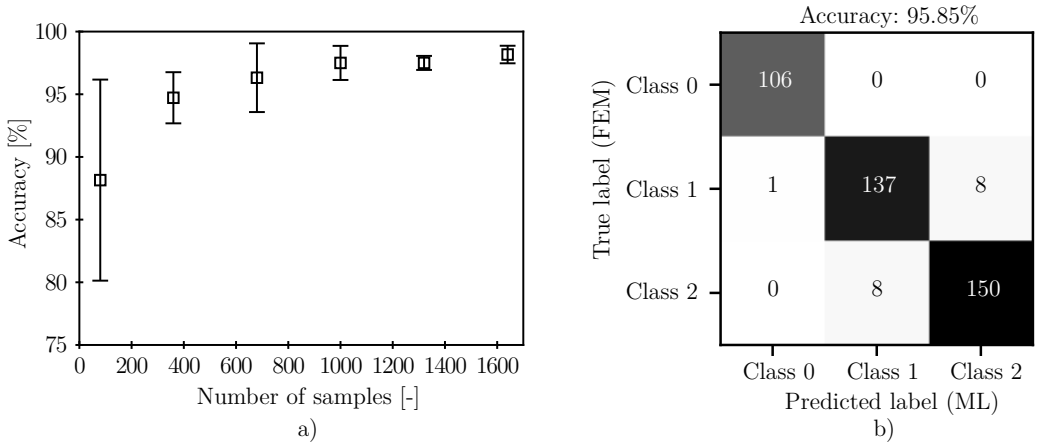

Figure 6.13: Model performance a) Accuracy over training samples and b) ternary confusion matrix.

Single output regression model

The effect of the distance between the defect and the impact zone was found to be crucial in the classification. (Figure 6.14) shows the relationship between the maximum displacement and the distance between the defect and the impactor for each of the three empty cases used in the training. The non-linear trend can be seen in all three cases where at small distances the effect of the void is evident but from 60 mm distance, the effect is negligible.

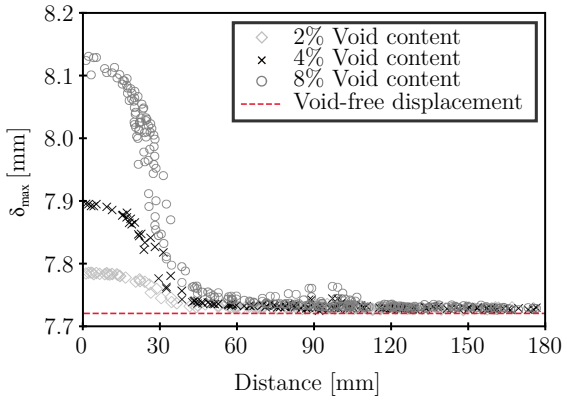

Figure 6.14: $\delta_{\max}$ depending on the distance of the defect for different levels of voids.

In addition to being able to classify plates based on their $\delta_{\max}$, a regression model was generated that directly predicted $\delta_{\max}$. The modelling was similar to that performed in the classifier model. The metric used in the regression case was the R^2 and an accurate value of $R^2 = 0.99$ was obtained in the testing samples (Figure 6.15). In the test samples, the void values were equal to the used in the training, i.e. 2%, 4% and 8% voids. However,

the model should be able to respond to any level of voids, and therefore, the model was re-tested with additional 15 new cases where the level of voids varied randomly between 1% and 10%. In the case of the samples used for the re-testing, the prediction was slightly worse but still higher than $R^2 = 0.85$. This confirms that the ML model is able to predict δ_{max} for void levels between 0% and 10%.

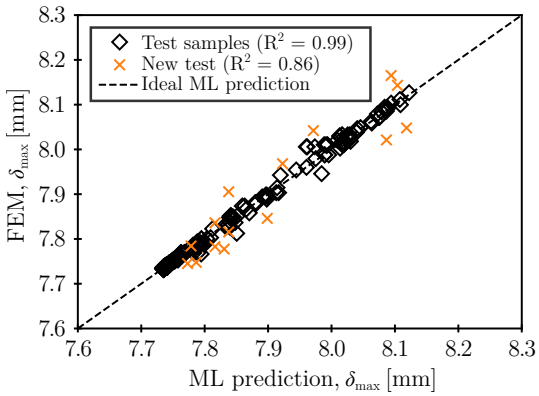

Figure 6.15: The results predicted by the ML model versus the actual results calculated by FEM.

Multi-output regression model

For the multi-output regression, the force-time, energy-time and displacement-time curves were discretised and each variable was independently predicted. To quantify the performance, the R^2 of each of the three variables was calculated separately and the R^2 results boxplot are shown in Figure 6.16. The central line inside the box represents the median of R^2 being superior to 0.995 in all the cases. The boxplot is a visual method used to represent the statistical features of a distribution where the central line represents the median, the box plots the first and third quartiles and the upper and lower lines shows the minimum and maximum values without taking into account the outliers. The lower horizontal line of the box shows the value of the first quartile and the upper horizontal line is the value of the third quartile. Finally, the line at the lower end represents the minimum R^2 value obtained while the upper one represents the maximum. The result obtained is very satisfactory, as shown by the fact that the boxplot is above 0.99 in all three cases.

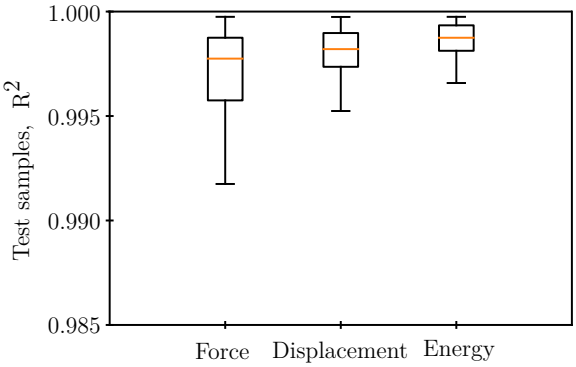

Figure 6.16: R^2 results for force, displacement and energy curves.

In order to analyse the predictions in a more practical way, two case studies were analysed. The non-critical case with a defect far away from the impact zone of a low void content of 2% (Figure 6.17a), and the critical case with a more critical defect of 8% very close to the impact zone (Figure 6.17b).

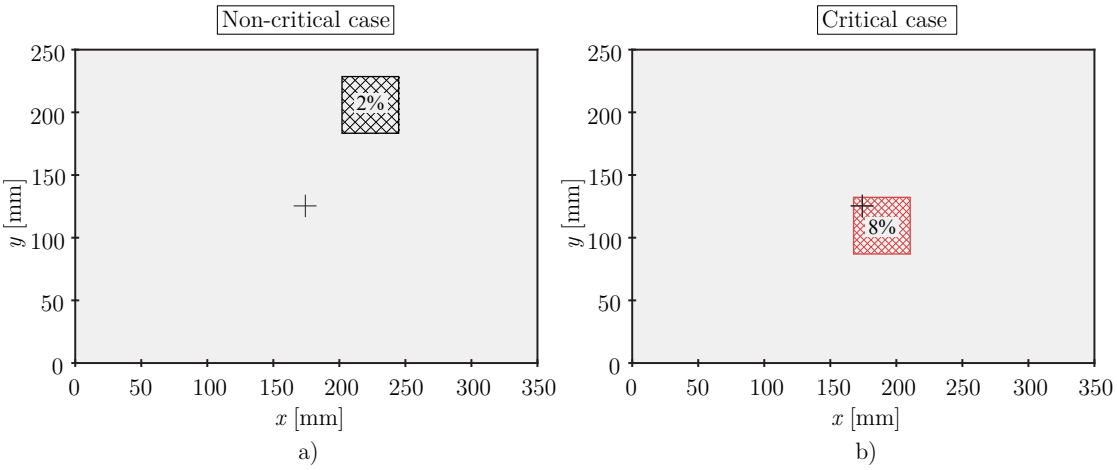

Figure 6.17: The case studies compared: a) a non-critical defect of 2% void and b) a critical defect of 8% void.

The void content map inputs were fed into the predictive model pipeline and all discrete values of the three curves (f-t, U-t and E-t) were predicted. The results obtained by the predictive model represented with a high level of accuracy the curves obtained by FEM (Figure 6.18). By comparing the two extreme case studies, one with a minimal defect and one with a critical defect, it was intended to demonstrate that the model was not biased and that it was able to detect both bad and good parts.

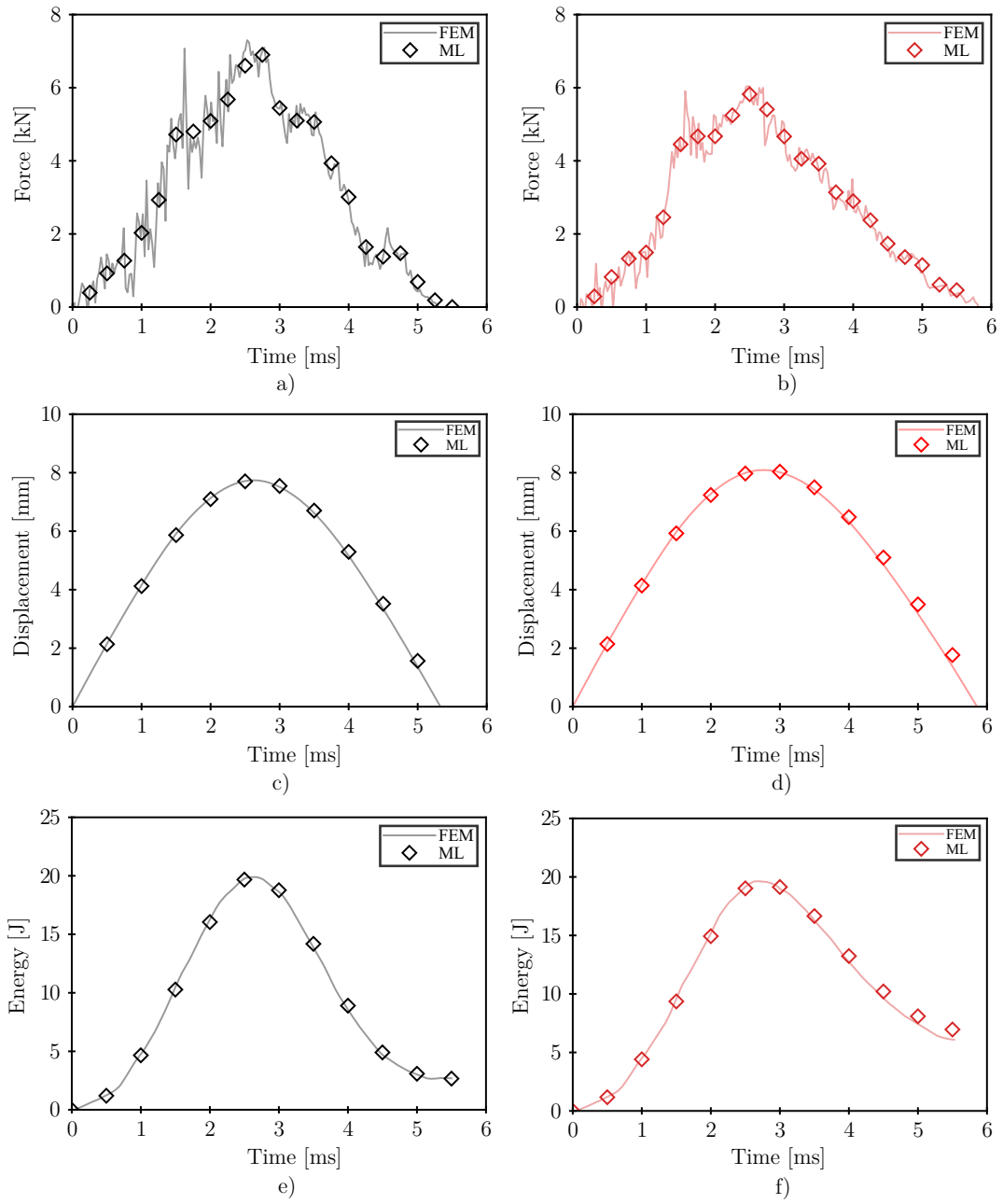

Figure 6.18: FEM results vs ML predictions of the noncritical (black) and critical (red) cases for a-b) $F(t)$, c-d) $\delta(t)$, and e-f) $E(t)$ curves.

The computational cost of this multi-output model can be segmented into three main phases. The first was the generation of the data volume, the accuracy of the predictive model depended on the data volume. Therefore, this phase was crucial and once the data was generated it was not necessary to generate it again. Second, The cost associated with training, and in this case, the model took 5-6 minutes to train. After training, the model was ready to predict and the prediction time was less than 5 seconds. It is worth bearing in mind that the training phase comes before any prediction,

so once trained the model is ready to use it.

6.5 Conclusions

In this chapter, different surrogate models were developed for the structural performance of NCF-carbon reinforced composite plates. These models, once generated and trained, can be used during the manufacturing process to predict the mechanical behaviour of the plate being manufactured.

The case study was a rectangular part subjected to a drop weight impact test. In addition, the part microstructure, related to void content, was introduced as an input variable in order to create the link between the process and structural performance. 2050 simulations were created were the level of void content, 2%, 4% and 8%, and location of the defect were parametrised. For the ML based surrogate models generation, three strategies were followed: Maximum displacement based classification, Maximum displacement regression and, multi-output regression for force-time, displacement-time and energy-time performance curves.

In the case of the classification, it was shown how the void content level and defect position affect to the overall performance. The classification model was based on Random Forest ensemble method and showed an accuracy over 95%. It was observed that the larger the volume of data used, the better the model was better generalising and the better the predictions were made. However, from 1200 samples onwards, the model did not improve its performance and reached its maximum.

For the maximum displacement regression, Random Forest was used and its R^2 score was 0.99. However, this score was obtained with testing samples, which had the same level of void content as the training ones (2%, 4% and, 8%). For evaluating its performance for different void levels, 15 new samples were used for re-testing. In that case, the void level was random and it ranged from 1% to 12%. The results were worse but the R^2 score was over 0.85 and showed that even when using voids levels not used for training the model responds accurately.

In the last case, the multi-output regression model showed a median value higher than 0.995 for the force-time, displacement-time and energy-time curves. The multi-output regression model was able to predict accurately the test curves for critical defects as well as for non-critical defects. The shown method offers a computational cost advantage over the classical FEM model, as it can predict the mechanical response of the part with high accuracy in less than 5 seconds. The use of ML-based surrogate models for composite behaviour modelling has been validated and it is confirmed the potential of using them during the process for on-line structural validation.

7 General conclusions and future lines

Contents

This chapter presents the general conclusions of the thesis, as well as, the future lines of study considered worthy of interest. Finally, the scientific contributions resulting from the results obtained in this work are listed.

7.1 General conclusions

The development of this doctoral thesis has meant a considerable advance for its use in the manufacture of composite components with RTM. The conclusions of the work are described in terms of the objectives stated:

- **Objective I:** *Experimental study of the effect of RTM process parameters on void generation and the effect of those voids on impact properties.*

  Experimentally, following the PSPP approach, the effect of the RTM process parameters on the generation of voids (Process-Structure), and then the effect of these voids on the impact properties (Structure-Property) were quantified. It can be concluded that manufacturing parameters in RTM have a significant effect on void formation and, as a result, on the composite impact properties. The peak force was reduced by 25.9% and the dissipated energy by 9.57% when the void content was increased to 4.3%. Furthermore, in the high void content plates, the

perforation limit was 20% lower. This could be due to the fact that voids have a negative effect on matrix-dominated properties. As shown in the literature, the onset and propagation of delamination is enhanced in the presence of voids, and this is a common failure mechanism in impacts. Furthermore, the existence of voids can precipitate the degradation of the intra-laminar matrix. All of these factors indicate that the fibre load is higher and so breaks prematurely, resulting in reduced peak forces and energy dissipation.

In addition, process optimisation proved to be key in the reduction of voids. Flow front control based on capillary number and vent application resulted in the lowest void content (less than 1%), and hence improved impact properties.

- **Objective II:** *Development and validation of a methodology for diagnosing the quality of composite parts manufactured by RTM.*

  Training the predictive SL models with the synthetic dataset proved to be an efficient method to achieve an accurate diagnosis of the impregnation quality based on process information (Process-Structure).

  Although the present case study was focused on permeability variation due to local binder content, the methodology can be extended to any other source of permeability variation, such as different level of fibre compaction, nesting effect, shear or others. Besides, using the predictive model made it possible to determine the number and location of pressure sensors in the mould, while it can be sufficiently fast for integration into the actual process between the injection and curing stages.

  In this way, after the injection phase, the DT would be able to inform about the current state of the part. Allowing it to be rejected once it has reached sufficient rigidity and without the need to wait for full curing. This allows for a substantial improvement in time and energy savings to improve the robustness of the RTM process.

- **Objective III:** *Development of a ML-based surrogate model of impact event which takes into account manufacturing defects.*

  It was demostrated that the void defect can be included in structural impact models (Structure-Property), and hence, as-manufactured structural surrogate model can be generated (Property-Performance). The surrogated model was developed using synthetic data generated by Abaqus®, where in a innovative way based on property reduction, the void defect was introduced. For the surrogate model, Random Forest was employed for classification based on maximum displacement, maximum displacement regression, and multi-output regression. For the classification problem an accuracy of 95 % was achieved, and for the single output and multi-output regression an R^2 of 0.99 in both cases.

The surrogated models shown a computational cost advantage over the classical FEM model, as it can accurately predict the mechanical impact response of the part in less than 5 seconds. In this way it was confirmed the potential of using them during the process for on-line structural validation. Therefore, during the manufacturing process, the DT will inform about the state of the part as well as a future prediction of its impact behaviour.

7.2 Future lines

The following lines of work are proposed for the coming years based on the knowledge acquired to date.

In order to generate a full PSPP-based DT, the predictive models described in Chapter 5 (Process-Structure) and Chapter 6 (Structure-Property-Performance) must be linked. As a result, the DT will have all of the information and will be able to predict the structure, mechanical properties, and impact behavior based on the process information (Figure 7.1).

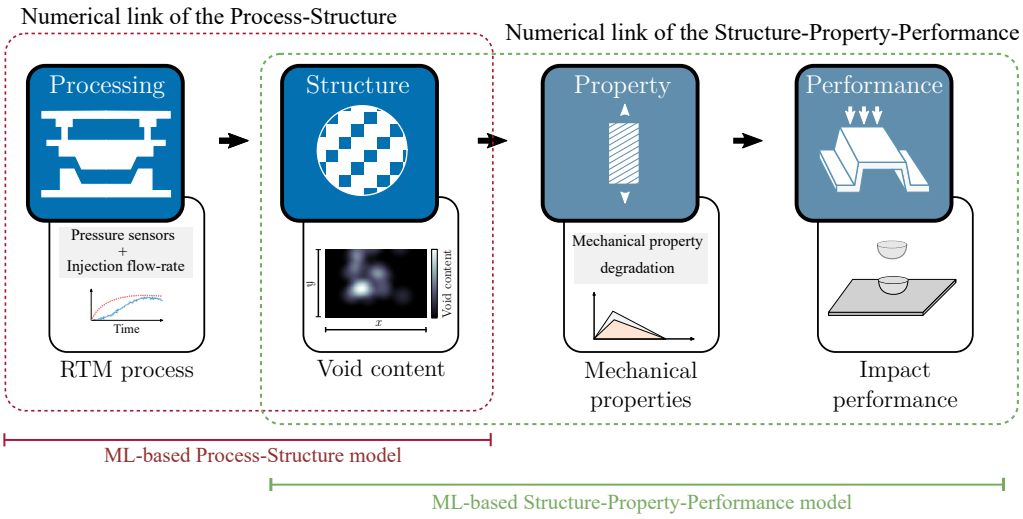

Figure 7.1: Generation of link for the PSPP chain.

However, the design of both models has limited this connection between models to be natural. Firstly, the Process-Structure model predicts the structural quality of the part and even the quality of the defined zones. Nevertheless, in order to make the link with the second predictive model Structure-Property-Performance, a numerical input would be more interesting. In other words, it would be better to know the void level in each of the zones. Some preliminary results were done, where the output was the level of voids in each zone (regression). The used model was Random Forest, which showed good results previously. As shown in Figure 7.2, the range of defects was between 0% and 3% void content. Although the velocity optimiser allowed the overall void level of the part to be

reduced, high void levels were generated in certain zones. The preliminary model achieved an R^2 of 0.72 in the prediction of the level of voids by zones (Figure 7.2a), in addition, the prediction error was on average less than 0.4% in all zones (Figure 7.2b).

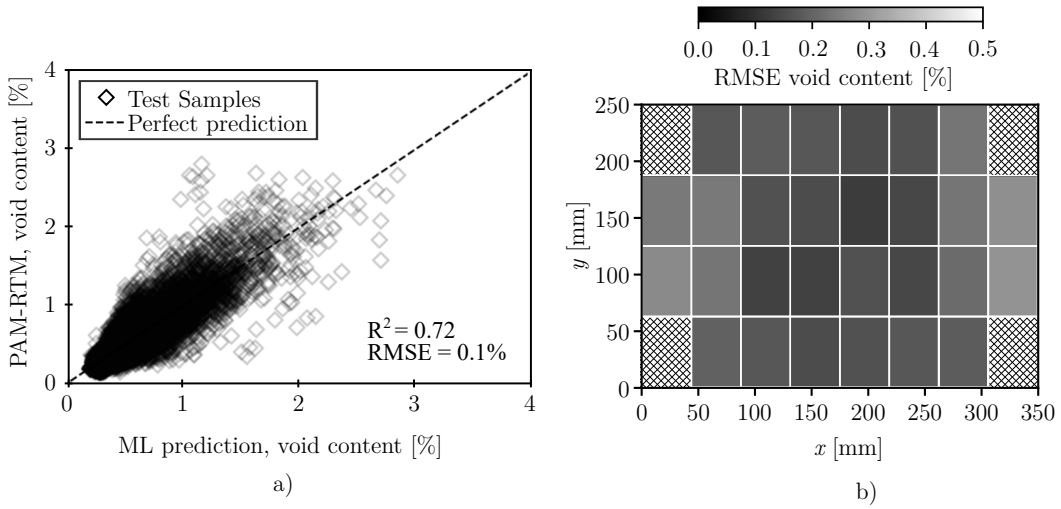

Figure 7.2: Void content prediction by zones a) Regression results and, b) RMSE void content.

The predictive model for mechanical performance (Process-Structure-Property) was able to predict the impact performance of the plates as a function of different local defects. However, the model was trained with local defects (50 mm × 50 mm) and it did not allow input data for each of the zones. Therefore, to verify the future viability of the method, a small adjustment was made to adapt the training data and obtain the defective level in each zone. Figure 7.3 shows the adjustment from a 50 mm × 50 mm local defects to a void map segmented in 32 zones.

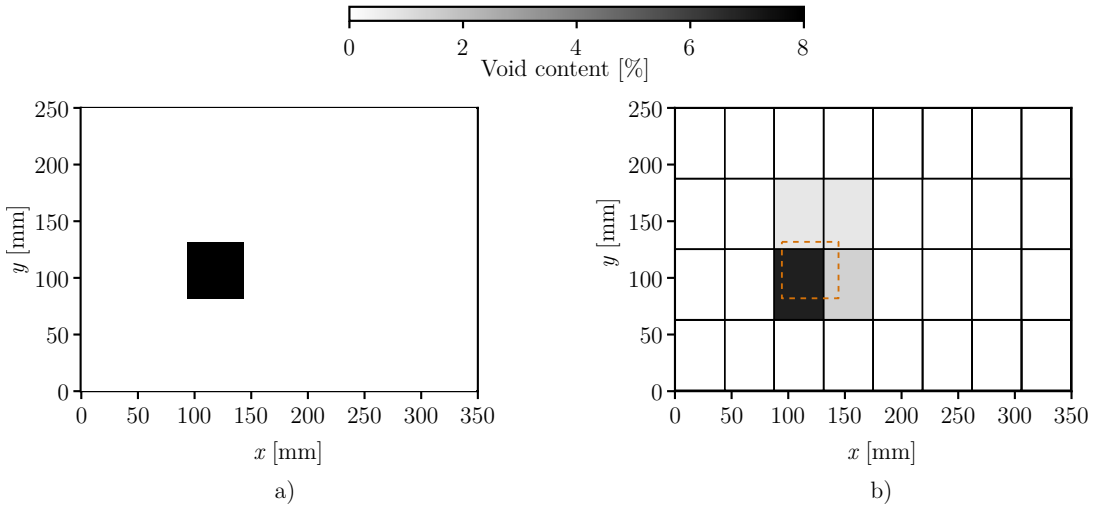

Figure 7.3: Adjustment from a) from a 50 mm × 50 mm local defects to b) void map segmented in 32 zones.

In this new format, the model was re-trained and the results were somewhat worse but still the R2 was 0.94 (Figure 7.4).

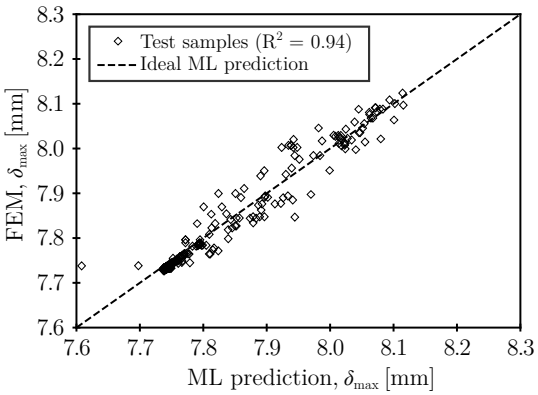

Figure 7.4: The results predicted by the ML and FEM, with zone-based defects.

It can be concluded that in order to give continuity to the work done, the following steps would be interesting:

- Generate a larger volume of process data. Where optimised and non-optimised injections are combined, different injection strategies, different material properties...
- Perform a more exhaustive study to compare the different supervised regression models. As well as, study plates with different zone segmentations (more zones or less zones) or diferent part geometries.
- Based on the results obtained in the process model, generate impact simulations to train the new Structure-Process-Performance predictive model. In addition compare different algorithms and hyperparameters to find the most suitable one.

7.3 Scientific contributions

Within the framework of this doctoral thesis, the following scientific contributions have been made:

7.3.1 Indexed articles

- Mendikute J., Plazaola J., Baskaran M., Zugasti E., Aretxabaleta L., Aurrekoetxea J. (2021). Impregnation quality diagnosis in resin transfer moulding by machine learning. Composites Part B: Engineering, doi: 10.1016/j.compositesb.2021.108973

- Mendikute J., Baskaran M., Aretxabaleta L., Aurrekoetxea J. (2022). Effect of voids on the impact properties of Non-Crimp Fabric Carbon/Epoxy laminates manufactured by Liquid Composite Moulding. Composites Structures. (Major revision)

- Mendikute J., Baskaran M., Llavori I., Zugasti E., Aretxabaleta L., Aurrekoetxea J. (2022). Machine Learning based surrogate modelling for low-velocity impact prediction considering void defects induced in Liquid Composite Moulding process. (Under Review)

7.3.2 Scientific conferences

- Mendikute J., Baskaran M., Aretxabaleta L., Aurrekoetxea J. (2019). Reducción de porosidad en RTM mediante el control de la velocidad del frente de flujo. XII Congreso Nacional de Materiales Compuestos (MATCOMP19), Vigo 2019.

References

[Abrate 1991] Abrate, Serge (1991). "Impact on laminated composite materials". In: *Applied Mechanics Reviews*. DOI: 10.1115/1.3119500.

[Advani 2010] Advani, Suresh G. and E. Murat Sozer (2010). *Process Modeling of composite manufature*. 2nd. CRC Press.

[Afazov 2021] Afazov, Shukri, Adam Roberts, Louise Wright, Prashant Jadhav, Adam Holloway, Hector Basoalto, Katy Milne, and Nick Brierley (2021). "Metal powder bed fusion process chains: an overview of modelling techniques". In: *Progress in Additive Manufacturing* 0123456789. DOI: 10.1007/s40964-021-00230-1.

[Aggelis 2012] Aggelis, D. G. and A. S. Paipetis (2012). "Monitoring of resin curing and hardening by ultrasound". In: *Construction and Building Materials*. DOI: 10.1016/j.conbuildmat.2011.06.084.

[Agrawal 2016] Agrawal, Ankit and Alok Choudhary (2016). "Perspective: Materials informatics and big data: Realization of the "fourth paradigm" of science in materials science". In: *APL Materials* 4.5. DOI: 10.1063/1.4946894.

[Aleksendrić 2015] Aleksendrić, Dragan and Pierpaolo Carlone (2015). "Composite materials – modelling, prediction and optimization". In: *Soft Computing in the Design and Manufacturing of Composite Materials*, pp. 61–289. DOI: 10.1533/9781782421801.61.

[Allison 2006] Allison, John, Mei Li, C. Wolverton, and Xu Ming Su (2006). *Virtual aluminum castings: An industrial application of ICME*. DOI: 10.1007/s11837-006-0224-4.

[Alpaydin 2010] Alpaydin, Ethem (2010). *Introduction to Machine Learng Second Edition*.

[Arthurs 2015] Arthurs, B., D. J. Bull, V. Arumugam, A. R. Chambers, and C. Santulli (2015). "Porosity effect on residual flexural strength following low energy impact of carbon fibre composites". In: *Polymers and Polymer Composites*. DOI: 10.1177/096739111502300401.

[Asp 1997] Asp, Leif E. and Fredrik Brandt (1997). "Effects of pores and voids on the interlaminar delamination toughness of a carbon/epoxy composite". In: *International Conference on Composite Materials, ICCM-11, Gold Coast, Australia*.

[Aurrekoetxea 2012] Aurrekoetxea, J., A. Agirregomezkorta, G. Aretxaga, and M. Sarrionandia (2012). "Impact behavior of carbon fiber/epoxy composite manufactured by vacuum-assisted compression resin transfer molding". In: *Journal of Composite Materials* 46.1, pp. 43–49. DOI: 10.1177/0021998311401938.

[Aymerich 2009] Aymerich, F., F. Dore, and P. Priolo (2009). "Simulation of multiple delaminations in impacted cross-ply laminates using a finite element model based on cohesive interface elements". In: *Composites Science and Technology* 69.11-12, pp. 1699–1709. DOI: 10.1016/j.compscitech.2008.10.025.

[Bárkányi 2021] Bárkányi, Ágnes, Tibor Chován, Sándor Németh, and János Abonyi (2021). "Modelling for digital twins—potential role of surrogate models". In: *Processes* 9.3. DOI: 10.3390/pr9030476.

[Barry 2016] Barry, T. J., M. Kesharaju, C. R. Nagarajah, and S. Palanisamy (2016). *Defect characterisation in laminar composite structures using ultrasonic*

techniques and artificial neural networks. DOI: 10.1177/0021998315584651.

[Baskaran 2017] Baskaran, Maider (2017). "Optimización del proceso de Compression Resin Transfer Moulding (CRTM) mediante técnicas experimentales y simulación". PhD thesis, p. 155.

[Baskaran 2018] Baskaran, Maider, Laurentzi Aretxabaleta, Modesto Mateos, and Jon Aurrekoetxea (2018). "Simulation and experimental validation of the effect of material and processing parameters on the injection stage of compression resin transfer molding". In: *Polymer Composites*. DOI: 10.1002/pc.24514.

[Bel 2015] Bel, S. (2015). "Mechanical behaviour of non-crimp fabric (NCF) preforms in composite materials manufacturing". In: *Advances in Composites Manufacturing and Process Design*. Elsevier Ltd., pp. 253–268. DOI: 10.1016/B978-1-78242-307-2.00012-9.

[Belov 2004] Belov, E. B., S. V. Lomov, Ignaas Verpoest, T. Peters, D. Roose, R. S. Parnas, K. Hoes, and H. Sol (2004). "Modelling of permeability of textile reinforcements: Lattice Boltzmann method". In: *Composites Science and Technology*. DOI: 10.1016/j.compscitech.2003.09.015.

[Bergstra 2011] Bergstra, J, Edwin H Land Boulevard, D Yamins, D D Cox, and Edwin H Land Boulevard (2011). "Making a Science of Model Search : Hyperparameter Optimization in Hundreds of Dimensions for Vision Architectures". In: *Proceedings of the 30th International Conference on Machine Learning*. Vol. 28.

[Bickerton 2001] Bickerton, Simon, Hubert C. Stadtfeld, Karl V. Steiner, and Suresh G. Advani (2001). "Design and application of actively controlled injection schemes for resin-transfer molding". In: *Composites Science and Technology*. DOI: 10.1016/S0266-3538(01)00064-1.

[BMW group 2021] BMW group (2021). *BMW iX chassis*.

[Bodaghi 2019a] Bodaghi, M., Ricardo Costa, Rui Gomes, João Silva, Nuno Correia, and Fernando Silva (2019a). "Experimental comparative study of the variants of high-temperature vacuum-assisted resin transfer moulding". In: *Composites Part A: Applied Science and Manufacturing* 129, p. 105708. DOI: 10.1016/j.compositesa.2019.105708.

[Bodaghi 2016] Bodaghi, M., C. Cristóvão, R. Gomes, and N. C. Correia (2016). "Experimental characterization of voids in high fibre volume fraction composites processed by high injection pressure RTM". In: *Composites Part A: Applied Science and Manufacturing* 82, pp. 88–99. DOI: 10.1016/j.compositesa.2015.11.042.

[Bodaghi 2019b] Bodaghi, M., Lomov, P. Simacek, N. C. Correia, and S. G. Advani (2019b). "On the variability of permeability induced by reinforcement distortions and dual scale flow in liquid composite moulding: A review". In: *Composites Part A: Applied Science and Manufacturing* 120, pp. 188–210. DOI: 10.1016/j.compositesa.2019.03.004.

[Bodaghi 2019c] Bodaghi, M., P. Simacek, N. Correia, and S. Advani (2019c). "Experimental parametric study of flow-induced fiber washout during high-injection-pressure resin transfer molding". In: *Polymer Composites* September, pp. 1–13. DOI: 10.1002/pc.25437.

[Bogenfeld 2018] Bogenfeld, Raffael, Janko Kreikemeier, and Tobias Wille (2018). "Review and benchmark study on the analysis of low-velocity impact on composite laminates". In: *Engineering Failure Analysis* 86.December 2017, pp. 72–99. DOI: 10.1016/j.engfailanal.2017.12.019.

[Bowles 1992] Bowles, Kenneth J. and Stephen Frimpong (1992). "Void Effects on the Interlaminar Shear Strength of Unidirectional Graphite-Fiber-Reinforced Composites". In: *Journal of Composite Materials*. DOI: 10.1177/002199839202601006.

[Bradley 1997] Bradley, Andrew P. (1997). "The use of the area under the ROC curve in the evaluation of machine learning algorithms". In: *Pattern Recognition* 30.7, pp. 1145–1159. DOI: 10.1016/S0031-3203(96)00142-2.

[Bréard 2003] Bréard, Joël, Yann Henzel, François Trochu, and Raymond Gauvin (2003). "Analysis of dynamic flows through porous media. Part I: Comparison between saturated and unsaturated flows in fibrous reinforcements". In: *Polymer Composites*. DOI: 10.1002/pc.10038.

[Camanho 2002] Camanho, P. and C. Davila (2002). "Mixed-Mode Decohesion Finite Elements for the Simulation of Delamination in Composite Materials". In: *NASA Technical Paper* 211737.June, p. 42.

[Camanho 2003] Camanho, P., C. Davila, and D. Moura (2003). "Numerical Simulation of Mixed-Mode Progressive Delamination in Composite Materials Damage and Failure of Non-Conventional Composite Laminates View project". In: *Journal of Composite Materials* 37.16, pp. 1415–1438. DOI: 10.1177/0021998303034505.

[Carlone 2015] Carlone, P. and G. S. Palazzo (2015). "Unsaturated and Saturated Flow Front Tracking in Liquid Composite Molding Processes using Dielectric Sensors". In: *Applied Composite Materials*. DOI: 10.1007/s10443-014-9422-3.

[Carraro 2015a] Carraro, P. A., L. Maragoni, and M. Quaresimin (2015a). "Influence of manufacturing induced defects on damage initiation and propagation in carbon/epoxy NCF laminates". In: *Advanced Manufacturing: Polymer and Composites Science*. DOI: 10.1179/2055035914Y.0000000004.

[Carraro 2015b] Carraro, P. A., L. Maragoni, and M. Quaresimin (2015b). "Influence of manufacturing induced defects on damage initiation and propagation in carbon/epoxy NCF laminates". In: *Advanced Manufacturing: Polymer and Composites Science* 1.1, pp. 44–53. DOI: 10.1179/2055035914Y.0000000004.

[Cartié 2002] Cartié, D. D.R. and P. E. Irving (2002). "Effect of resin and fibre properties on impact and compression after impact performance of CFRP". In: *Composites - Part A: Applied Science and Manufacturing*. DOI: 10.1016/S1359-835X(01)00141-5.

[Castro 2020] Castro, J., F. Sket, and C. González (2020). "S-XCT experimental determination of local contact angle and meniscus shape in liquid moulding of composites". In: *Composites Science and Technology* 199.April, p. 108362. DOI: 10.1016/j.compscitech.2020.108362.

[C. T. Chen 2019] Chen, Chun Teh and Grace X. Gu (2019). "Machine learning for composite materials". In: *MRS Communications* 9.2, pp. 556–566. DOI: 10.1557/mrc.2019.32.

[T. Chen 2016] Chen, Tianqi and Carlos Guestrin (2016). "XGBoost: A scalable tree boosting system". In: *Proceedings of the ACM SIGKDD International Conference on Knowledge Discovery and Data Mining*. DOI: 10.1145/2939672.2939785.

[X. Chen 2012] Chen, Xingkai, Bingyan Jiang, and Zhou Zhou (2012). "Optimization of CFRP pultrusion process with NSGA-II and ANN". In: *Advanced Materials Research* 538-541, pp. 2705–2711. DOI: 10.4028/www.scientific.net/AMR.538-541.2705.

[X. Chen 2010] Chen, Xingkai, Huaiqin Xie, Hui Chen, and Fuhua Zhang (2010). "Optimization for CFRP pultrusion process based on genetic algorithm-neural network". In: *International Journal of Material Forming* 3.SUPPL. 2, pp. 1391–1399. DOI: 10.1007/s12289-010-0684-5.

[Chiu 2002] Chiu, C. H. and C. C. Cheng (2002). "In-plane permeability of stitched MMWK laminates in resin transfer molding". In: *Journal of Reinforced Plastics and Composites*. DOI: 10.1177/0731684402021005440.

[Chowdhury 2008] Chowdhury, K. A., R. Talreja, and A. A. Benzerga (2008). "Effects of manufacturing-induced voids on local failure in polymer-based composites". In: *Journal of Engineering Materials and Technology, Transactions of the ASME*. DOI: 10.1115/1.2841529.

[Christoforou 1998] Christoforou, A. P. and A. S. Yigit (1998). "Effect of flexibility on low velocity impact response". In: *Journal of Sound and Vibration*. DOI: 10.1006/jsvi.1998.1807.

[Cinquin 2007] Cinquin, Jacques, Virginie Triquenaux, and Yvan Rouesne (2007). "Porosity influence on organic composite material mechanical properties". In: *ICCM International Conferences on Composite Materials*.

[Crane 2018] Crane, Robert L. (2018). "Nondestructive inspection of composites". In: *Comprehensive Composite Materials II*. Vol. 7-8. April 2015, pp. 159–166. DOI: 10.1016/B978-0-12-803581-8.03925-4.

[Cuevas 2013] Cuevas, Esmeralda, Covadonga García, Sergio Hernandez, Tomás Enrique Gomez Álvarez-Arenas, and Mar Cañada (2013). "Non destructive testing for non cured composites: Air coupled Ultrasounds and Thermography". In: *5th International Symposium on NDT in Aerospace*.

[Cutler 2012] Cutler, Adele, D. Richard Cutler, and John R. Stevens (2012). "Random forests". In: *Ensemble Machine Learning: Methods and Applications*. DOI: 10.1007/9781441993267{_}5.

[Dassault Systèmes 2021] Dassault Systèmes (2021). *Abaqus Unified FEA - SIMULIA™ by Dassault Systèmes®*.

[David-West 2008] David-West, O. S., D. H. Nash, and W. M. Banks (2008). "An experimental study of damage accumulation in balanced CFRP laminates due to repeated impact". In: *Composite Structures* 83.3, pp. 247–258. DOI: 10.1016/j.compstruct.2007.04.015.

[Dávila 2005] Dávila, Carlos G., Pedro P. Camanho, and Cheryl A. Rose (2005). "Failure criteria for FRP laminates". In: *Journal of Composite Materials* 39.4, pp. 323–345. DOI: 10.1177/0021998305046452.

[Dávila 2003] Dávila, Carlos G., Navin Jaunky, and Sanjib Goswami (2003). "Failure criteria for FRP laminates in plane stress". In: *Collection of Technical Papers - AIAA/ASME/ASCE/AHS/ASC Structures, Structural Dynamics and Materials Conference*.

[Demaría 2007] Demaría, C., Edu Ruiz, and F. Trochu (2007). "In-plane anisotropic permeability characterization of deformed woven fabrics by unidirectional injection. Part I: Experimental results". In: *Polymer Composites*. DOI: 10.1002/pc.20107.

[Devillard 2003] Devillard, Mathieu, Kuang Ting Hsiao, Ali Gokce, and Suresh G. Advani (2003). "On-line characterization of bulk permeability and race-tracking during the filling stage in resin transfer molding process". In: *Journal of Composite Materials*. DOI: 10.1177/0021998303034459.

[Di Fratta 2013] Di Fratta, Claudio, Florian Klunker, and Paolo Ermanni (2013). "A methodology for flow-front estimation in LCM processes based on pressure sensors". In: *Composites Part A: Applied Science and Manufacturing* 47.1, pp. 1–11. DOI: 10.1016/j.compositesa.2012.11.008.

[Di Fratta 2016] Di Fratta, Claudio, Grigorios Koutsoukis, Florian Klunker, and Paolo Ermanni (2016). "Fast method to monitor the flow front and control injection parameters in resin transfer molding using pressure sensors". In: *Journal of Composite Materials* 50.21, pp. 2941–2957. DOI: 10.1177/0021998315614994.

[Di Landro 2017] Di Landro, Luca, Aurelio Montalto, Paolo Bettini, Stefania Guerra, Fabrizio Montagnoli, and Marco Rigamonti (2017). "Detection of voids in carbon/epoxy laminates and their influence on mechanical properties". In: *Polymers and Polymer Composites*. DOI: 10.1177/096739111702500506.

[Dickert 2012] Dickert, Matthias, David C. Berg, and Gerhard Ziegmann (2012). "Influence of binder activation and fabric design on the permeability of non-crimp carbon fabrics". In: *Flow Processes in Composite Materials FPCM-11* June, p. 18.

[Dobyns 1981] Dobyns, A. L. (1981). "Analysis of Simply-Supported Orthotropic Plates Subject to Static and Dynamic Loads". In: *AIAA Journal*. DOI: 10.2514/3.50984.

[Dong 2016] Dong, Chensong (2016). "Effects of Process-Induced Voids on the Properties of Fibre Reinforced Composites". In: *Journal of Materials Science and Technology* 32.7, pp. 597–604. DOI: 10.1016/j.jmst.2016.04.011.

[Drapier 2002] Drapier, S., A. Pagot, A. Vautrin, and P. Henrat (2002). "Influence of the stitching density on the transverse permeability of non-crimped new concept (NC2) multiaxial reinforcements: Measurements and predictions". In: *Composites Science and Technology*. DOI: 10.1016/S0266-3538(02)00127-6.

[Elenchezhian 2018] Elenchezhian, Muthu Ram Prabhu, Aishwarya Nandini, Vamsee Vadlamudi, Rassel Raihan, and Kenneth Reifsnider (2018). "Detection and prediction of defects in composite materials using di-electric characterization and neural networks". In: *International SAMPE Technical Conference*.

[Esnaola 2016] Esnaola, A., B. Elguezabal, J. Aurrekoetxea, I. Gallego, and I. Ulacia (2016). "Optimization of the semi-hexagonal geometry of a composite crush structure by finite element analysis". In: *Composites Part B: Engineering* 93, pp. 56–66. DOI: 10.1016/j.compositesb.2016.03.002.

[Estrada 2002] Estrada, Gonzalo, Céline Vieux-Pernon, and Suresh G. Advani (2002). "Experimental characterization of the influence of tackifier material on preform permeability". In: *Journal of Composite Materials* 36.19, pp. 2297–2310. DOI: 10.1177/0021998302036019542.

[Fang 2015] Fang, Liangchao, Jianjun Jiang, Junbiao Wang, and Chao Deng (2015). "Effect of Nesting on the Out-of-Plane Permeability of Unidirectional Fabrics in Resin Transfer Molding". In: *Applied Composite Materials*. DOI: 10.1007/s10443-014-9403-6.

[Fauster 2019] Fauster, Ewald, David C. Berg, Dilmurat Abliz, Harald Grössing, Dieter Meiners, Gerhard Ziegmann, and Ralf Schledjewski (2019). "Image processing and data evaluation algorithms for reproducible optical in-plane permeability characterization by radial flow experiments". In: *Journal of Composite Materials*. DOI: 10.1177/0021998318780209.

[Feraboli 2004] Feraboli, Paolo and Keith T. Kedward (2004). "Enhanced evaluation of the low-velocity impact response of composite plates". In: *AIAA Journal* 42.10, pp. 2143–2152. DOI: 10.2514/1.4534.

[Feraboli 2006] Feraboli, Paolo and Keith T. Kedward (2006). "A new composite structure impact performance assessment program". In: *Composites Science and Technology* 66.10, pp. 1336–1347. DOI: 10.1016/j.compscitech.2005.09.009.

[Garschke 2012] Garschke, C., C. Weimer, P. P. Parlevliet, and B. L. Fox (2012). "Out-of-autoclave cure cycle study of a resin film infusion process using in situ process monitoring". In: *Composites Part A: Applied Science and Manufacturing*. DOI: 10.1016/j.compositesa.2012.01.003.

[Ghiorse 1993] Ghiorse, S. R. (1993). "Effect of void content on the mechanical properties of carbon/epoxy laminates". In: *S.A.M.P.E. quarterly*.

[Glaessgen 2012] Glaessgen, E. H. and D. S. Stargel (2012). "The digital twin paradigm for future NASA and U.S. Air force vehicles". In: *Collection of Technical Papers - AIAA/ASME/ASCE/AHS/ASC Structures, Structural Dynamics and Materials Conference*. DOI: 10.2514/6.2012-1818.

[Gokce 2005] Gokce, Ali and Suresh G. Advani (2005). "Modeling, optimization and control of resin flow during manufacturing of textile composites with liquid molding". In: *Design and Manufacture of Textile Composites*, pp. 242–291. DOI: 10.1533/9781845690823.242.

[Gomez 2021] Gomez, C., A. Guardia, J. L. Mantari, A. M. Coronado, and J. N. Reddy (2021). "A contemporary approach to the MSE paradigm powered by Artificial Intelligence from a review focused on Polymer Matrix Composites". In: *Mechanics of Advanced Materials and Structures* 0.0, pp. 1–21. DOI: 10.1080/15376494.2021.1886379.

[González 2020] González, C. and J. Fernández-León (2020). "A Machine Learning Model to Detect Flow Disturbances during Manufacturing of Composites by Liquid Moulding". In: *Journal of Composites Science* 4.2, p. 71. DOI: 10.3390/jcs4020071.

[González 2017] González, C., J. J. Vilatela, J. M. Molina-Aldareguía, C. S. Lopes, and J. LLorca (2017). "Structural composites for multifunctional applications: Current challenges and future trends". In: *Progress in Materials Science* 89, pp. 194–251. DOI: 10.1016/j.pmatsci.2017.04.005.

[Gourichon 2008] Gourichon, Boris, Mylène Deléglise, Christophe Binetruy, and Patricia Krawczak (2008). "Dynamic void content prediction during radial injection in liquid composite molding". In: *Composites Part A: Applied Science and Manufacturing* 39.1, pp. 46–55. DOI: 10.1016/j.compositesa.2007.09.008.

[Greve 2006] Greve, L. and A. K. Pickett (2006). "Modelling damage and failure in carbon/epoxy non-crimp fabric composites including effects of fabric pre-shear". In: *Composites Part A: Applied Science and Manufacturing* 37.11, pp. 1983–2001. DOI: 10.1016/j.compositesa.2005.12.012.

[Griffin 2017] Griffin, Daniel, Alper Aktas, Maria Lodeiro, Tim Young, Ian Hamerton, and Ivana Partridge (2017). "A comparison of material state monitoring techniques applied to resin transfer moulding". In: *ICCM International Conferences on Composite Materials*.

[Gu 2018] Gu, Grace X., Chun Teh Chen, and Markus J. Buehler (2018). "De novo composite design based on machine learning algorithm". In: *Extreme Mechanics Letters* 18, pp. 19–28. DOI: 10.1016/j.eml.2017.10.001.

[Guerdal 1991] Guerdal, Z., A. P. Tomasino, and S. B. Biggers (1991). "Effects of processing induced defects on laminate response. Interlaminar tensile strength". In: *SAMPE Journal*.

[Hallett 2008] Hallett, S. (2008). "Predicting progressive delamination via interface elements". In: *Delamination Behaviour of Composites*, pp. 367–386. DOI: 10.1533/9781845694821.4.367.

[Hamidi 2018] Hamidi, Youssef K. and Cengiz M. Altan (2018). *2.5 Process-Induced Defects in Resin Transfer Molded Composites*. Vol. 2. Elsevier Ltd., pp. 95–106. DOI: 10.1016/b978-0-12-803581-8.09902-1.

[Hancox 1977] Hancox, N. L. (1977). "The effects of flaws and voids on the shear properties of CFRP". In: *Journal of Materials Science*. DOI: 10.1007/BF00540969.

[Harper 1987] Harper, B. D., G. H. Staab, and R. S. Chen (1987). "A Note on the Effects of Voids Upon the Hygral and Mechanical Properties of AS4/3502 Graphite/Epoxy". In: *Journal of Composite Materials*. DOI: 10.1177/002199838702100306.

[Hashin 1980] Hashin, Z. (1980). "Failure criteria for unidirectional fiber composites". In: *Journal of Applied Mechanics, Transactions ASME*. DOI: 10.1115/1.3153664.

[Hashin 1973] Hashin, Z. and A. Rotem (1973). "A Fatigue Failure Criterion for Fiber Reinforced Materials". In: *Journal of Composite Materials*. DOI: 10.1177/002199837300700404.

[Hegg 2005] Hegg, Michael C., Anil Ogale, Ann Mescher, Alexander V. Mamishev, and Bob Minaie (2005). "Remote monitoring of resin transfer molding processes by distributed dielectric sensors". In: *Journal of Composite Materials*. DOI: 10.1177/0021998305051083.

[Heieck 2017] Heieck, F., F. Hermann, P. Middendorf, and K. Schladitz (2017). "Influence of the cover factor of 2D biaxial and triaxial braided carbon composites on their in-plane mechanical properties". In: *Composite Structures*. DOI: 10.1016/j.compstruct.2016.12.025.

[Heimbs 2014] Heimbs, S., T. Bergmann, D. Schueler, and N. Toso-PentecÔte (2014). "High velocity impact on preloaded composite plates". In: *Composite Structures*. DOI: 10.1016/j.compstruct.2013.12.031.

[Heinecke 2018] Heinecke, F. and T. Wille (2018). "In-situ structural evaluation during the fibre deposition process of composite manufacturing". In: *CEAS Aeronautical Journal* 9.1, pp. 123–133. DOI: 10.1007/s13272-018-0284-5.

[Henning 2014] Henning, Frank, Alexander Bernath, Raman Chaudhari, Luise Kärger, Dino Magagnato, and Fabian Schirmaier (2014). "An integrated development approach to combine design, manufacturing and validation of high-pressure rtm composite structures". In: *International SAMPE Technical Conference*.

[Henning 2019] Henning, Frank, Luise Kärger, Dominik Dörr, Fabian J. Schirmaier, Julian Seuffert, and Alexander Bernath (2019). "Fast processing and continuous simulation of automotive structural composite components". In: *Composites Science and Technology* 171.September 2017, pp. 261–279. DOI: 10.1016/j.compscitech.2018.12.007.

[Hernández 2013] Hernández, S., F. Sket, C. González, and J. Llorca (2013). "Optimization of curing cycle in carbon fiber-reinforced laminates: Void distribution and mechanical properties". In: *Composites Science and Technology*. DOI: 10.1016/j.compscitech.2013.06.005.

[Hill 1965] Hill, R. (1965). "Theory of mechanical properties of fibre-strengthened materials-III. self-consistent model". In: *Journal of the Mechanics and Physics of Solids*. DOI: 10.1016/0022-5096(65)90008-6.

[Hoes 2004] Hoes, Kris, Daniela Dinescu, Hugo Sol, Richard S. Parnas, and Stepan Lomov (2004). "Study of nesting induced scatter of permeability values in layered reinforcement fabrics". In: *Composites Part A: Applied Science and Manufacturing*. DOI: 10.1016/j.compositesa.2004.05.004.

[Hoffman 1967] Hoffman, Oscar (1967). "The Brittle Strength of Orthotropic Materials". In: *Journal of Composite Materials*. DOI: 10.1177/002199836700100210.

[Hou 1996] Hou, Meng, Lin Ye, and Yiu Wing Mai (1996). "Effect of moulding temperature on flexure, impact strength and interlaminar fracture toughness of CF/PEI composite". In: *Journal of Reinforced Plastics and Composites*. DOI: 10.1177/073168449601501104.

[hu 2003] hu, Jinlian, Yi Liu, and Xueming Shao (2003). "Effect of Stitches on the Permeability of Interbundle Channels in Stitched Fabrics". In: *Textile Research Journal*. DOI: 10.1177/004051750307300806.

[H. Huang 2005] Huang, Hansong and Ramesh Talreja (2005). "Effects of void geometry on elastic properties of unidirectional fiber reinforced composites". In: *Composites Science and Technology*. DOI: 10.1016/j.compscitech.2005.02.019.

[Z. Huang 2021] Huang, Ziqi, Yang Shen, Jiayi Li, Marcel Fey, and Christian Brecher (2021). "A Survey on AI-Driven Digital Twins in Industry 4.0: Smart Manufacturing and Advanced Robotics". In: pp. 1–35.

[Hürkamp 2020] Hürkamp, André, Sebastian Gellrich, Tim Ossowski, Jan Beuscher, Sebastian Thiede, Christoph Herrmann, and Klaus Dröder (2020). "Combining simulation and machine learning as digital twin for the

manufacturing of overmolded thermoplastic composites". In: *Journal of Manufacturing and Materials Processing* 4.3. DOI: 10.3390/JMMP4030092.

[Im 2021] Im, Sunyoung, Hyungjun Kim, Wonbae Kim, and Maenghyo Cho (2021). "Neural network constitutive model for crystal structures". In: *Computational Mechanics*. DOI: 10.1007/s00466-020-01927-w.

[Jensen 2001] Jensen, Henrik Myhre and Izhak Sheinman (2001). "Straight-sided, buckling-driven delamination of thin films at high stress levels". In: *International Journal of Fracture*. DOI: 10.1023/A:1010821918325.

[Jordan 2015] Jordan, M I and T M Mitchell (2015). *Machine learning: Trends, perspectives, and prospects*. DOI: 10.1126/science.aaa8415.

[Kakakasery 2015] Kakakasery, J., V. Arumugam, K. Abdul Rauf, D. Bull, A. R. Chambers, C. Scarponi, and C. Santulli (2015). "Cure cycle effect on impact resistance under elevated temperatures in carbon prepreg laminates investigated using acoustic emission". In: *Composites Part B: Engineering*. DOI: 10.1016/j.compositesb.2015.02.002.

[Kang 2001] Kang, M. K., W. I. Lee, and H. T. Hahn (2001). "Analysis of vacuum bag resin transfer molding process". In: *Composites - Part A: Applied Science and Manufacturing*. DOI: 10.1016/S1359-835X(01)00012-4.

[Kärger 2015] Kärger, Luise, Alexander Bernath, Florian Fritz, Siegfried Galkin, Dino Magagnato, André Oeckerath, Alexander Schön, and Frank Henning (2015). "Development and validation of a CAE chain for unidirectional fibre reinforced composite components". In: *Composite Structures* 132, pp. 350–358. DOI: 10.1016/j.compstruct.2015.05.047.

[Kärger 2018] Kärger, Luise, Siegfried Galkin, Clemens Zimmerling, Dominik Dörr, Johannes Linden, André Oeckerath, and Klaus Wolf (2018). "Forming optimisation embedded in a CAE chain to assess and enhance the structural performance of composite components". In: *Composite Structures* 192.February, pp. 143–152. DOI: 10.1016/j.compstruct.2018.02.041.

[Ke 2017] Ke, Guolin, Qi Meng, Thomas Finley, Taifeng Wang, Wei Chen, Weidong Ma, Qiwei Ye, and Tie Yan Liu (2017). "LightGBM: A highly efficient gradient boosting decision tree". In: *Advances in Neural Information Processing Systems*.

[Keller 2015] Keller, A., K. Masania, A. C. Taylor, and C. Dransfeld (2015). "Fast-curing epoxy polymers with silica nanoparticles: properties and rheo-kinetic modelling". In: *Journal of Materials Science* 51.1, pp. 236–251. DOI: 10.1007/s10853-015-9158-y.

[Kenane 1997] Kenane, M. and M. L. Benzeggagh (1997). "Mixed-mode delamination fracture toughness of unidirectional glass/epoxy composites under fatigue loading". In: *Composites Science and Technology*. DOI: 10.1016/S0266-3538(97)00021-3.

[Kesavan 2008] Kesavan, Ajay, Sabu John, and Israel Herszberg (2008). "Structural health monitoring of composite structures using artificial intelligence protocols". In: *Journal of Intelligent Material Systems and Structures*. DOI: 10.1177/1045389X06073688.

[Kim 1993] Kim, Jin Soo and Dai Gil Lee (1993). "On-line cure monitoring and viscosity measurement of carbon fiber epoxy composite materials". In: *Journal of Materials Processing Tech.* DOI: 10.1016/0924-0136(93)90105-F.

[Klosterman 2021] Klosterman, Donald, Charles Browning, Issa Hakim, and Kyle Lach (2021). "Investigation of various techniques for controlled void formation in fiberglass/epoxy composites". In: *Journal of Composite Materials*. DOI: 10.1177/0021998320952517.

[Konstantopoulos 2019] Konstantopoulos, S, Christian Hueber, Ioannis Antoniadis, John Summerscales, and Ralf Schledjewski (2019). *Liquid composite*

molding reproducibility in real-world production of fiber reinforced polymeric composites: a review of challenges and solutions. DOI: 10.1080/20550340.2019.1635778.

[S. Konstantopoulos 2014] Konstantopoulos, S., E. Fauster, and R. Schledjewski (2014). "Monitoring the production of FRP composites: A review of in-line sensing methods". In: *Express Polymer Letters.* DOI: 10.3144/expresspolymlett.2014.84.

[Kosmann 2015] Kosmann, N., J. M. Karsten, M. Schuett, K. Schulte, and B. Fiedler (2015). "Determining the effect of voids in GFRP on the damage behaviour under compression loading using acoustic emission". In: *Composites Part B: Engineering* 70, pp. 184–188. DOI: 10.1016/j.compositesb.2014.11.010.

[Kousourakis 2006] Kousourakis, A., A. P. Mouritz, and M. K. Bannister (2006). "Interlaminar properties of polymer laminates containing internal sensor cavities". In: *Composite Structures.* DOI: 10.1016/j.compstruct.2006.04.086.

[Kuentzer 2007] Kuentzer, Nina, Pavel Simacek, Suresh G. Advani, and Shawn Walsh (2007). "Correlation of void distribution to VARTM manufacturing techniques". In: *Composites Part A: Applied Science and Manufacturing.* DOI: 10.1016/j.compositesa.2006.08.005.

[Labat 2001] Labat, L., J. Bréard, S. Pillut-Lesavre, and G. Bouquet (2001). "Void fraction prevision in LCM parts". In: *EPJ Applied Physics.* DOI: 10.1051/epjap:2001104.

[Laulusa 2006] Laulusa, A., O. A. Bauchau, J. Y. Choi, V. B.C. Tan, and L. Li (2006). "Evaluation of some shear deformable shell elements". In: *International Journal of Solids and Structures.* DOI: 10.1016/j.ijsolstr.2005.08.006.

[Lawrence 2004] Lawrence, Jeffrey M., John Barr, Rajat Karmakar, and Suresh G. Advani (2004). "Characterization of preform permeability in the presence of race tracking". In: *Composites Part A: Applied Science and Manufacturing.* DOI: 10.1016/j.compositesa.2004.05.002.

[Lebel 2017] Lebel, François, Edu Ruiz, and François Trochu (2017). "Void content analysis and processing issues to minimize defects in liquid composite molding". In: *Polymer Composites* 40.1, pp. 109–120. DOI: 10.1002/pc.24609.

[Leclerc 2008] Leclerc, Jean Sébastien and Edu Ruiz (2008). "Porosity reduction using optimized flow velocity in Resin Transfer Molding". In: *Composites Part A: Applied Science and Manufacturing.* DOI: 10.1016/j.compositesa.2008.09.008.

[D. H. Lee 2006] Lee, Doh Hoon, Woo Il Lee, and Moon Koo Kang (2006). "Analysis and minimization of void formation during resin transfer molding process". In: *Composites Science and Technology.* DOI: 10.1016/j.compscitech.2005.07.008.

[S. Lee 2021] Lee, Sooyoung, Chaeyoung Hong, Taeseong Choi, Hye-gyu Kim, Seong-woo Im, Soo-chang Kang, Young-bin Park, and Wooseok Ji (2021). "CSAI analysis of non-crimp fabric cross-ply laminate manufactured through wet compression molding process". In: *Composite Structures* 255.June 2020, p. 113056. DOI: 10.1016/j.compstruct.2020.113056.

[Lefik 2003] Lefik, M. and B. A. Schrefler (2003). "Artificial neural network as an incremental non-linear constitutive model for a finite element code". In: *Computer Methods in Applied Mechanics and Engineering.* DOI: 10.1016/S0045-7825(03)00350-5.

[Liu 2016] Liu and Chen (2016). "A review of void formation and its effects on the mechanical performance of carbon fiber reinforced plastic". In: *Engineering Transactions* 64.1, pp. 33–51.

[K. S. Liu 1998] Liu, Kuo Shih and Stephen W. Tsai (1998). "A progressive quadratic failure criterion for a laminate". In: *Composites Science and Technology*. DOI: 10.1016/S0266-3538(96)00141-8.

[L. Liu 2006] Liu, Ling, Bo Ming Zhang, Dian Fu Wang, and Zhan Jun Wu (2006). "Effects of cure cycles on void content and mechanical properties of composite laminates". In: *Composite Structures*. DOI: 10.1016/j.compstruct.2005.02.001.

[W. K. Liu 2021] Liu, Wing Kam, Shaofan Li, and Harold S Park (2021). "Eighty Years of the Finite Element Method: Birth, Evolution, and Future". In: pp. 1–30.

[Xin Liu 2021] Liu, Xin, Su Tian, Fei Tao, and Wenbin Yu (2021). "A review of artificial neural networks in the constitutive modeling of composite materials". In: *Composites Part B: Engineering* 224.March, p. 109152. DOI: 10.1016/j.compositesb.2021.109152.

[Xing Liu 2022] Liu, Xing, Tian Qiao Liu, and Peng Feng (2022). "Long-term performance prediction framework based on XGBoost decision tree for pultruded FRP composites exposed to water, humidity and alkaline solution". In: *Composite Structures* 284.December 2021, p. 115184. DOI: 10.1016/j.compstruct.2022.115184.

[Liu 2015] Liu, Yuksel C. Yabansu, Ankit Agrawal, Surya R. Kalidindi, and Alok N. Choudhary (2015). "Machine learning approaches for elastic localization linkages in high-contrast composite materials". In: *Integrating Materials and Manufacturing Innovation* 4.1, pp. 192–208. DOI: 10.1186/s40192-015-0042-z.

[Loendersloot 2011] Loendersloot, R. (2011). "Permeability of non-crimp fabric preforms". In: *Non-Crimp Fabric Composites*. Woodhead Publishing Limited. Chap. 8, pp. 166–215. DOI: 10.1533/9780857092533.2.166.

[Lomov 2011] Lomov, S.V., T. Truong Chi, and I. Verpoest (2011). "Mechanical properties of non-crimp fabric (NCF) based composites: stiffness and strength". In: *Non-Crimp Fabric Composites*. 1999. Woodhead Publishing Limited. Chap. 11, pp. 263–288. DOI: 10.1533/9780857092533.3.263.

[Lopes 2014] Lopes, C. S., S. Sádaba, F. Naya, and C. González (2014). "Multiscale Simulation Strategy for Low-Velocity Impact on FRP". In: *Proceedings of the American Society for Composites - 29th Technical Conference, ASC 2014; 16th US-Japan Conference on Composite Materials; ASTM-D30 Meeting*. September 2014.

[Lu 1990] Lu, Stephen C.Y. (1990). "Machine learning approaches to knowledge synthesis and integration tasks for advanced engineering automation". In: *Computers in Industry* 15.1-2, pp. 105–120. DOI: 10.1016/0166-3615(90)90088-7.

[Lystrup 2020] Lystrup, C., A. George, B. Zobell, K. Boster, C. Childs, H. Girod, and D. Fullwood (2020). "Optical measurement of voids in situ during infusion of carbon reinforcements". In: *Journal of Composite Materials*. DOI: 10.1177/0021998320959820.

[MacLaren 2009] MacLaren, O., J. M. Gan, C. M.D. Hickey, S. Bickerton, and P. A. Kelly (2009). "The RTM-Light manufacturing process: Experimentation and modelling". In: *ICCM International Conferences on Composite Materials*.

[Maimí 2007] Maimí, P., P. P. Camanho, J. A. Mayugo, and C. G. Dávila (2007). "A continuum damage model for composite laminates: Part I - Constitutive model". In: *Mechanics of Materials* 39.10, pp. 897–908. DOI: 10.1016/j.mechmat.2007.03.005.

[Marani 2018] Marani, R., D. Palumbo, V. Renò, U. Galietti, E. Stella, and T. D'Orazio (2018). "Modeling and classification of defects in CFRP laminates by thermal non-destructive testing". In: *Composites Part B: Engineering* 135.June 2017, pp. 129–141. DOI: 10.1016/j.compositesb.2017.10.010.

[Martin 1999] Martin, R. H. and B. D. Davidson (1999). "Mode II fracture toughness evaluation using four point bend, end notched flexure test". In: *Plastics, Rubber and Composites Processing and Applications*. DOI: 10.1179/146580199101540565.

[Mason 2022] Mason, Hannah (Jan. 2022). "BMW rolls out multi-material Carbon Cage with 2022 iX vehicle line". In: *CompositeWorld*, pp. 44–49.

[Matsuzaki 2021] Matsuzaki, Ryosuke, Masato Morikawa, Yuya Oikawa, and Kengo Ushiyama (2021). "Predicting thickness impregnation in a VaRTM resin flow simulation using machine learning". In: *Composites Part C: Open Access* 5.March, p. 100158. DOI: 10.1016/j.jcomc.2021.100158.

[Matsuzaki 2014] Matsuzaki, Ryosuke, Daigo Seto, Akira Todoroki, and Yoshihiro Mizutani (2014). "Void formation in geometry-anisotropic woven fabrics in resin transfer molding". In: *Advanced Composite Materials*. DOI: 10.1080/09243046.2013.832829.

[Mayer 2016a] Mayer, Natalie, Jens Prowe, Tamas Havar, Roland Hinterhölzl, and Klaus Drechsler (2016a). "Structural analysis of composite components considering manufacturing effect". In: *Composite Structures*. DOI: 10.1016/j.compstruct.2016.01.023.

[Mayer 2016b] Mayer, Natalie, Björn Van Den Broucke, Jens Prowe, Tamas Havar, and Roland Hinterhölzl (2016b). "Finite element mapping for incompatible FE meshes of composite structures". In: *Advances in Engineering Software*. DOI: 10.1016/j.advengsoft.2016.05.007.

[McKelvie 1978] McKelvie, A. N. (1978). "The measurement of paint consistency by flow cups". In: *Progress in Organic Coatings*. DOI: 10.1016/0300-9440(78)80003-4.

[Mehdikhani 2019] Mehdikhani, Mahoor, Larissa Gorbatikh, Ignaas Verpoest, and Stepan V. Lomov (2019). "Voids in fiber-reinforced polymer composites: A review on their formation, characteristics, and effects on mechanical performance". In: *Journal of Composite Materials* 53.12, pp. 1579–1669. DOI: 10.1177/0021998318772152.

[Meister 2021] Meister, Sebastian, Mahdieu Wermes, Jan Stüve, and Roger M. Groves (2021). "Investigations on Explainable Artificial Intelligence methods for the deep learning classification of fibre layup defect in the automated composite manufacturing". In: *Composites Part B: Engineering* 224.July, p. 109160. DOI: 10.1016/j.compositesb.2021.109160.

[Mesogitis 2014] Mesogitis, T. S., A. A. Skordos, and A. C. Long (2014). "Uncertainty in the manufacturing of fibrous thermosetting composites: A review". In: *Composites Part A: Applied Science and Manufacturing* 57, pp. 67–75. DOI: 10.1016/j.compositesa.2013.11.004.

[Montoro 2011] Montoro, Sergio Roberto, Marcos Yutaka Shiino, Tessie Gouvea Da Cruz, Maria Odila Hilário Cioffi, and Herman Jacobus Cornelis Woorwald (2011). "Influence of voids on the flexural resistance of the NCF/RTM6 composites". In: *Procedia Engineering* 10, pp. 3220–3225. DOI: 10.1016/j.proeng.2011.04.532.

[Mozaffar 2019] Mozaffar, M., R. Bostanabad, W. Chen, K. Ehmann, Jian Cao, and M. A. Bessa (2019). "Deep learning predicts path-dependent plasticity". In: *Proceedings of the National Academy of Sciences of the United States of America*. DOI: 10.1073/pnas.1911815116.

[Mukhopadhyay 2021] Mukhopadhyay, T., S. Naskar, S. Chakraborty, P. K. Karsh, R. Choudhury, and S. Dey (2021). "Stochastic Oblique Impact on Composite Laminates: A Concise Review and Characterization of the Essence of Hybrid Machine Learning Algorithms". In: *Archives of Computational Methods in Engineering* 28.3, pp. 1731–1760. DOI: 10.1007/s11831-020-09438-w.

[Nali 2012] Nali, P. and E. Carrera (2012). "A numerical assessment on two-dimensional failure criteria for composite layered structures". In: *Composites Part B: Engineering* 43.2, pp. 280–289. DOI: 10.1016/j.compositesb.2011.06.018.

[Nguyen-Thanh 2020] Nguyen-Thanh, Vien Minh, Xiaoying Zhuang, and Timon Rabczuk (2020). "A deep energy method for finite deformation hyperelasticity". In: *European Journal of Mechanics, A/Solids*. DOI: 10.1016/j.euromechsol.2019.103874.

[Nielsen 2002] Nielsen, D. R. and R. Pitchumani (2002). "Closed-loop flow control in resin transfer molding using real-time numerical process simulations". In: *Composites Science and Technology*. DOI: 10.1016/S0266-3538(01)00213-5.

[Núñez 1995] Núñez, Lisardo, F. Fraga, L. Fraga, T. Salgado, and J. Rodriguez Añón (1995). "Determination of the optimum epoxy/curing agent ratio: A study of different kinetic parameters". In: *Pure and Applied Chemistry*. DOI: 10.1351/pac199567071091.

[O'Brien 2021] O'Brien, J. M., S. Montgomery, A. Yaghi, and S. M. Afazov (2021). "Process chain simulation of laser powder bed fusion including heat treatment and surface hardening". In: *CIRP Journal of Manufacturing Science and Technology*. DOI: 10.1016/j.cirpj.2021.01.006.

[Okereke 2014] Okereke, M. I., A. I. Akpoyomare, and M. S. Bingley (2014). "Virtual testing of advanced composites, cellular materials and biomaterials: A review". In: *Composites Part B: Engineering*. DOI: 10.1016/j.compositesb.2014.01.007.

[G. B. Olson 1997] Olson, G. B. (1997). "Computational design of hierarchically structured materials". In: *Science*. DOI: 10.1126/science.277.5330.1237.

[R. S. Olson 2019] Olson, Randal S. and Jason H. Moore (2019). "TPOT: A Tree-Based Pipeline Optimization Tool for Automating Machine Learning". In: DOI: 10.1007/978-3-030-05318-5{_}8.

[Olsson 1992] Olsson, Robin (1992). "Impact response of orthotropic composite plates predicted from a one-parameter differential equation". In: *AIAA Journal*. DOI: 10.2514/3.11105.

[Olsson 2001] Olsson, Robin (2001). "Analytical prediction of large mass impact damage in composite laminates". In: *Composites - Part A: Applied Science and Manufacturing*. DOI: 10.1016/S1359-835X(01)00073-2.

[Park 2011] Park, Chung Hae. and Woo. Lee (2011). "Modeling void formation and unsaturated flow in liquid composite molding processes: A survey and review". In: *Journal of Reinforced Plastics and Composites* 30.11, pp. 957–977. DOI: 10.1177/0731684411411338.

[Parnas 1991] Parnas, Richard S. and Frederick R. Phelan (1991). "Effect of heterogeneous porous media on mold filling in resin transfer molding". In: *S.A.M.P.E. quarterly*.

[Patel 1995a] Patel, N. and L. James Lee (1995a). "Effects of fiber mat architecture on void formation and removal in liquid composite molding". In: *Polymer Composites*. DOI: 10.1002/pc.750160507.

[Patel 1996a] Patel, N. and L. James Lee (1996a). "Modeling of void formation and removal in liquid composite molding. Part I: Wettability analysis". In: *Polymer Composites*. DOI: 10.1002/pc.10594.

[Patel 1996b] Patel, N. and L. James Lee (1996b). "Modeling of void formation and removal in liquid composite molding. Part II: Model development and implementation". In: *Polymer Composites*. DOI: 10.1002/pc.10595.

[Patel 1995b] Patel, N., V. Rohatgi, and L. James Lee (1995b). "Micro scale flow behavior and void formation mechanism during impregnation through a unidirectional stitched fiberglass mat". In: *Polymer Engineering & Science*. DOI: 10.1002/pen.760351006.

[Pfrommer 2018] Pfrommer, Julius, Clemens Zimmerling, Jinzhao Liu, Luise Kärger, Frank Henning, and Jürgen Beyerer (2018). "Optimisation of manufacturing process parameters using deep neural networks as surrogate models". In: *Procedia CIRP* 72, pp. 426–431. DOI: 10.1016/j.procir.2018.03.046.

[Pham 2005] Pham, D. T. and A. A. Afify (2005). "Machine-learning techniques and their applications in manufacturing". In: *Proceedings of the Institution of Mechanical Engineers, Part B: Journal of Engineering Manufacture*. DOI: 10.1243/095440505X32274.

[Pierce 2017] Pierce, Robert S. and Brian G. Falzon (2017). "Simulating Resin Infusion through Textile Reinforcement Materials for the Manufacture of Complex Composite Structures". In: *Engineering* 3.5, pp. 596–607. DOI: 10.1016/J.ENG.2017.04.006.

[Pinho 2005] Pinho, S. T., C. G. Dávila, P. P. Camanho, L. Iannucci, and P. Robinson (2005). "Failure Models and Criteria for FRP Under In-Plane or Three-Dimensional Stress States Including Shear Non-linearity". In: *Nasa/Tm-2005-213530*.

[Potter 2009] Potter, K. D. (2009). "Understanding the origins of defects and variability in composites manufacture". In: *ICCM International Conferences on Composite Materials*.

[Protz 2015] Protz, R., N. Kosmann, M. Gude, W. Hufenbach, K. Schulte, and B. Fiedler (2015). "Voids and their effect on the strain rate dependent material properties and fatigue behaviour of non-crimp fabric composites materials". In: *Composites Part B: Engineering*. DOI: 10.1016/j.compositesb.2015.08.018.

[Puck 1998] Puck, A. and H. Schürmann (1998). "Failure analysis of FRP laminates by means of physically based phenomenological models". In: *Composites Science and Technology*. DOI: 10.1016/S0266-3538(96)00140-6.

[Qi 2019] Qi, Zhenchao, Nanxi Zhang, Yong Liu, and Wenliang Chen (2019). "Prediction of mechanical properties of carbon fiber based on cross-scale FEM and machine learning". In: *Composite Structures* 212.January, pp. 199–206. DOI: 10.1016/j.compstruct.2019.01.042.

[Ramasamy 2014] Ramasamy, P. and S. Sampathkumar (2014). "Prediction of impact damage tolerance of drop impacted WGFRP composite by artificial neural network using acoustic emission parameters". In: *Composites Part B: Engineering*. DOI: 10.1016/j.compositesb.2013.12.028.

[Raschka 2019] Raschka, Sebastian (2019). *Python® Machine Learning*. DOI: 10.1002/9781119557500.

[Reiland 2020] Reiland, Johanna; Laszlo; Bax, and Marco; Lerides (2020). *A vision on the future of automotive lightweighting*. Tech. rep.

[Rieber 2009] Rieber, G. and P. Mitschang (2009). "Full characterization of a stitched twill weave textile by unsaturated 2-D and 3-D permeability measurements". In: *ICCM International Conferences on Composite Materials*.

[Robinson 2000] Robinson, P. and J.M. Hodgkinson (2000). "Interlaminar fracture toughness". In: *Mechanical Testing of Advanced Fibre Composites*. DOI: 10.1533/9781855738911.170.

[Rohatgi 1996] Rohatgi, V., N. Patel, and L. James Lee (1996). "Experimental investigation of flow-induced microvoids during impregnation of unidirectional stitched fiberglass mat". In: *Polymer Composites*. DOI: 10.1002/pc.10601.

[Rong 2019] Rong, Qingyuan, Han Wei, Xingyi Huang, and Hua Bao (2019). "Predicting the effective thermal conductivity of composites from cross sections images using deep learning methods". In: *Composites Science and Technology*. DOI: 10.1016/j.compscitech.2019.107861.

[Rudd 1997] Rudd, C D, A C Long, K N Kendall, and C G E Mangin (1997). "Introduction to liquid composite moulding". In: *Liquid Moulding Technologies*. DOI: 10.1533/9781845695446.1.

[Ruiz 2006] Ruiz, E., V. Achim, Sofiane Soukane, F. Trochu, and J. Bréard (2006). "Optimization of injection flow rate to minimize micro/macro-voids formation in resin transfer molded composites". In: *Composites Science and Technology* 66.3-4, pp. 475–486. DOI: 10.1016/j.compscitech.2005.06.013.

[Sacco 2020] Sacco, Christopher, Anis Baz Radwan, Andrew Anderson, Ramy Harik, and Elizabeth Gregory (2020). "Machine learning in composites manufacturing: A case study of Automated Fiber Placement inspection". In: *Composite Structures* 250, p. 112514. DOI: 10.1016/j.compstruct.2020.112514.

[Sachse 2020] Sachse, R., A. K. Pickett, and P. Middendorf (2020). "Simulation of impact and residual strength of thick laminate composites". In: *Composites Part B: Engineering* 195.November 2019, p. 108070. DOI: 10.1016/j.compositesb.2020.108070.

[Sands 2001] Sands, J. M., B. K. Fink, S. H. McKnight, C. H. Newton, J.W. Gillespie Jr., and G. R. Palmese (2001). "Environmental issues for polymer matrix composites and structural adhesives". In: *Clean Products and Processes*. DOI: 10.1007/s100980000089.

[Santulli 2002] Santulli, C., R. Garcia Gil, A. C. Long, and M. J. Clifford (2002). "Void content measurements in commingled E-glass/polypropylene composites using image analysis from optical micrographs". In: *Science and Engineering of Composite Materials*. DOI: 10.1515/secm.2002.10.2.77.

[Schnabel 2011] Schnabel, A. and T. Gries (2011). "Production of non-crimp fabrics for composites". In: *Non-Crimp Fabric Composites*. DOI: 10.1533/9780857092533.1.3.

[Schneider 2011] Schneider, M. (2011). "Automated analysis of defects in non-crimp fabrics for composites". In: *Non-Crimp Fabric Composites*. DOI: 10.1533/9780857092533.1.103.

[Senoguz 2001] Senoguz, M. T., F. D. Dungan, A. M. Sastry, and J. T. Klamo (2001). "Simulations and experiments on low-pressure permeation of fabrics: Part II - The variable gap model and prediction of permeability". In: *Journal of Composite Materials*. DOI: 10.1106/HWL5-599F-8NA8-XAN0.

[Seyhan 2005] Seyhan, A. Tuğrul, Gökmen Tayfur, Murat Karakurt, and Metin Tanoğlu (2005). "Artificial neural network (ANN) prediction of compressive strength of VARTM processed polymer composites". In: *Computational Materials Science* 34.1, pp. 99–105. DOI: 10.1016/j.commatsci.2004.11.001.

[Shah 2019] Shah, S. Z.H., S. Karuppanan, P. S.M. Megat-Yusoff, and Z. Sajid (2019). "Impact resistance and damage tolerance of fiber reinforced composites: A review". In: *Composite Structures* 217.November 2018, pp. 100–121. DOI: 10.1016/j.compstruct.2019.03.021.

[Sharma 2021] Sharma, A, T Mukhopadhyay, S M Rangappa, S Siengchin, and V Kushvaha (2021). "Advances in computational intelligence of polymer composite materials : Machine learning assisted modeling , analysis and design". In: *Research Square*, pp. 1–83.

[Shi 2012] Shi, Y., T. Swait, and C. Soutis (2012). "Modelling damage evolution in composite laminates subjected to low velocity impact". In: *Composite Structures* 94.9, pp. 2902–2913. DOI: 10.1016/j.compstruct.2012.03.039.

[S. M. Sisodia 2016] Sisodia, S. M., S. C. Garcea, A. R. George, D. T. Fullwood, S. M. Spearing, and E. K. Gamstedt (2016). "High-resolution computed tomography in resin infused woven carbon fibre composites with voids". In: *Composites Science and Technology*. DOI: 10.1016/j.compscitech.2016.05.010.

[S. Sisodia 2015] Sisodia, Sanjay, E. Kristofer Gamstedt, Fredrik Edgren, and Janis Varna (2015). "Effects of voids on quasi-static and tension fatigue behaviour of carbon-fibre composite laminates". In: *Journal of Composite Materials* 49.17, pp. 2137–2148. DOI: 10.1177/0021998314541993.

[Skordos 2000] Skordos, A. A. and I. K. Partridge (2000). "Dielectric flow sensing in resin transfer moulding of carbon fibre reinforced composites". In: *Plastics, Rubber and Composites Processing and Applications*. DOI: 10.1179/146580100101541201.

[Sozer 2012] Sozer, E. M., P. Simacek, and S. G. Advani (2012). "Resin transfer molding (RTM) in polymer matrix composites". In: *Manufacturing Techniques for Polymer Matrix Composites (PMCs)*. Woodhead Publishing Limited, pp. 245–309. DOI: 10.1016/B978-0-85709-067-6.50009-2.

[Stabik 2009] Stabik, J., A. Dybowska, M. Szczepanik, and Suchoń (2009). "Viscosity measurements of epoxy resin filled with ferrite powders". In: *Archives of Materials Science and Engineering*.

[Stamopoulos 2016] Stamopoulos, A. G., K. I. Tserpes, P. Prucha, and D. Vavrik (2016). "Evaluation of porosity effects on the mechanical properties of carbon fiber-reinforced plastic unidirectional laminates by X-ray computed tomography and mechanical testing". In: *Journal of Composite Materials*. DOI: 10.1177/0021998315602049.

[Stieber 2021] Stieber, Simon, Niklas Schröter, Alexander Schiendorfer, Alwin Hoffmann, and Wolfgang Reif (2021). "FlowFrontNet: Improving Carbon Composite Manufacturing with CNNs". In: *Lecture Notes in Computer Science (including subseries Lecture Notes in Artificial Intelligence and Lecture Notes in Bioinformatics)* 12460 LNAI, pp. 411–426. DOI: 10.1007/978-3-030-67667-4{_}25.

[J. M. Tang 1987] Tang, Jian Mao, Woo I. Lee, and George S. Springer (1987). "Effects of Cure Pressure on Resin Flow, Voids, and Mechanical Properties". In: *Journal of Composite Materials*. DOI: 10.1177/002199838702100502.

[M. Tang 2020] Tang, Mingzhu, Qi Zhao, Steven X. Ding, Huawei Wu, Linlin Li, Wen Long, and Bin Huang (2020). "An improved lightGBM algorithm for online fault detection of wind turbine gearboxes". In: *Energies* 13.4. DOI: 10.3390/en13040807.

[Tay 2003] Tay, T. E. (2003). *Characterization and analysis of delamination fracture in composites: An overview of developments from 1990 to 2001*. DOI: 10.1115/1.1504848.

[Tersing 2012] Tersing, H., J. Lorentzon, A. Francois, A. Lundbäck, B. Babu, J. Barboza, V. Bäcker, and L. E. Lindgren (2012). "Simulation of manufacturing chain of a titanium aerospace component with experimental validation". In: *Finite Elements in Analysis and Design*. DOI: 10.1016/j.finel.2011.10.002.

[Tretiak 2022] Tretiak, Iryna, Luiz F. Kawashita, and Stephen R. Hallett (2022). "Predicting short beam shear strength reduction in carbon/epoxy laminates containing voids". In: *Composite Structures* 290.March, p. 115472. DOI: 10.1016/j.compstruct.2022.115472.

[Trochu 2006] Trochu, François, Edu Ruiz, Vincent Achim, and Sofiane Soukane (2006). "Advanced numerical simulation of liquid composite molding for process analysis and optimization". In: *Composites Part A: Applied Science and Manufacturing* 37.6 SPEC. ISS. Pp. 890–902. DOI: 10.1016/j.compositesa.2005.06.003.

[Truong 2008] Truong, T. C., D. S. Ivanov, D. V. Klimshin, S. V. Lomov, and I. Verpoest (2008). "Carbon composites based on multi-axial multi-ply stitched preforms. Part 7: Mechanical properties and damage observations in composites with sheared reinforcement". In: *Composites Part A: Applied Science and Manufacturing*. DOI: 10.1016/j.compositesa.2008.05.004.

[Tsai 1971] Tsai, Stephen W. and Edward M. wu (1971). "A General Theory of Strength for Anisotropic Materials". In: *Journal of Composite Materials*. DOI: 10.1177/002199837100500106.

[Tuncol 2007] Tuncol, Goker, Murat Danisman, Alper Kaynar, and E. Murat Sozer (2007). "Constraints on monitoring resin flow in the resin transfer molding (RTM) process by using thermocouple sensors". In: *Composites Part A: Applied Science and Manufacturing*. DOI: 10.1016/j.compositesa.2006.10.009.

[Turon 2018] Turon, Albert; Pedro P.; Camanho, Albert; Soto, and Emilio V. González (2018). "Analysis of Delamination Damage in Composite Structures Using Cohesive Elements". In: *Comprehensive Composite Materials II*. Vol. 5-8, pp. 19–40. DOI: 10.1016/B978-0-12-803581-8.10059-1.

[Uhl 1988] Uhl, K. M., B. Lucht, H. Jeong, and D. K. Hsu (1988). "Mechanical strength degradation of graphite fiber reinforced thermoset composites due to porosity". In: *Review of Progress in Quantitative Nondestructive Evaluation*. DOI: 10.1007/978-1-4613-0979-6{_}24.

[Vajari 2014] Vajari, D. (2014). "A micromechanical study of porous composites under longitudinal shear and transverse normal loading". In: *Composite Structures*. DOI: 10.1016/j.compstruct.2015.02.026.

[Varna 1995] Varna, J., R. Joffe, L. A. Berglund, and T. S. Lundström (1995). "Effect of voids on failure mechanisms in RTM laminates". In: *Composites Science and Technology*. DOI: 10.1016/0266-3538(95)00024-0.

[Vieira 2019] Vieira, Sandra, Walter Hugo Lopez Pinaya, and Andrea Mechelli (2019). "Introduction to machine learning". In: *Machine Learning: Methods and Applications to Brain Disorders*. DOI: 10.1016/B978-0-12-815739-8.00001-8.

[Wagner 2019] Wagner, H. N.R., H. Köke, S. Dähne, S. Niemann, C. Hühne, and R. Khakimova (2019). "Decision tree-based machine learning to optimize the laminate stacking of composite cylinders for maximum buckling load and minimum imperfection sensitivity". In: *Composite Structures* 220.February, pp. 45–63. DOI: 10.1016/j.compstruct.2019.02.103.

[Wang 2013] Wang, Ke Sheng (2013). "Towards zero-defect manufacturing (ZDM)-a data mining approach". In: *Advances in Manufacturing* 1.1, pp. 62–74. DOI: 10.1007/s40436-013-0010-9.

[Weng 2019] Weng, Ziqiao (2019). "From Conventional Machine Learning to AutoML". In: *Journal of Physics: Conference Series* 1207.1. DOI: 10.1088/1742-6596/1207/1/012015.

[Wilhelmy 1863] Wilhelmy, Ludwig (1863). "Ueber die Abhängigkeit der Capillaritäts-Constanten des Alkohols von Substanz und Gestalt des benetzten festen Körpers". In: *Annalen der Physik*. DOI: 10.1002/andp.18631950602.

[Wirth 2000] Wirth, Rüdiger (2000). "CRISP-DM : Towards a Standard Process Model for Data Mining". In: *Proceedings of the Fourth International Conference on the Practical Application of Knowledge Discovery and Data Mining*. DOI: 10.1.1.198.5133.

[Wisnom 1996] Wisnom, Michael R., Tom Reynolds, and Nigel Gwilliam (1996). "Reduction in interlaminar shear strength by discrete and distributed voids". In: *Composites Science and Technology*. DOI: 10.1016/0266-3538(95)00128-X.

[Wu 2020] Wu, Ling, Kepa Zulueta, Zoltan Major, Aitor Arriaga, and Ludovic Noels (2020). "Bayesian inference of non-linear multiscale model parameters accelerated by a Deep Neural Network". In: *Computer Methods in Applied Mechanics and Engineering*. DOI: 10.1016/j.cma.2019.112693.

[Wuest 2014] Wuest, Thorsten, Christopher Irgens, and Klaus Dieter Thoben (2014). "An approach to monitoring quality in manufacturing using supervised

machine learning on product state data". In: *Journal of Intelligent Manufacturing* 25.5, pp. 1167–1180. DOI: 10.1007/s10845-013-0761-y.

[Wuest 2016] Wuest, Thorsten, Daniel Weimer, Christopher Irgens, and Klaus Dieter Thoben (2016). "Machine learning in manufacturing: Advantages, challenges, and applications". In: *Production and Manufacturing Research* 4.1, pp. 23–45. DOI: 10.1080/21693277.2016.1192517.

[Xu 2014] Xu, Kun and Xiaomei Qian (2014). "An FEM analysis with consideration of random void defects for predicting the mechanical properties of 3d braided composites". In: *Advances in Materials Science and Engineering*. DOI: 10.1155/2014/439819.

[Xue 2021] Xue, Jing and Kedar Kirane (2021). "Effect of the shape of the softening damage law on the predicted tensile fracturing and energy dissipation in textile composites". In: *International Journal of Damage Mechanics*. DOI: 10.1177/1056789520986849.

[Yan 2020] Yan, Shibo, Xi Zou, Mohammad Ilkhani, and Arthur Jones (2020). "An efficient multiscale surrogate modelling framework for composite materials considering progressive damage based on artificial neural networks". In: *Composites Part B: Engineering* 194.March, p. 108014. DOI: 10.1016/j.compositesb.2020.108014.

[J. Yang 2010] Yang, Junying, Yuxi Jia, Yanyu Ding, Haidong He, Tongfei Shi, and Lijia An (2010). "Edge effect in RTM processes under constant pressure injection conditions". In: *Journal of Applied Polymer Science*. DOI: 10.1002/app.32470.

[Z. Yang 2019] Yang, Zijiang, Yuksel C. Yabansu, Dipendra Jha, Wei keng Liao, Alok N. Choudhary, Surya R. Kalidindi, and Ankit Agrawal (2019). "Establishing structure-property localization linkages for elastic deformation of three-dimensional high contrast composites using deep learning approaches". In: *Acta Materialia* 166, pp. 335–345. DOI: 10.1016/j.actamat.2018.12.045.

[Ye 2019] Ye, Sang, Bo Li, Qunyang Li, Hong Ping Zhao, and Xi Qiao Feng (2019). "Deep neural network method for predicting the mechanical properties of composites". In: *Applied Physics Letters* 115.16. DOI: 10.1063/1.5124529.

[Yenilmez 2009] Yenilmez, Bekir and E. Murat Sozer (2009). "A grid of dielectric sensors to monitor mold filling and resin cure in resin transfer molding". In: *Composites Part A: Applied Science and Manufacturing*. DOI: 10.1016/j.compositesa.2009.01.014.

[You 2016] You, Renchun, Yuan Yao, Jia Shi, Kaiyi Zheng, and Kai Hong Wang (2016). "Feature-selective clustering for ultrasonic-based automatic defect detection in FRP structures". In: *Chemometrics and Intelligent Laboratory Systems*. DOI: 10.1016/j.chemolab.2016.06.014.

[Yuan 2018] Yuan, Mengfei, Sean Paradiso, Bryce Meredig, and Stephen R. Niezgoda (2018). "Machine Learning–Based Reduce Order Crystal Plasticity Modeling for ICME Applications". In: *Integrating Materials and Manufacturing Innovation*. DOI: 10.1007/s40192-018-0123-x.

[Zabala 2014] Zabala, H., L. Aretxabaleta, G. Castillo, J. Urien, and J. Aurrekoetxea (2014). "Impact velocity effect on the delamination of woven carbon-epoxy plates subjected to low-velocity equienergetic impact loads". In: *Composites Science and Technology* 94, pp. 48–53. DOI: 10.1016/j.compscitech.2014.01.016.

[Zambal 2018] Zambal, Sebastian, Christian Eitzinger, Michael Clarke, John Klintworth, and Pierre-yves Mechin (July 2018). "A digital twin for composite parts manufacturing : Effects of defects analysis based on manufacturing data". In: *2018 IEEE 16th International Conference on Industrial Informatics (INDIN)*. IEEE, pp. 803–808. DOI: 10.1109/INDIN.2018.8472014.

[Zhang 2010] Zhang, Boming, Zhong Yang, Xinyang Sun, and Zhanwen Tang (2010). "A virtual experimental approach to estimate composite mechanical properties: Modeling with an explicit finite element method". In: *Computational Materials Science*. DOI: 10.1016/j.commatsci.2010.06.007.

[Zhao 2020] Zhao, Lujie, Yixiang Huang, Dengyu Xiao, Yanming Li, and Chengliang Liu (2020). "A Novel Method for Induction Motor Fault Identification Based on MSST and LightGBM". In: pp. 90–96. DOI: 10.1109/sdpc.2019.00025.

[Zhou 2006] Zhou, Fuping, Nina Kuentzer, Pavel Simacek, Suresh G. Advani, and Shawn Walsh (2006). "Analytic characterization of the permeability of dual-scale fibrous porous media". In: *Composites Science and Technology*. DOI: 10.1016/j.compscitech.2006.02.025.

[Zhu 2010] Zhu, Weiyao and Xiwu Xu (2010). "Finite element simulation of low velocity impact damage on composite laminates". In: *Fuhe Cailiao Xuebao/Acta Materiae Compositae Sinica* 27.6, pp. 200–207.

[Zimmerling 2019] Zimmerling, Clemens, Dominik Dörr, Frank Henning, and Luise Kärger (2019). "A machine learning assisted approach for textile formability assessment and design improvement of composite components". In: *Composites Part A: Applied Science and Manufacturing* 124.March, p. 105459. DOI: 10.1016/j.compositesa.2019.05.027.